



UNIVERSIDAD
POLITECNICA
DE VALENCIA

HYPERLOOP DESIGN REPORT

Makers UPV Team

Universitat Politècnica de València

Valencia - January 2016



HYPERLOOP DESIGN REPORT

Makers UPV Team

Universitat Politècnica de València

January 2016

“There is a fine line between genius and insanity. I have erased this line.”

Oscar Levant

“Amb diners, torrons”

Valencian proverb

Retrospective

After the experience lived in the Design Weekend held at Texas A& M University we feel overwhelmed. No mention about the fact that we did not expect to win, not one, but 2 awards and among them the top design concept award. We attended Design Weekend with eagerness but knowing that our rivals were formidable. Also, being 5 only we had a clear handicap regarding human capital but the result could not have been better.

This work was composed in a hurry and knowing that we had to deliver a minimum content. We have revised it, corrected errors and rephrased misleading sentences but it requires from a major overhaul to make it a truly rigorous report. Since we are studying simultaneously with this project we cannot devote it all the time we wish, so, this will be it from now.

The reader is going to encounter with an initial analysis which lays the foundations of the future works in a preliminary way. It will not find here an extensive and detailed study. Despite the fact we are proud of the level of development reached and we hope to keep improving the proposal.

Kind regards

Retrospectiva

Después de vivir la experiencia del Design Weekend en la Universidad de Texas A& M estamos abrumados. Ni tan siquiera mencionar que no esperábamos ganar, ya no uno, sino 2 premios y entre ellos el de mejor concepto de diseño. Íbamos al Design Weekend con mucha ilusión pero sabiendo que teníamos unos contrincantes más que formidables. Siendo además sólo 5 en el equipo estábamos en clara desventaja en lo que a capital humano se refiere, pero el resultado no pudo ser mejor.

Este documento fue redactado con prisa y sabiendo que teníamos que cumplir un mínimo de contenido. Hemos revisado su contenido, corregido erratas y replanteado frases malinterpretables pero requeriría de una revisión mayor para que fuera un documento verdaderamente riguroso. Dado que estamos compaginando estudios con este proyecto, no podemos dedicarle todo el tiempo que desearíamos, por lo que deberá bastar por ahora.

El lector se encontrará con un análisis inicial que sienta las bases de los futuros desarrollos de una forma preliminar. No encontrará un desarrollo extenso y detallado "al milímetro". A pesar de esto estamos orgullosos del punto en el que nos encontramos y esperamos poder seguir mejorando la propuesta.

Saludos cordiales

The Hyperloop Makers UPV Team
Valencia March-2016

Acknowledgements

The team would like to thank the following companies and institutions for their support to the Hyperloop Makers UPV project.

Special thanks to the Universitat Politècnica de Valencia (UPV) for all the support given, both in economic form, technical resources and in human value and experience. Thanks to Escuela Técnica Superior de Ingeniería de Diseño (ETSID) for enabling our advisor to travel with us. Many thanks to Vossloh for taking care of part of the travel expenses and giving us to present this work for the student community at UPV. Thanks to ANSYS and ANSYS Iberica for providing us with a software license which enabled us to perform this work as well as modeFrontier for their optimization software. Thanks to the ISA (Automation Institute at UPV) and a special mention to Professor Sergio García-Nieto whose helpful aid in the control of the levitation system made it possible. Thanks to Pau Raga and Antonio Gil from CMT-UPV for aiding the mesh generation during CFD calculations.

This is also an acknowledgment of volunteers' generous contributions, which have helped the project to grow faster and acquire new dimensions:

Francisco Presencia Fandos
Demetrio Muñoz Blanco
The Makers UPV association and community

Finally, our most sincere gratitude goes to our advisor, professor Vicente Dolz. Without his constant support, illusion and work this development would have failed.

The Hyperloop UPV Team



Abstract

This work studies the feasibility of a high-speed transportation system. In the first place, an open pre-design phase based on simple physical models is performed. Through the use of advanced multiobjective optimization techniques two situations are studied, acceleration, cruise and braking cases. Setting the design point, magnetic levitation system analysis is conducted and a CFD-based aerodynamic analysis is performed. Additionally, structural and modal analysis is carried out on a reference critical case as well as defining the braking methods and systems. Control and guidance study is performed and a cost analysis is done including production, scalability reports and ergonomic and passenger comfort analysis. As closure, conclusions about the proposal are withdrawn and future work is proposed. The final proposed pod has a cruise speed of 276 m/s , consuming as low as $26\text{ W}\cdot\text{h/pass km}$. It weighs around 20 tons and has capacity for 30 passengers or 3600 kg of payload in a 19 m total length.

KEYWORDS: Transportation, Systems engineering, System Optimization, Physical modelling, Numerical analysis, CFD aerodynamics, FEM simulation, Levitation, Energy efficiency

Contents

Retrospective	i
Acknowledgements	ii
Abstract	iii
Figure index	viii
Table index	ix
1 Preface	1
2 Introduction	2
2.1 Introduction	2
2.2 Objectives	3
2.3 Tools	3
2.4 Team description	4
3 Pre-design	6
3.1 Description of the problem	6
3.2 Models used defining the pre-design concept	6
3.2.1 External aerodynamics	6
3.2.2 Internal aerodynamics	9
3.2.3 Magnetic levitation system	9
3.2.4 Structure and weight	9
3.2.5 Propulsion system	9
3.2.6 Power systems	10
3.2.7 Cabin arrangement and payload	10
3.3 Optimization	11
3.3.1 Cruise configuration optimization results	11
3.3.2 Acceleration configuration optimization results	13
3.4 Chosen pre-design point	14
4 Detailed Study	15
4.1 Levitation system	15
4.1.1 Physical magnetostatic modelling and small real-life model	15
4.1.2 Magnetostatic 2-D configuration analysis	18
4.1.3 Magnetostatic 2-D parametric configuration analysis	21
4.1.4 Magnetostatic 3-D confirmation analysis	25
4.1.5 Magnetodynamic 3-D simulation	27
4.2 Aerodynamic and propulsion system study	30
4.2.1 CFD pre-processing	30

4.2.2	3-D cases	35
4.2.3	CFD Cases	38
4.2.4	Low speed propulsion system	47
4.3	Ergonomics, passenger comfort and design	49
4.4	Design re-optimization	51
4.5	Structural analysis	53
4.5.1	Static analysis	54
4.5.2	Modal analysis	59
4.6	Braking system	65
4.6.1	Alternative braking proposal	70
4.7	Guidance, navigation and control	71
4.7.1	Sensors on board	71
4.7.2	Control scheme	71
4.7.3	Guidance and navigation	72
4.7.4	Conclusions	76
4.8	Safety measures	77
5	Cost and production analysis	80
5.1	Pod cost breakdown	80
5.2	Track cost breakdown	83
5.3	Production planning	84
6	Final proposed solution specifications	86
7	Conclusions	89
8	Future work	92
	Bibliography	94

List of Figures

2.1 Initial concept sketch.	3
3.1 Aerodynamic stations and scheme.	8
3.2 Cruise case optimization results.	11
3.3 Acceleration case optimization results.	13
4.1 Root locus for the levitation system.	16
4.2 Simulink dynamic model.	16
4.3 Model system used to test the modelling approach.	17
4.4 Unit configuration 0.	18
4.5 Unit configuration 0 reversed.	18
4.6 EM simulation results for the configuration 0.	19
4.7 Unit configuration 1.	19
4.8 Unit configurations 1 – v_1 and 1 – v_2 .	20
4.9 EM simulation results for the configuration 1 – v_2 .	20
4.10 Parametric setup for magnetostatic configuration.	21
4.11 Force vs magnet radius parametric study.	22
4.12 Force vs permanent magnet thickness parametric study.	23
4.13 Force vs gap distance and coil intensity parametric study.	23
4.14 EM simulation results for the 3D setup.	25
4.15 EM simulation results for the 3D setup.	26
4.16 3D case geometry.	27
4.17 Magnet pull force vs simulation time.	28
4.18 EM simulation results for the 3D dynamic 3D setup.	28
4.19 2-D parametric CFD geometry domain with boundary conditions.	31
4.20 Mesh independence study: drag coefficient.	32
4.21 Mesh independence study: compressor mass flow rate.	32
4.22 2-D mesh: overall view.	33
4.23 2-D mesh: inlet detail.	33
4.24 2-D mesh: nozzle detail.	34
4.25 3-D parametric CFD geometry domain.	35
4.26 2-D mesh: overall surface view.	36
4.27 3-D mesh: inlet detail at symmetry plane.	36
4.28 3-D mesh: nozzle detail at symmetry plane.	37
4.29 Nozzle total pressure as a function of Mach number for the ramp cases.	38
4.30 Mach contours at the nozzle area, Mach 0.3.	38
4.31 Mach contours at the nozzle area, Mach 0.45.	39
4.32 Mach contours at the nozzle area, Mach 0.6.	39
4.33 Mach contours at the nozzle area, Mach 0.75.	40
4.34 Mach contours at the nozzle area, Mach 0.8.	40
4.35 Mach contours at the nozzle area, Mach 0.85.	41

4.36	Static pressure contours, inlet area, Mach 0.75.	41
4.37	Gap velocity vectors, coloured by Mach number, Mach 0.75.	42
4.38	Fanno flow along the gap for Mach 0.75.	42
4.39	Temperature contours, Mach 0.75.	43
4.40	Temperature contours, pod detail, Mach 0.75.	43
4.41	Shockwaves in the nozzle area	44
4.42	Shockwaves in the nozzle area	44
4.43	Contours of static pressure at pod wall.	45
4.44	Contours of static pressure at tube wall.	45
4.45	Contours of static temperature at pod wall.	45
4.46	Contours of static temperature at tube wall.	46
4.47	Temperature and pressure evolution on the pod wall for the cruise case.	46
4.48	Temperature and pressure evolution on the tube wall for the cruise case.	47
4.49	Cabin distribution proposal.	49
4.50	Cabin distribution proposal, perspective.	50
4.51	Cruise case optimization results.	51
4.52	Pressure cabin geometry details.	53
4.53	Cabin skin thickness displacement parametric study.	54
4.54	Cabin skin thickness stress parametric study.	55
4.55	Cabin mesh: front and side view.	55
4.56	Cabin mesh: perspective view.	56
4.57	Cabin deformation: perspective view.	56
4.58	Cabin deformation: perspective cut.	57
4.59	Cabin stress: perspective view.	57
4.60	Cabin stress: perspective cut.	58
4.61	Cabin structure modal spectrum.	59
4.62	First vibration mode of the cabin structure.	60
4.63	Second vibration mode of the cabin structure.	61
4.64	Third vibration mode of the cabin structure.	62
4.65	Fourth vibration mode of the cabin structure.	63
4.66	Fifth vibration mode of the cabin structure.	64
4.67	Pod braking flow patterns.	66
4.68	Pod inlet static pressure at braking.	67
4.69	Pod inlet static pressure at braking.	68
4.70	Static temperature at a braking timestep symmetry axis.	69
4.71	Static pressure at a braking timestep at symmetry axis.	69
4.72	Control scheme proposed for the pod.	71
4.73	Positoning patterns in the tube.	73
4.74	Positoning patterns in the tube. Terminal guidance.	74
4.75	Pod sensors arrangement.	76
5.1	Pod costs by subsystem.	80
5.2	Tube layout comparison.	83
5.3	Gantt diagram for the project production.	85

LIST OF FIGURES

viii

6.1	Pod velocity profile.	88
7.1	Proposed concept appearance.	89
8.1	Diversion system proposal.	93

List of Tables

3.1	Predesign parameters	6
3.2	Optimal dimensions and parameters	14
4.1	Final levitation unit dimensions and parameters.	24
4.2	Design dimensions and parameters	52
4.3	Sensor and magnitude cross table.	75
5.1	Pod cost breakout.	82
5.2	Pod final production costs.	82
5.3	Pod final production costs.	83
6.1	Pod final dimensions.	86
6.2	Pod final aerodynamic performance.	86
6.3	Pod final magnetic parameters.	86
6.4	Pod final power distribution.	87
6.5	Pod final mass budget.	87
6.6	Pod final power distribution.	87

1

Preface

First of all, the authors of this document want to thank and value in its right extent the importance of the opportunity that has been given to them. The times are changing in a swifter way than ever and, the famous Max Planck's quote: "a new scientific truth does not triumph by convincing its opponents and making them see the light, but rather because its opponents eventually die, and a new generation grows up that is familiar with it.", is getting out of the current paradigm at a steady pace.

Science today has evolved since Planck's times. New generation scientists need to adapt in order to keep making this world a better place for all and everything. This project stands in behalf of all this movement. Being ecologic is no longer an option in this epoch, and it has to keep with the standards of quality, security and fastness of the current society.

Here, we hope to deliver and fulfill a man's dream. The Hyperloop Makers UPV Team.

2

Introduction

2.1 Introduction

The current proposal differs substantially from the previous work done by SpaceX in the Hyperloop Alpha proposal [1]. The here proposed design uses magnetic attraction to the tube instead of repulsion to a non-ferrous metallic plate in order to levitate, also this design avoids the use of air cushioning because of the unpredictability in the forces and disturbances occurring on the pod. At present, means of transportation, which uses electromagnetic levitation (maglevs), are usually infeasible for long distances due to the high cost of construction and maintenance of its rails. In order to avoid these high costs, in this paper, the use of a cylindrical tube done with a ferromagnetic material without any type of active system or special material is proposed as a rail. On the other hand, the levitation modules are mounted in a cylindrical shaped pod, thereby achieving two major advantages:

- Reducing construction and maintenance costs of the rail.
- Considering the rail is an empty cylindrical tube, the tube has angular symmetry and the pod is able to roll to compensate the inertial forces produced by the different curves in the way, simplifying its controllability.

In addition, actuators used in an aerodynamic levitation introduce a significant inertia in the system, as a result of mechanical actuators and air compressibility, which is critical for an stable control of this levitation system. Focusing on propulsion, we have decided to implement a system which consists of a front compressor, which captures the intake air and delivers it to a tube inside the pod. This compressor is moved by an electric motor. The air travels the length of the pod through the aforementioned tube to a power turbine which recovers part of the available energy, finally the air is expanded through a nozzle at the pod's end producing the necessary thrust to the system.

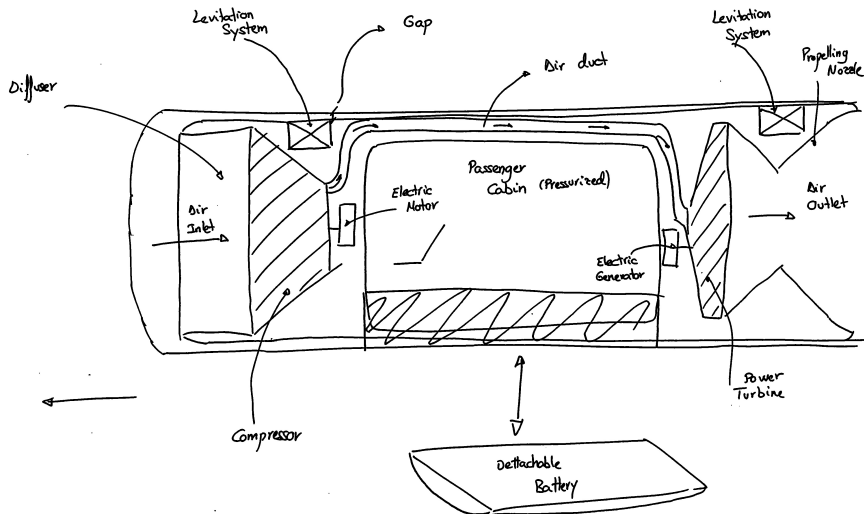


Figure 2.1: Initial concept sketch.

Thus, the present proposal is divided into two main systems: First, the magnetic levitation system consisting in attractive permanent magnets and electromagnets which aims to generate a controlled lift that allows the pod levitation. Second, aerodynamic system consisting in a diffuser-compressor, intermediate tube, a turbine and a nozzle which aims to generate enough thrust or drag to control the speed of the pod.

2.2 Objectives

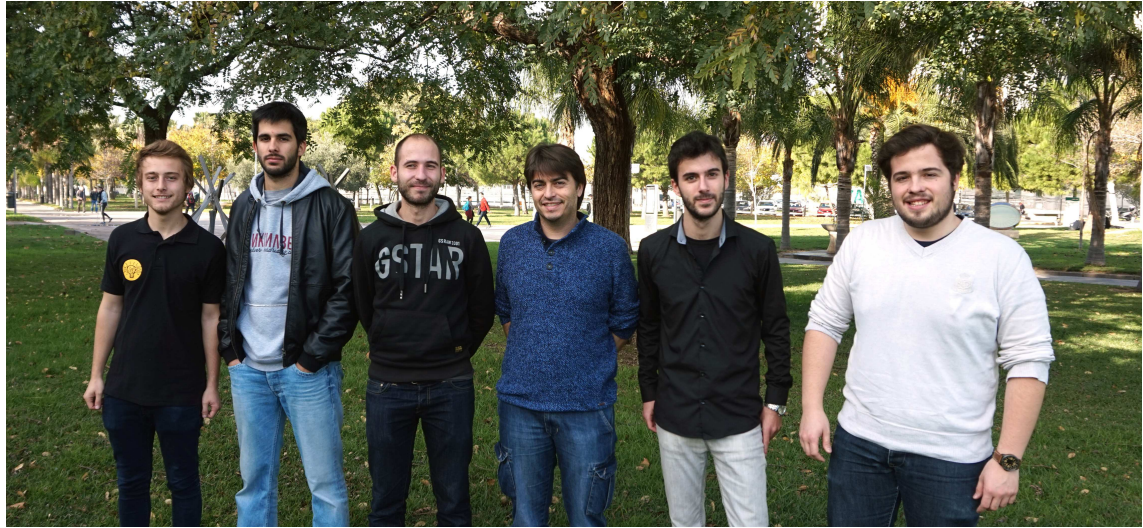
The main objective of this report is to provide a base design for the Hyperloop system based on the above description in a realistic way. Hyperloop is a surface based transportation system which runs inside a partially evacuated tube by levitation. This proposal aims for a 30 passenger configuration travelling as fast as possible inside transonic regime speeds.

2.3 Tools

Several tools are along this development. For the initial models and pre-design phase Microsoft Excel and modeFrontier were employed. For detailed study mainly ANSYS suite was used, specifically Fluent for CFD calculations, Maxwell for electromagnetic simulations and Mechanical for FEM calculations on the structure. On the modelling of the geometry, most developments were made in ANSYS integrated DesignModeler and some other were carried on with Autodesk Inventor. Finally, data plotting and formatting was done using MATLAB, which also was employed in the development of the control systems.

2.4 Team description

The Makers UPV Team composed of five spanish students from the Universitat Politècnica de València (UPV), reunited together with the purpose of helping the global community in the development of a brand-new high-speed ground transport system: the Hyperloop.



The team has the special support of Dr. Vicente Dolz, PhD. Mechanical Engineer, senior lecturer at the UPV and researcher at the Center of Thermal Engines (CMT) in the fields of energy recovery from exhaust gases, turbomachinery processes, heat flow modelling and rankine cycles using organic fluids (ORC). Dr. Dolz is passionate about science and technology, from quantum mechanics to complex aero-thermodynamic theories. Being an active publisher in journals such as *Applied Thermal Engineering* and *Applied Energy*, Dr. Dolz has showed a strong commitment in the project from the beginning, becoming the main advisor of the team.

In addition, the members of the team are an active part of a community of inventors, students, scientists, and hobbyists called Makers UPV, which was founded three years ago at the University to provide a more practical and hands-on experience to the students. In Makers UPV, people are brought together to create new things, learn from others and teach themselves reciprocally. In this short timeframe, the community has gained great attention through the projects and prizes won at challenges and competitions won by its members, such as the Space Apps Awards organised by NASA.

Furthermore, the Makers UPV Team has the support from the Universitat Politecnica de Valencia, one of the best universities in Spain according to Academic Ranking of World Universities, which has provided the team with tools to keep on working and researching.

In the long term, the team's vision is to raise support from more sponsors to keep on developing the technology, helping the global community in the creation of the Hyperloop. The team would be interested in joining the "Building" phase if enough support is raised after the Design Weekend.

Description of team members:**Ángel Benedicto:**

Ángel is currently doing his Masters in Aerospace Engineering. Member of UPV Flight Lab, he loves developing UAVs and drones. In his Bachelor thesis he designed a GPS navigation system and he participates in Makers UPV as a lecturer and creating new projects. His areas of interest include Aerodynamics and Design.

Daniel Orient:

Daniel obtained his Bachelor Degree in Aerospace Engineering (Aeroengines) last year and is now starting his M. Sc. in Automatic Control and Industrial Computer Science at UPV. Winner of the Ideas 2k15 Open Innovation Challenge, he won broad knowledge with his thesis on modeling and controlling an airship. Auditor in AIR NOSTRUM aerospace company, he built, programmed and controlled a multicopter himself.

David Pistoni:

David is a proactive and communicative student. Cofounder of the Makers UPV community, he completed his Bachelor last year and is currently doing his Masters in Industrial Engineering at UPV in parallel with a Bachelor degree in Psychology. In his B.Sc. thesis he invented a smart 3D Scanner and has helped in the design of HCube, a giant LED cube. Instructor of robotics and Arduino workshops, he also participates as a speaker in talks about 3D printing.

Germán Torres:

Germán loves creating new things. M.Sc. Aeronautical Engineer, he has extensive experience in implementing and managing scientific and maker projects. He was awarded with a honour mention for his thesis about the design of a Supersonic Unmanned Aircraft. He also designed a regional electric aircraft as part of the subject Aircraft Design and participated in the instrumentation of a dynamometric train wheel and bench setup. He qualified in the global top 5 design award at NASA Spaceapps contest in 2015 with the project GoSat.

Juan Vicén:

Juan is a passionate entrepreneur. He gained extensive experience in the Start-Up field both in Germany and Spain, having co-founded the first maker organisation in his home region. He is a double degree student currently doing his Masters in Mechanical Engineering. His academic background includes studying in the fields of Lean Start-Ups, Disruptive Innovation and Design Thinking at the Institute of Product Development at TUM. He built a smart air-quality measuring device and has researched on digital sounds for EVs.

3

Pre-design

3.1 Description of the problem

Considering the design showed on figure 2.1 presented system is mainly described by the following parameters:

Parameter	Value Range	Units	Parameter	Value Range	Units
Pod Length	12 – 16	m	Tube diameter	1.79	m
Gap distance	0.05	m	Tube pressure	100 – 800	Pa
Tube temperature	300	K	Travel speed	200 – 340	m/s
Diffuser suction	0.85 – 1.1	[–]	Diffuser section ratio	0.9 – 1	[–]
$(\pi_C)_{t/t}$	10 – 35	[–]	$(\eta_C)_{t/t}$	0.7	[–]
$u_{C_{Out}}$	300 – 500	m/s	f_{Duct}	0.01	[–]
L_{Duct}	Pod length – 4m	m	$(\pi_T)_{t/t}$	1.1 – 25	[–]
$(\eta_T)_{t/t}$	0.7	[–]	$u_{T_{Out}}$	300 – 500	m/s
f_{Gap}	0.02	[–]	Travel length	600	km

Table 3.1: Predesign parameters

Tube diameter and gap distance to the tube were kept constant and are based on Hyperloop Alpha [1] proposal and a team decision in the case of the gap which enabled a reasonable range of control. The pod length was kept as a variable as well as the travel speed. Also, tube pressure was made variable as well as diffuser pressure ratio and cross section area. Regarding the propulsion system, compressor pressure ratio, compressor discharge speed, turbine pressure ratio and turbine discharge speed were made variables but their efficiencies were kept constant and set to a low value to be in the safe side. Furthermore, tube and gap friction factors and also travel distance were assumed as constant. Varying this parameters and using the models described in 3.2 all the performance actuations of the system may be calculated.

3.2 Models used defining the pre-design concept

In order to analyse the performance of the proposed system configuration a battery of simple and reasonable models are proposed.

3.2.1 External aerodynamics

The flow around the presented pod design might seem complex but, due to the simplification incurred while choosing the levitation system, our tube layout is clean and no air cushion is modeled. The basic flow patterns derive from two ways: the mass flow passing through the pod (diffuser-compressor, intermediate tube, turbine and nozzle) and the air

gap around the pod. From the point of view of external aerodynamics diffuser intake conditions, nozzle outlet conditions and mass flow process through the gap should be studied. A scheme showing flow stations is available in figure 3.1, mention will be made to this scheme during this subsection.

The first stage is to impose an absolute pressure at the diffuser inlet (station 1) in order to calculate how much mass flow travels through the compressor. The evolution between station 0 and 1 is defined as an isentropic process between the stagnation conditions upflow (0) and the inlet area and pressure condition. Using this relationship the compressor mass flow rate, and the thermodynamic properties at the diffuser inlet are obtained.

The rest of the incoming air must travel through the gap around the pod. This presents a different flow pattern known as a Fanno flow [2]. When the air enters the gap the dominant terms in the Navier-Stokes equations change from the convection dominated paradigm to a friction-convection dominated scheme. This compressible flow in which friction and air compression are relevant is well characterized for round ducts and depends on the parameter $f \cdot \frac{L}{D}$. Where f is the average friction factor in the duct, L the tube length and D the duct diameter. The proposed gap is no cylindric duct, so an equivalent hydraulic diameter was considered as a first approximation in 1-D models. Analysing the parameter, two situations appear:

- The parameter is large and the flow chokes in the gap. As the air travels between the pod and the tube wall, the shear stresses acting upon it cause a friction pressure loss. Because the air is in a compressible regime, this causes a density drop which makes the flow accelerate due to mass flow conservation. As it accelerates, if the $f \cdot \frac{L}{D}$ parameter is high enough, it may reach sonic conditions. When this occurs, the gap chokes and no more mass can travel through it.
- The parameter is small and the flow experiences a pressure loss through the gap in a subsonic process.

In either case, applying momentum conservation between the gap inlet (station 7) and outlet (station 8), the drag produced by this flow is obtained.

Likewise, the evolution from the upstream infinity conditions until the gap is calculated via an isentropic process.

Finally, at the pod's rear, the flow behaves in a manner determined by the propelling nozzle, whose stagnation pressure and temperature are calculated from the internal aerodynamics and propulsion models.

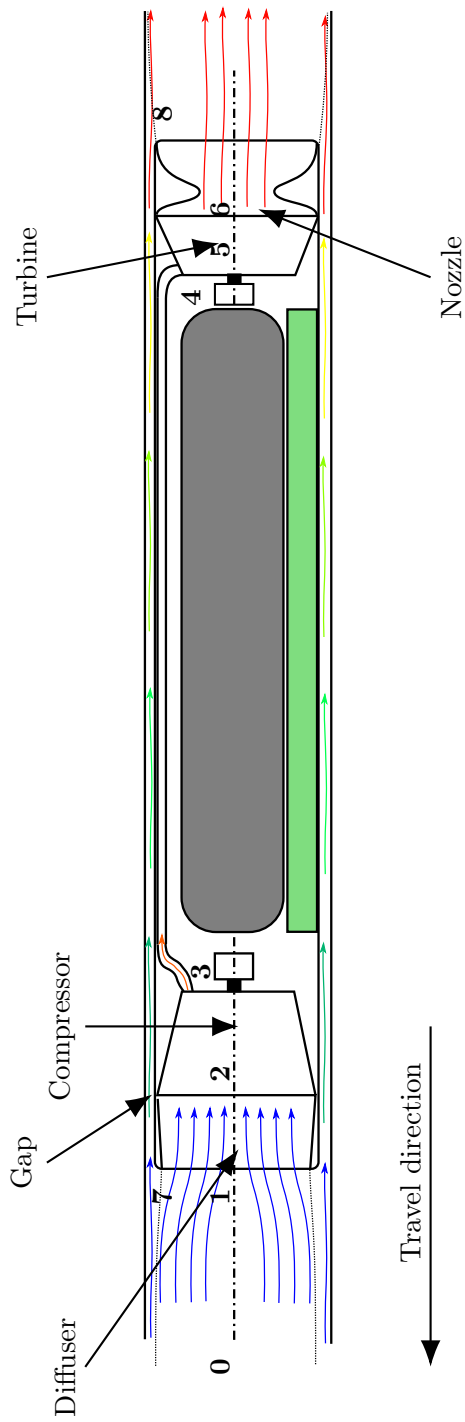


Figure 3.1: Aerodynamic stations and scheme.

3.2.2 Internal aerodynamics

The incoming diffuser flow travels through a 0-D compressor (evolution from station 2 to station 3) defined by its compression ratio and isentropic efficiency, the discharge section of it is described also by an axial velocity. This flow travels through a inner tube (stations 3 to 4) at the mentioned speed, also calculated as a Fanno flow. Finally the air enters a power turbine (evolution 5-6) defined by its expansion ratio and an isentropic efficiency to later expand into a propelling nozzle from the turbine discharge pressure until the defined tube pressure.

3.2.3 Magnetic levitation system

The initial magnetic levitation system starts as a reference permanent magnet. With a known cross sectional area and distance to a ferromagnetic surface, to which is attracted, the magnet's power per unit area is obtained through a $\frac{1}{r^2}$ law. Once the permanent magnet is characterized, a levitation unit is virtually assembled with a known magnet and an electromagnet, whose current and turn number is also an input parameter.

The levitation system consists of assemblies of several levitation units arranged in different orientations in order to control the pod's attitude and position inside the tube actively. The number of assemblies is calculated to lift the weight of the pod, and its power is derived from the current at a prescribed voltage.

3.2.4 Structure and weight

As a first approximation, the structure considered is the one of the cabin pressure vessel and a value dependant on pod kinetic energy.

The cabin is calculated as a pressure vessel made from wound carbon composite in the shape of a cylinder with spherical ends. The thickness is calculated in order to achieve a security factor of 4 treating the material as a fragile one (Tresca criteria). Once the thickness is known, the material volume, and thus, density is also known. Additionally, a 50% overhead on weight is included in this part to take into account the reinforcement for the doors and endcaps.

The term depending on vessel kinetic energy is calculated as a sacrificial braking mass in first approximation as no more data is available.

3.2.5 Propulsion system

For each component, the compressor and power turbine, the same method here described applies: Using the compression/expansion ratio, a number of stages and stage type is picked and calculated. For each stage, the cross sectional area of the airpath is used to calculate their volume as a cone trunk. The thickness of this cone depends on the type of stage considered. For each kind of stage, axial or radial, a different occupation factor is accounted. Once the volume is known, the mass is calculated using a density of a titanium compound as a reference.

3.2.6 Power systems

Through compression ratio, expansion ratio and compressor and turbine efficiencies the power available and required for each machine is known. Using this power an electric machine with a realistic efficiency of around 90% is chosen. These machines have a specific weight, as well as the power electronics. The final results from this model include: motor and generator weight, their volume, the required power from the battery and the overall system conversion efficiency.

The battery is calculated using the power required from the propulsion system, the levitation system and an auxiliary systems power budget. This power is then integrated through the duration of the travel to obtain the energy required. Moreover, a 70% depth of discharge is used and a 25% safety margin is also considered. Finally, using the power density, energy density and specific cost, the weight, volume and cost of the battery are obtained.

3.2.7 Cabin arrangement and payload

Three cabin densities are considered through this model, in each one the pitch between seats and the volume required per passenger is prescribed. Using the pod dimensions the number of passengers is calculated, including the payload weight and cabin interior trimming and seating weight.

3.3 Optimization

The previously described models were implemented in Excel spreadsheets, and integrated in modeFrontier. modeFrontier uses different configurable nonlinear optimization algorithms, including genetic based ones, which can be applied to a wide range of engineering related system implementations. The algorithm of choice was MOGA-2, a multiobjective genetic optimization algorythm [3].

3.3.1 Cruise configuration optimization results

The goal of this optimization was to obtain the minimum required energy for the travel while keeping the air tube that guides the air from the compressor to the turbine small enough for the cabin to fit while having enough space for both the batteries and the cabin. The requisite for the design was a minimum thrust to maintain pod velocity.

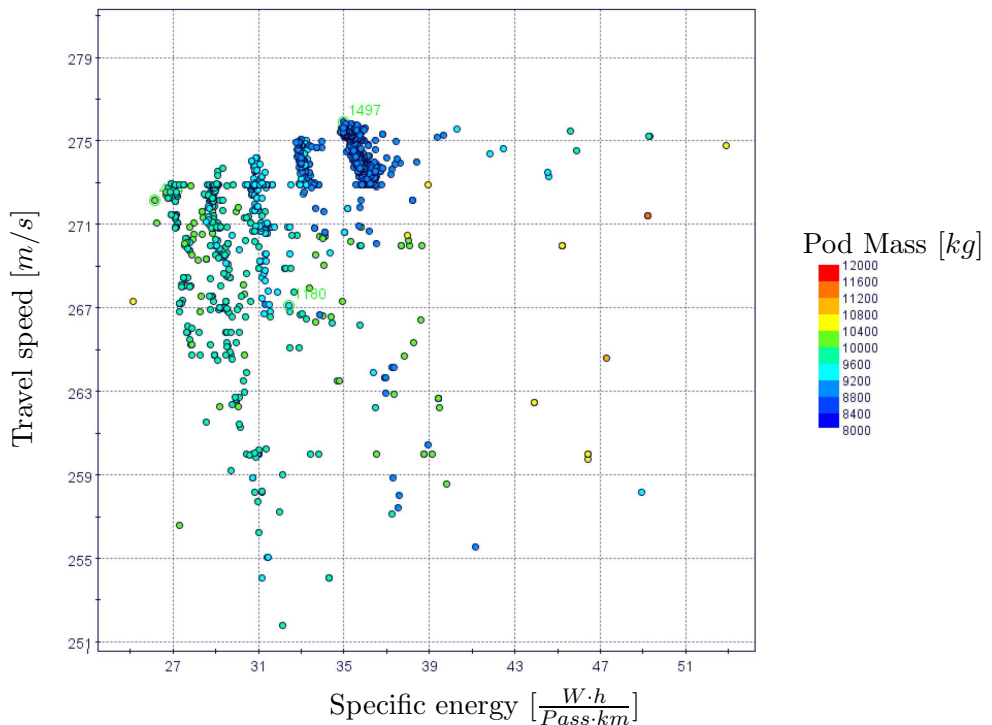


Figure 3.2: Cruise case optimization results.

This results take into account just the energy required to maintain the pod speed constant, a general trend is clear. Seeing the top of the different bands of possible results, an increasing trend appears, so is conluded that: the fastest the travel, the more energy is required to move the pod. Mass values on the other side decrease as a general rule with speed since turbine and compressor stage numbers change and make for a more compact solution. Moreover, turbine energy recovery is greater at higher speeds due to higher

compressor ratios and lower losses. Additionally, very little points are found past a peak speed of around 276 m/s . This fact is due to the choking of the diffuser at sonic conditions. In this stage, it has not been studied the effects of such a high speed axial velocity on the compressor. It is possible that the compressor would choke as the diffuser does if no measures are incorporated in order to reduce the flow-blade relative speed. A simple solution is the use of a IGV stator before the compressor inlet.

3.3.2 Acceleration configuration optimization results

The goal of this optimization was to obtain the maximum autonomous acceleration for the pod with the minimum required energy. In this calculation a phase of mechanical traction at low speeds is included to improve pod speed-up times.

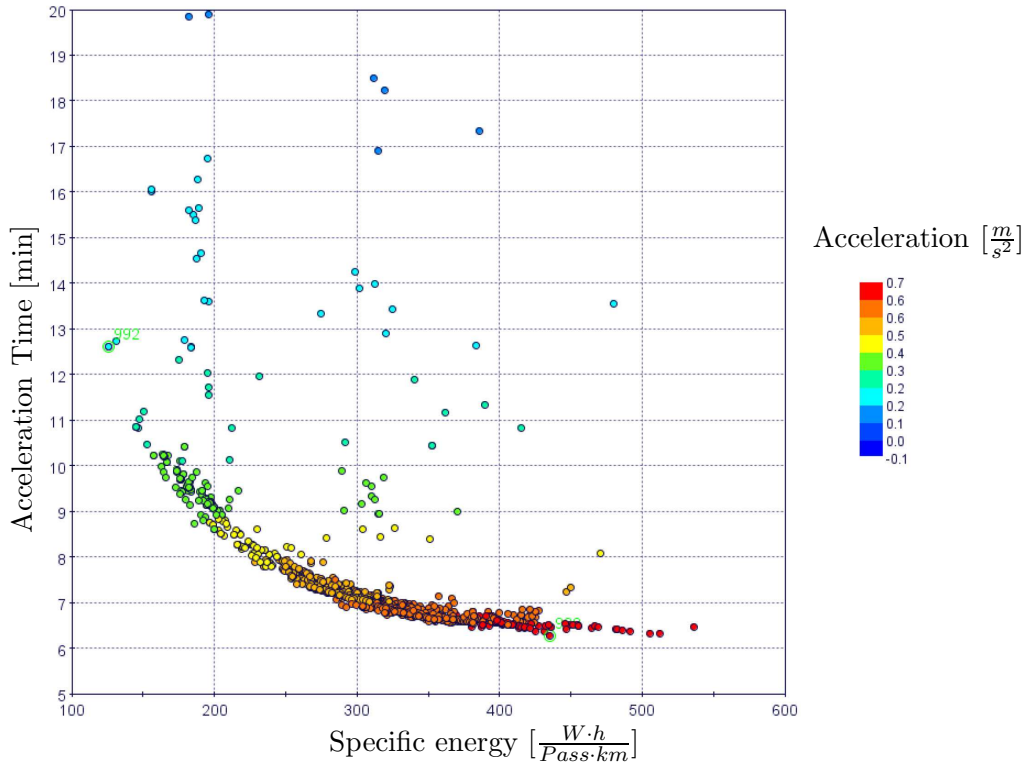


Figure 3.3: Acceleration case optimization results.

In this case, the results on figure 3.3 are clear, in order to obtain an autonomous acceleration for the pod in a shorter time, the specific energy increases exponentially. As it can be seen, the values in the specific energy change by an order of magnitude compared to the values in figure 3.2. This imposes a much bigger pod mass value and battery requirements to our system, further discussion on this is described in chapter 7.

3.4 Chosen pre-design point

The elected point for this development is defined by the following dimensions and parameters:

Parameter	Value	Units	Parameter	Value	Units
Pod Length	13.9	m	Tube diameter	1.79	m
Gap distance	0.05	m	Tube pressure	100	Pa
Tube temperature	300	K	Travel speed	260	m/s
Diffuser suction	0.9	[\cdot]	Diffuser section ratio	1	[\cdot]
$(\pi_C)_{t/t}$	26	[\cdot]	$(\eta_C)_{t/t}$	0.7	[\cdot]
$u_{C_{Out}}$	345	m/s	f_{Duct}	0.01	[\cdot]
L_{Duct}	10	m	$(\pi_T)_{t/t}$	15	[\cdot]
$(\eta_T)_{t/t}$	0.7	[\cdot]	$u_{T_{Out}}$	414	m/s
f_{Gap}	0.02	[\cdot]	Travel length	600	km
Pod mass	9802.5	kg	Specific energy	27.76	[$\frac{W \cdot h}{km \cdot pass}$]

Table 3.2: Optimal dimensions and parameters

4

Detailed Study

4.1 Levitation system

In order to make the pod hover, an innovative system has been designed and it will be depicted in this chapter. Instead of using an special aluminum track as required by rotating cylindric Hallback-configured eddy current magnetic levitation systems, the approach depicted uses the vaccum tube directly to hover the pod. This works by attracting the whole pod to the upper part of the tube.

Levitating such a mass requires a powerful electromagnet and, consequently, a high power demand. The power requirements can be easily reduced by means of incorporating a hybrid solution: a permanent plus an electromagnet unit. On the other hand, this approach requires a robust control system since the system is inherently unstable.

4.1.1 Physical magnetostatic modelling and small real-life model

As this is a complex nonlinear system, some approximations have been taken into account. The system can assumed as the sum of three forces:

1. Weight: this force is the simplest one: the mass times the gravity.
2. Permanent magnet force: this force may be complicated to estimate but is known that is function of $\frac{1}{r^2}$, so is assumed this force can be described as a constant k_1 times $\frac{1}{r^2}$.
3. Force due to the electromagnet: this force can be split into two factors: Magnetic factor: it has been modelled as the permanent force (with a different scaling constant k_2) Electric inertia: it is modelled as an exponential $\exp^{-\frac{R \cdot t}{L}} / L$.

If linearization is done in a defined setpoint gap distance, r_0 , chosen as 5 cm in this design, it is possible to obtain a very simple expression, as the Taylor series expansion for $1/r^2$ around r_0 is $-1/(r_0)^3 \cdot r$. Merging all the values obtained in the linearization and applying a Laplace transform to Newton's Third Law, the following equation can be derived:

$$k_1 \frac{1}{L + R \cdot s} r(s) + k_2 r(s) - mg = m r(s) s^2$$

This system has 3 poles, two in the stable zone and one in the unstable zone as the root locus diagram shows (figure 4.1), so it is not possible to do a simple proportional control, all the terms of a PID controller are needed [4].

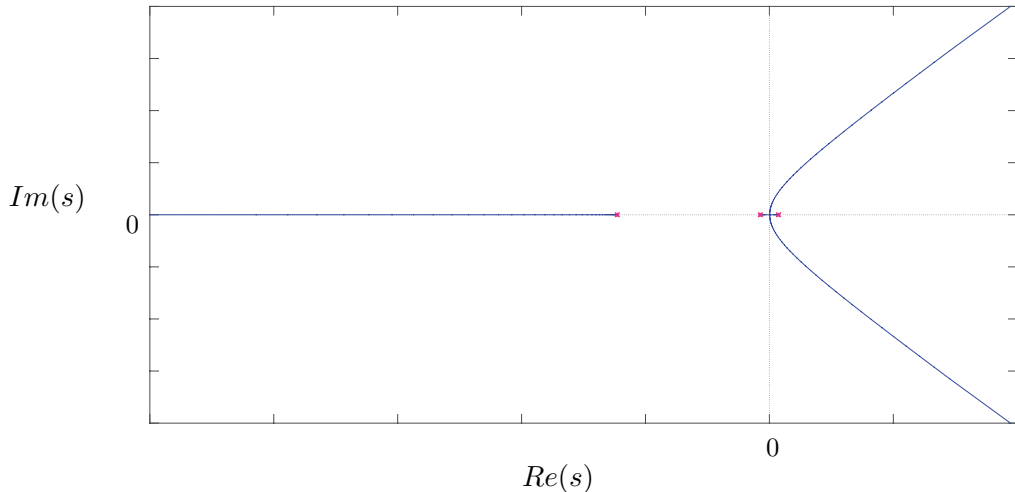


Figure 4.1: Root locus for the levitation system.

Next place, a dynamic model is constructed using MATLAB Simulink. The model can be seen in figure 4.2, and in this calculation the sensor gain k_3 has been considered to be unitary. With the aid of this model, the tuning parameters of the PID controller can be tested before testing a small real model.

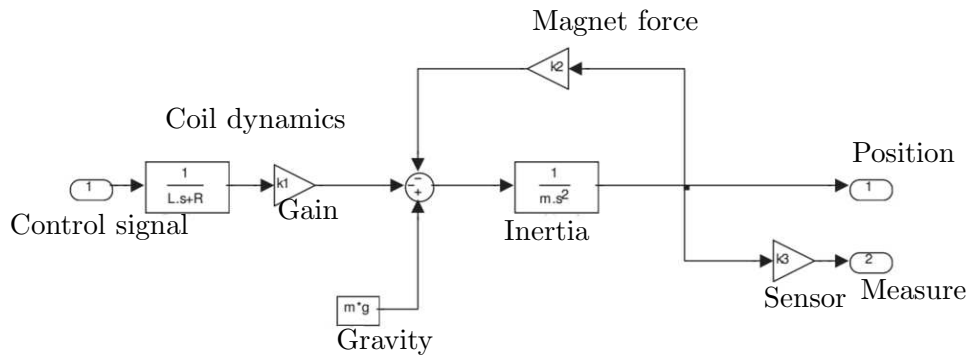


Figure 4.2: Simulink dynamic model.

The constant values can be obtained experimentally or theoretically if all the parameters of the magnetic devices and the setpoint are known. Once the system is identified, tuning the parameters of the PID is the final step. Despite theoretically they can be estimated, a final experimental tuning has to be done to ensure the optimal values.

In order to verify the previous assumptions, a small model has been chosen. The model consisted of a levitating cylindric permanent magnet with a mass of around 0.2 kg which was attracted to another permanent magnet mounted on the frame. The control action was provided by a electromagnet coil, located at the top of the system. Additional

stabilizing magnets are located at both sides of the levitating specimen (see figure 4.3). The values of the constants for the PID tuning of the model are:

- $K_p = 8$
- $T_d = 0.35$
- $T_i = 0.4$

Finally, an unstable system has been controlled and it has become stable:

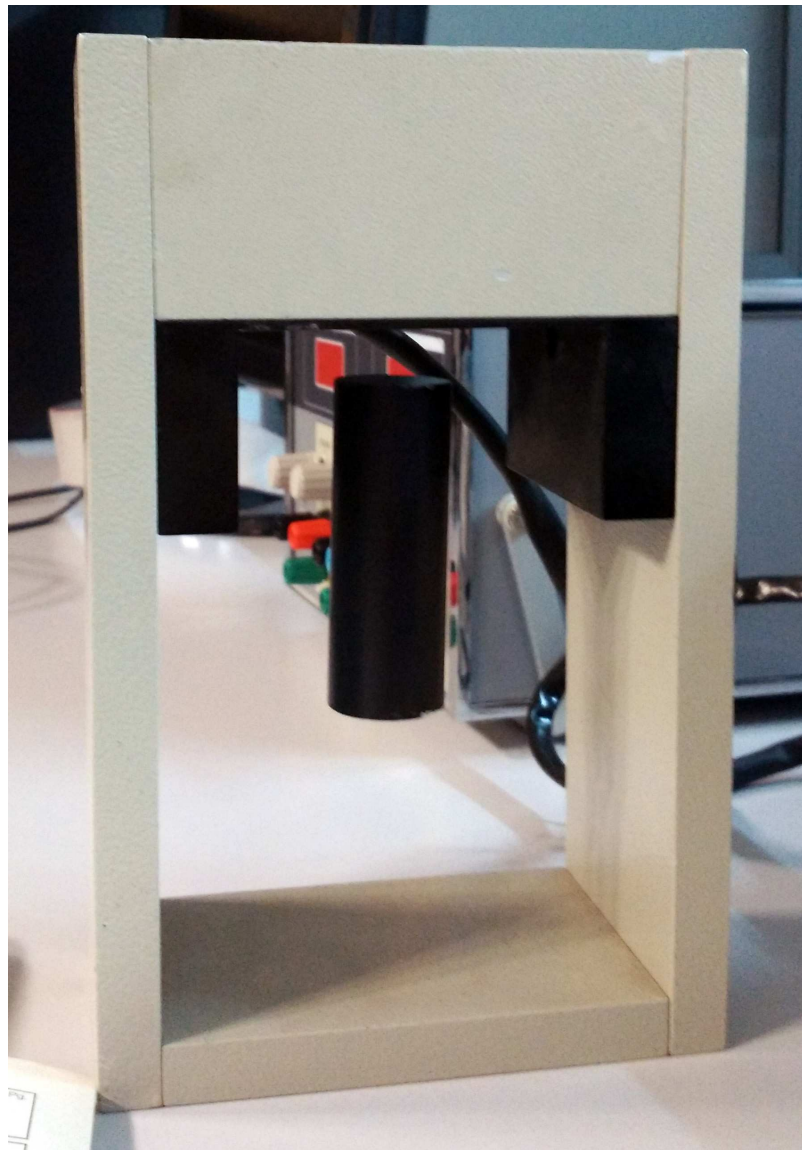


Figure 4.3: Model system used to test the modelling approach.
Note the internal cylinder is floating in mid-air.

4.1.2 Magnetostatic 2-D configuration analysis

For the system to behave in a proper way and for the sake of the controllability, both, upwards force and downward have to be achievable with the proposed system. The upwards force is provided by the permanent magnet and the electromagnet working in the same direction as the permanent magnet. The downward force is provided by gravity and the lack of magnetic attraction created by the electromagnet working against the permanent magnet's magnetic field.

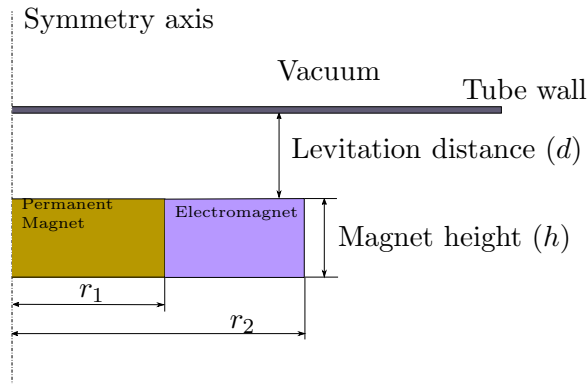


Figure 4.4: Unit configuration 0.

As a first approach, a simple 2-D concentric magnet configuration was elected, see picture 4.4. With this configuration, a sweep of different excitation currents were applied on the electromagnet. The results of this study show that there is no way for the electromagnet to completely cancel the permanent magnet field and, thus, force. As a second thought, the positions of the permanent and electromagnet were exchanged but this produced no relevant changes to the results.

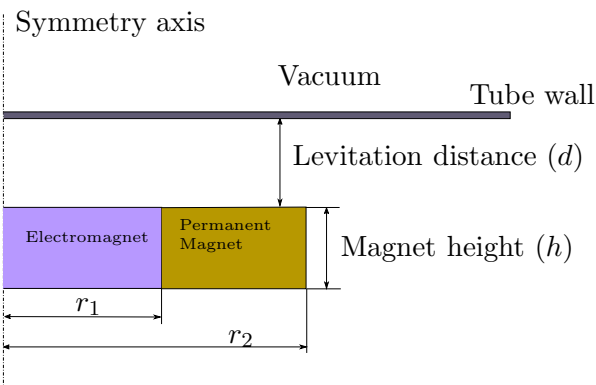


Figure 4.5: Unit configuration 0 reversed.
Magnet and electromagnet positions exchanged.

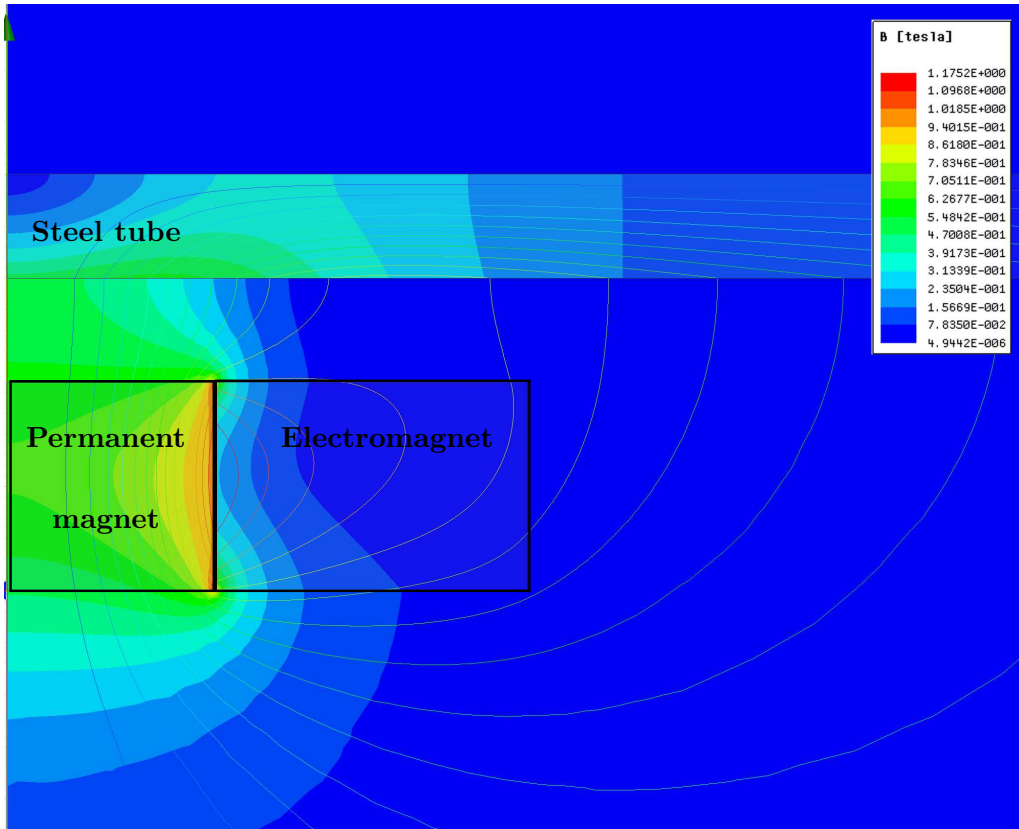


Figure 4.6: EM simulation results for the configuration 0.
Note the low flow deflection on the EM.

This results were logical because of the shape of the force lines in the airgap between the magnet and the steel surface of the tube. In order to cancel the force from the permanent magnet a stack approach was taken as can be seen in figure 4.7. In this case, the electromagnet was able to reduce the magnet's power by almost 90%, making this setup a viable configuration.

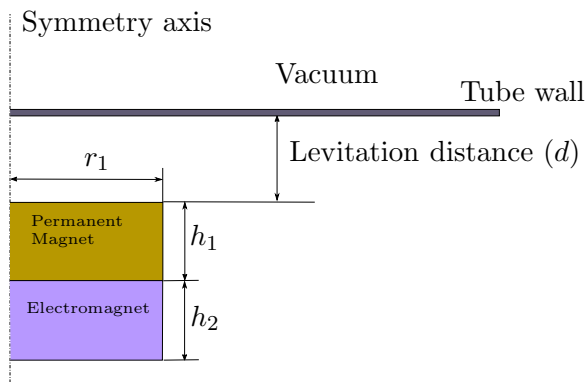


Figure 4.7: Unit configuration 1.

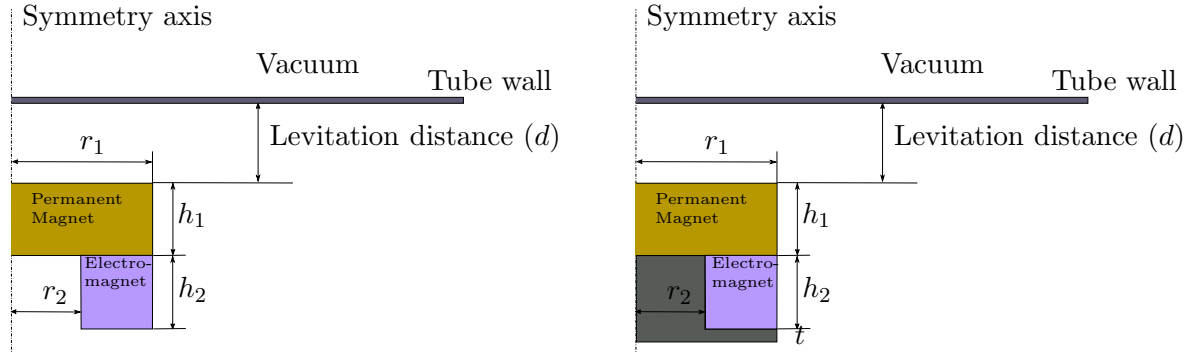


Figure 4.8: Unit configurations 1 – v1 and 1 – v2.

After having solved the problem of cancelling the magnet force, a refinement of the configuration was done in order to reduce the required current for the electromagnet. In the first place, the coil was reduced and shaped in an empty solenoid fashion (see figure 4.8 left). This step reduced the current required by 25%. Secondly, by adding an internal ferromagnetic core to the coil assembly as depicted in figure 4.8 right, the current required was cut by another 10% and the force applied by the system was increased by a factor of 1.1. This was due to the shorter path of the magnetic field and consequent reluctance reduction. A comparison between the base case and the optimized one for the field strength can be seen comparing figures 4.6 4.9.

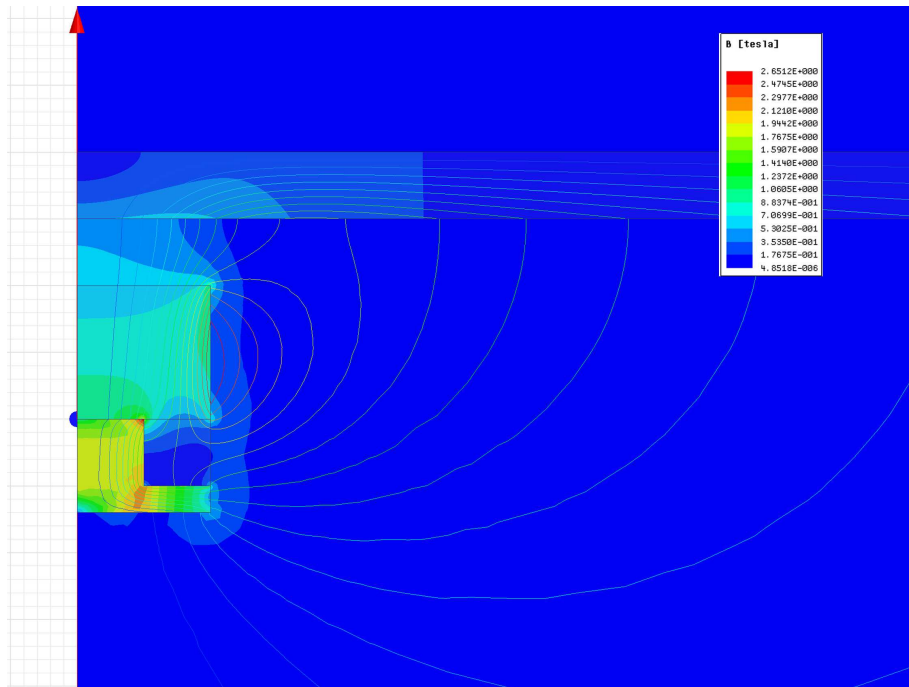


Figure 4.9: EM simulation results for the configuration 1 – v2.
Note the high flow density near the core of the coil.

4.1.3 Magnetostatic 2-D parametric configuration analysis

After deciding the magnet arrangement configuration, a parametric study of the selected setup was performed. In this case, the geometry was further complicated by means of a rounded tube wall to achieve a more realistic result.

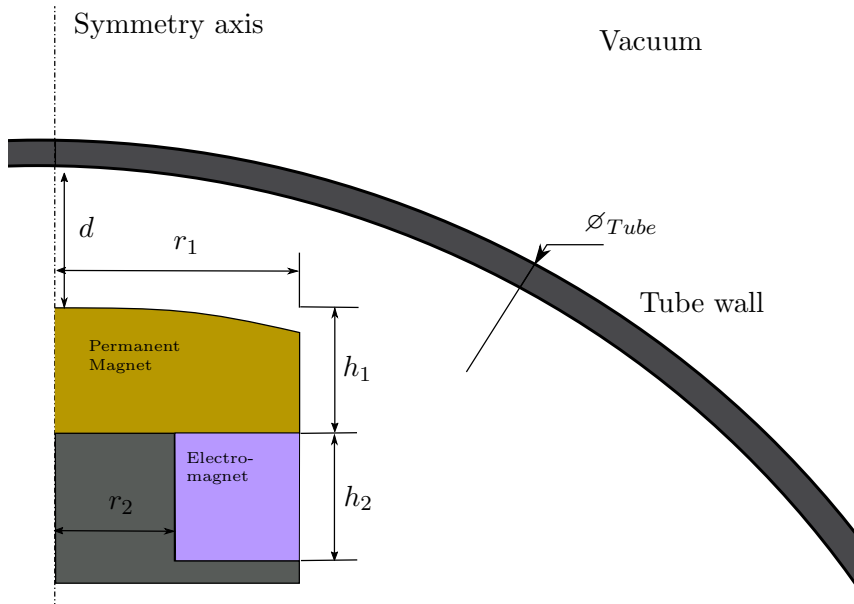


Figure 4.10: Parametric setup for magnetostatic configuration.

In figure 4.10, the different parameters varied are depicted. All results in force are referred to a reference case which corresponds to:

- $h_1 = 0.1 \text{ m}$
- $h_2 = 0.1 \text{ m}$
- $r_1 = 0.2 \text{ m}$
- $d = 0.05 \text{ m}$
- $I_{\text{Magnet}} = 0 \text{ A} \cdot \text{turn}$

These values were selected because of geometrical concerns and size restrictions.

The different results from this study are described here:

- Change in r_1 ranging $[0.01, 0.2] \text{ m}$: the force of the magnet varies almost linearly with the magnet's radius. This is not a physically sound result. In theory, the force a magnet exerts on a ferromagnetic surface or other magnet is proportional to its cross sectional area. In this case the force variation suffers from the restriction in the magnet's geometry which makes it concentric with the tube (see figure 4.10).

- Change in h_1 ranging $[0.1, 0.5] \text{ m}$: in this case, the force varies linearly with magnet thickness. This result is not easily correlated with classical physics.
- Change in d ranging $[0.01, 0.1] \text{ m}$: as expected, this result follows a $\frac{1}{d^2}$ law.
- Change in coil intensity between $2 \cdot 10^5$ and $-3 \cdot 10^5 \text{ A} \cdot \text{Turn}$: the unit force varies with intensity in a parabolic law. It presents a global minimum for a given value which varies with distance and it grows indefinitely with it.

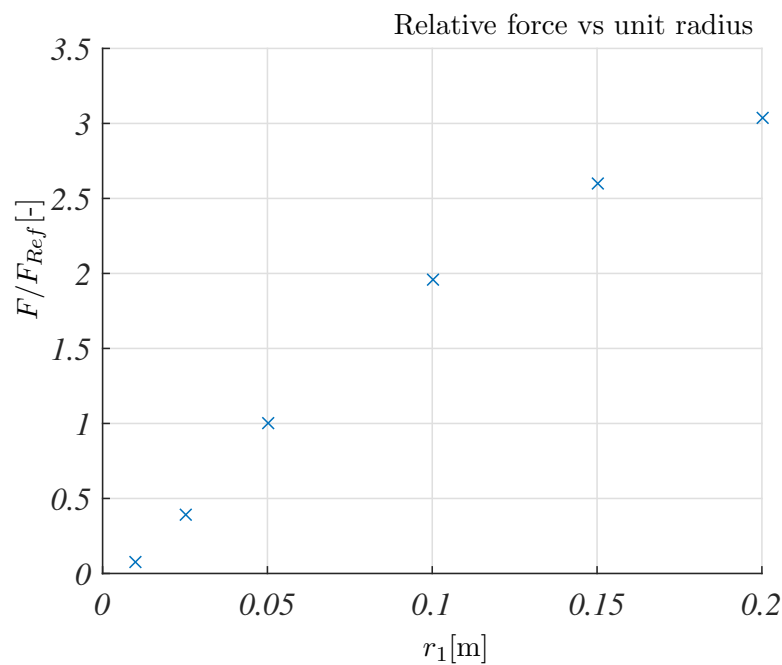


Figure 4.11: Force vs magnet radius parametric study.

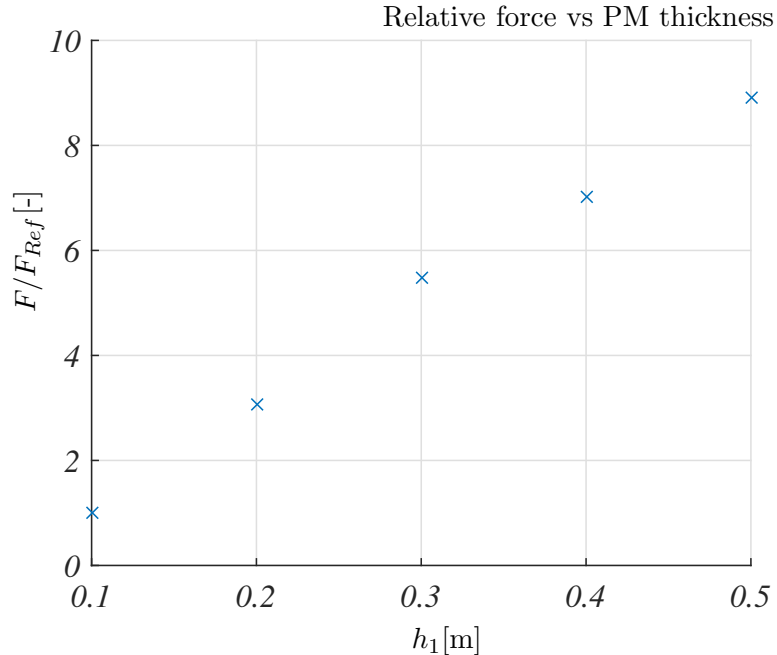


Figure 4.12: Force vs permanent magnet thickness parametric study.

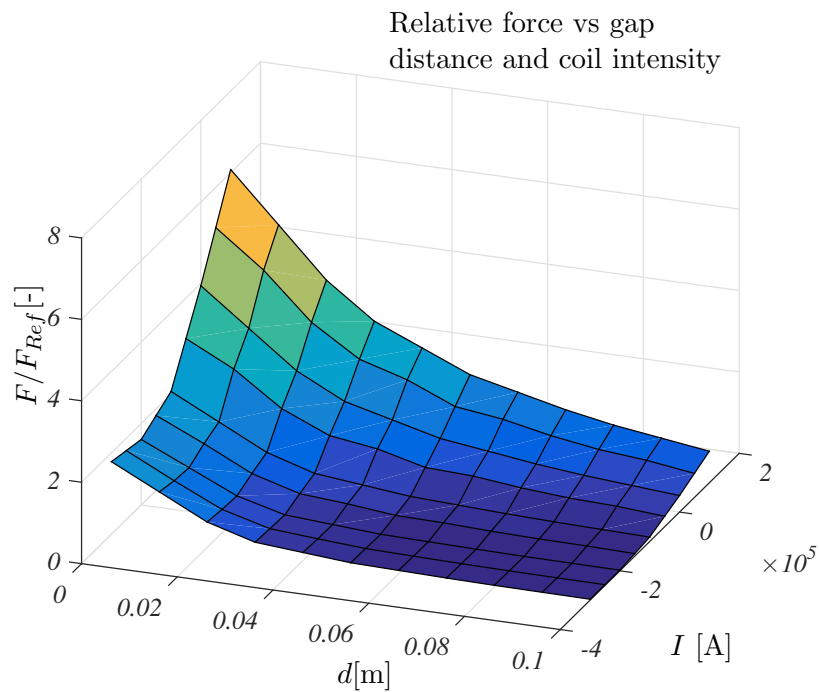


Figure 4.13: Force vs gap distance and coil intensity parametric study.

After this results, a magnet size and thickness was elected and the unit was charac-

terized for further calculations. The final dimensions of the unit can be seen in the next table.

Parameter	Value	Unit
Unit radius (r_1)	0.2	m
Unit height ($h_1 + h_2 + t$)	0.25	m
Permanent magnet height (h_1)	0.1	m
Electromagnet internal radius ($r_1/2$)	0.1	m
Core thickness (t)	0.05	m
Electromagnet maximum intensity	$\pm 3 \cdot 10^6$	$A \cdot turn$

Table 4.1: Final levitation unit dimensions and parameters.

4.1.4 Magnetostatic 3-D confirmation analysis

In addition to the previous calculation, a confirmation 3-D analysis was performed. The unit dimensions and current used are the same as the reference 2-D case, the tube length was set to 5 m in order to simulate an infinite tube. Several field distributions are depicted in figures 4.14 and 4.15. Figure 4.14 shows a magnetic field intensity distribution on the midplane of the levitation unit. Figure 4.15 depicts the same case magnetic field intensity but in this case at the surface of the tube and the unit. For both cases, the parameters of the unit are the same as the ones shown in table 4.1 and the tube diameter was set to 1.8 m.

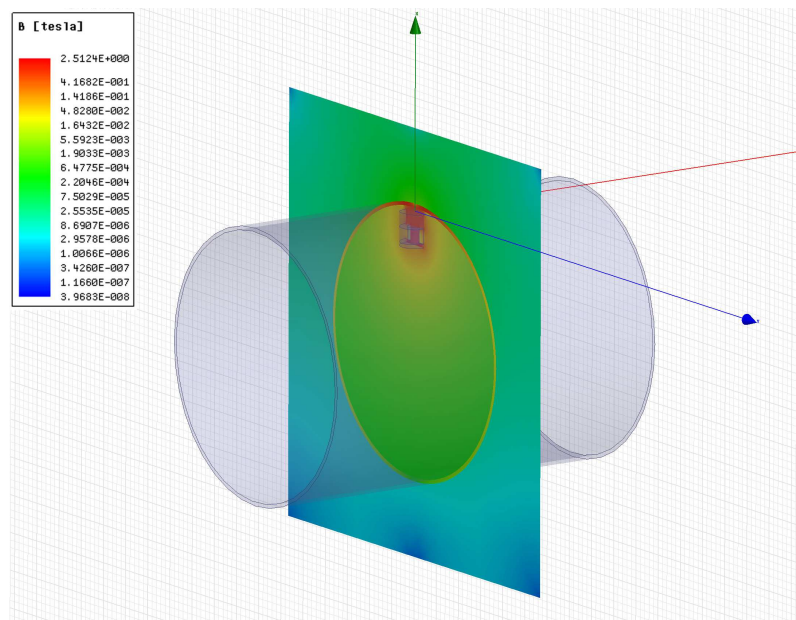


Figure 4.14: EM simulation results for the 3D setup.

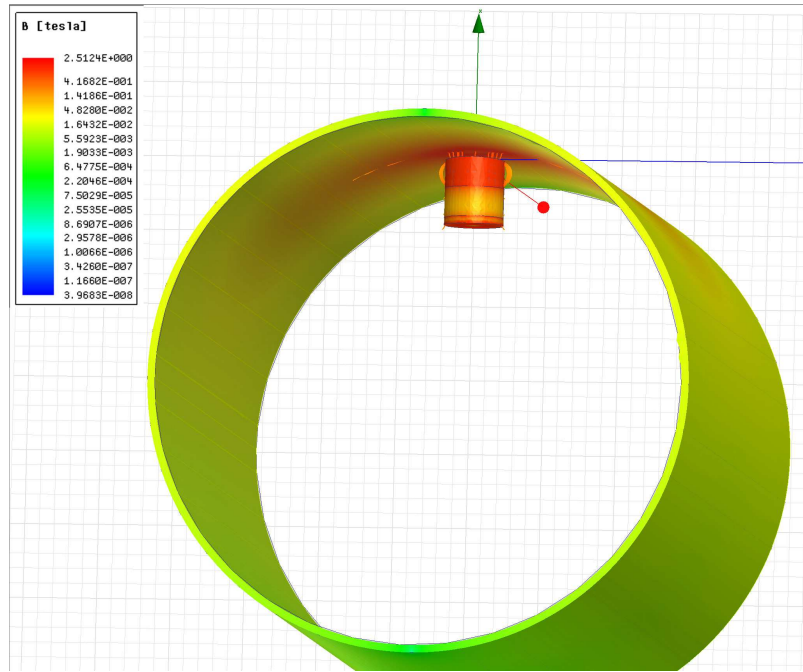


Figure 4.15: EM simulation results for the 3D setup.

4.1.5 Magnetodynamic 3-D simulation

As a final analysis, a 3-D magnetodynamic simulation was done in order to predict tube induced currents and magnetic fields which could lead to a drop in attraction force. The dimensions were inherited from the static 3-D case and the travel speed was set to 260 m/s.

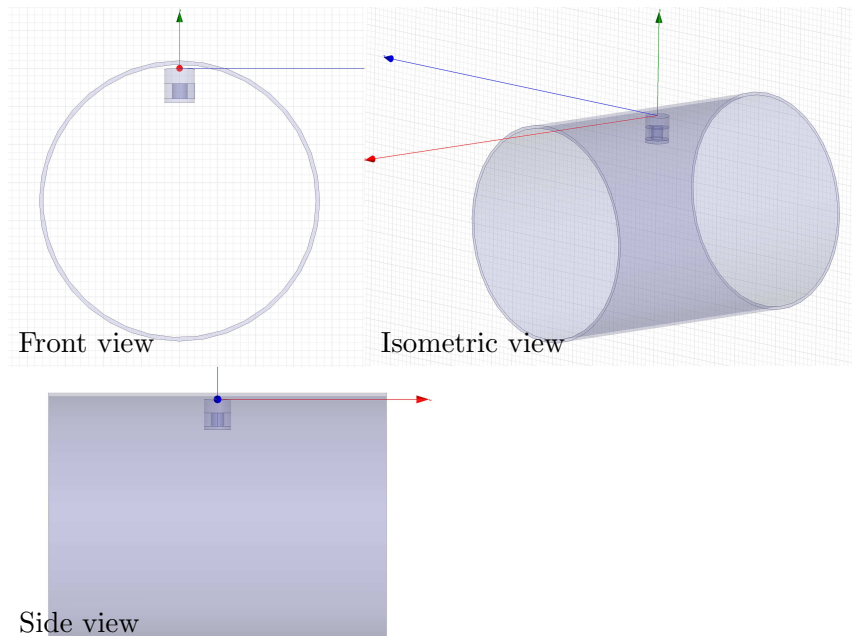


Figure 4.16: 3D case geometry.

The analysis geometry, depicted in figure 4.16, includes a short section of the tube and the whole 3-D levitation unit with the same dimensions as the static case. This analysis was performed at cruise speed since this is the critical phase for the levitation system effectiveness. The results of this case are represented in figure 4.17 and figure 4.18. The first represents the evolution of the unit pull force on the tube as a function of simulation time, the second one depicts a timestep magnetic field distribution over the tube.

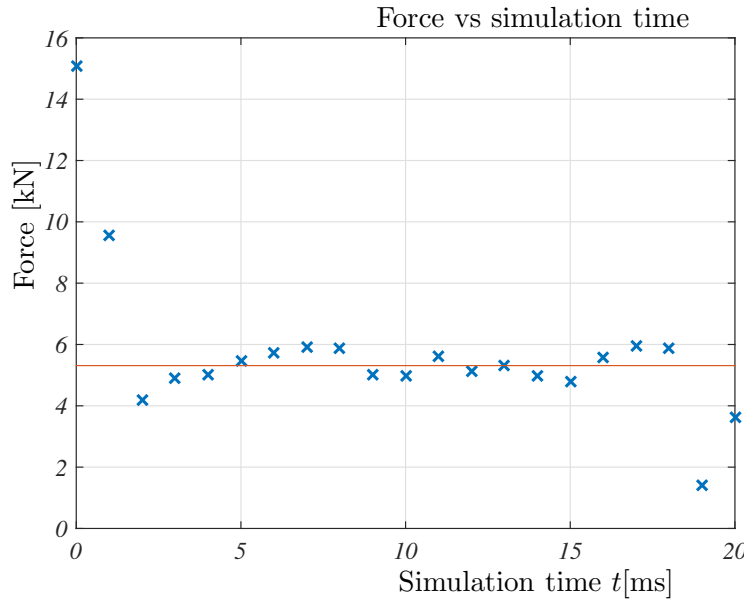


Figure 4.17: Magnet pull force vs simulation time.
The red line is the mean value of the central points.

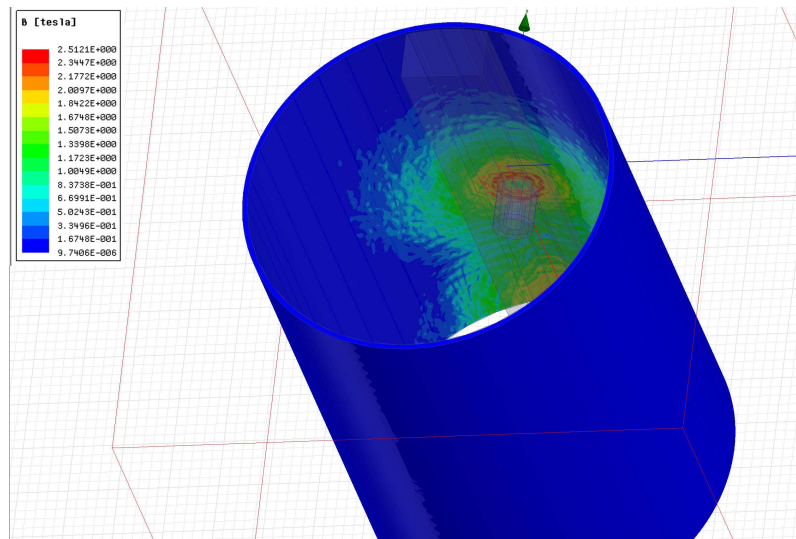


Figure 4.18: EM simulation results for the 3D dynamic 3D setup.

As can be seen, the force value remains fairly constant along the simulation time, excluding the initial and final timesteps and presents small variations due to mesh and simulation configuration. In the ends of the tube, the unit is not completely inside its domain, so the results are not completely valid. As expected, the force value decreases in this case compared to the static case. This fact is due to Lenz's law, the moving magnet induces a magnetic field in the plate of the tube which opposes the magnet's.

This behavior can be overcome by changing the distance between the pod and the tube and also by means of changing the current flowing through the electromagnet.

4.2 Aerodynamic and propulsion system study

As mentioned in section 3, the proposed design uses a front facing compressor to move the air, through a tube, to a rear nozzle in which it expands producing thrust. In order to verify the feasibility of the design, a detailed flow analysis is in order. This analysis would also improve the pod's external aerodynamic model. This development is going to be based in a CFD analysis of the flow around the pod placed inside a tube and will be compared against the pre-design calculations for further integrations.

4.2.1 CFD pre-processing

Two sections are described here: the mesh generation and mesh independence study for a 2-D case in the first place, and the mesh generation and independence study for a 3-D setup.

2-D Cases

Geometry and mesh independence study

This process starts with the generation of a suitable geometry in ANSYS DesignModeler. This geometry is parametric, so changes can be made automatically and also manually if needed. The first CFD studies are going to be 2-D axisymmetric cases. The detailed geometry can be seen in figure 4.19 and corresponds to the parameters shown in 3.2. Most of the geometry consists of straight lines, but two mating arcs have been incorporated to ease the singularities that a sharp corner would have caused from a numerical perspective. The upstream length is a function of tube diameter, being set to a value of 10 times the tube diameter. This value was of 20 times the tube diameter for the case of the downstream length. These values have been chosen according to typical free-flow CFD aerospace derived analysis and previous team experience.

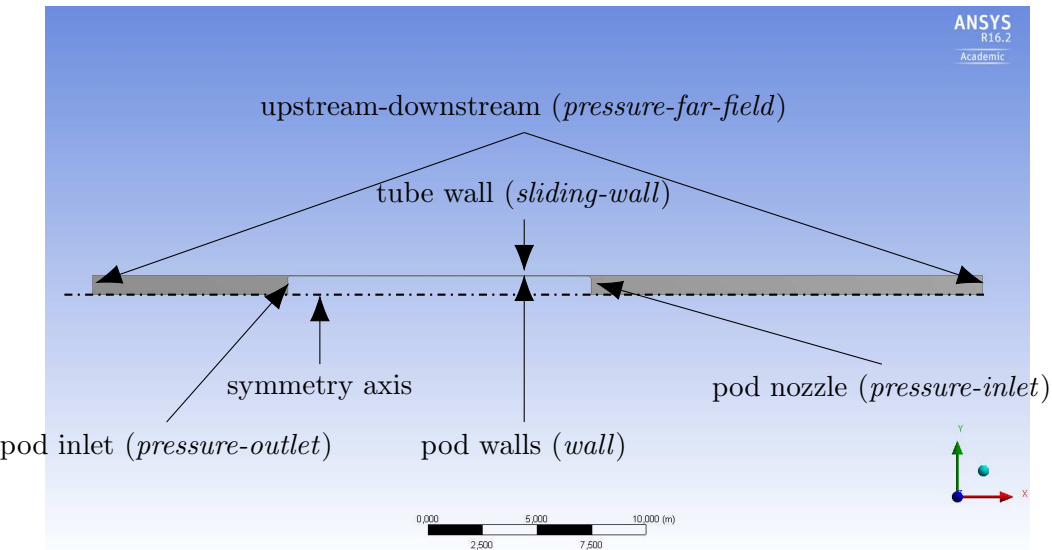


Figure 4.19: 2-D parametric CFD geometry domain with boundary conditions.

After the geometry is generated and adequately parametrized with the aid of the Excel component in ANSYS Workbench, it is time to generate the mesh. This mesh must be fine enough to visualize flow phenomena in the gap, but coarse enough to be light and easily generated due to the limited time available. Before selecting an adequate mesh size a mesh independence study was performed using different settings for the sizing controls. The meshing scheme selected was a predominant quadrilateral one because of the quicker convergence rate this type of meshing presents as it is predominantly aligned with flow patterns. Another advantage of this kind of mesh is the lower element count for a given domain size and mesh resolution.

The main sizing controls were a contact sizing of prescribed dimension, both in the pod side, and tube side of the gap and two sphere of influence type sizing restrictions near the compressor intake and the nozzle.

Varying the sizes mentioned, 4 different meshes were generated and were used to calculate a flow test. The test only simulated the compressor intake and upstreams of the pod. For the mesh independence calculations, a set of boundary conditions was applied. The upstream and downstream of the domain were set to *pressure-far-field*, the compressor inlet was set to *pressure-outlet*, the tube wall was configured as a moving wall and the rest of the geometry was set to wall with the exception of the main symmetry axis. From this calculation, two values were used to estimate mesh independence: compressor intake mass flow rate and drag coefficient of the pod.

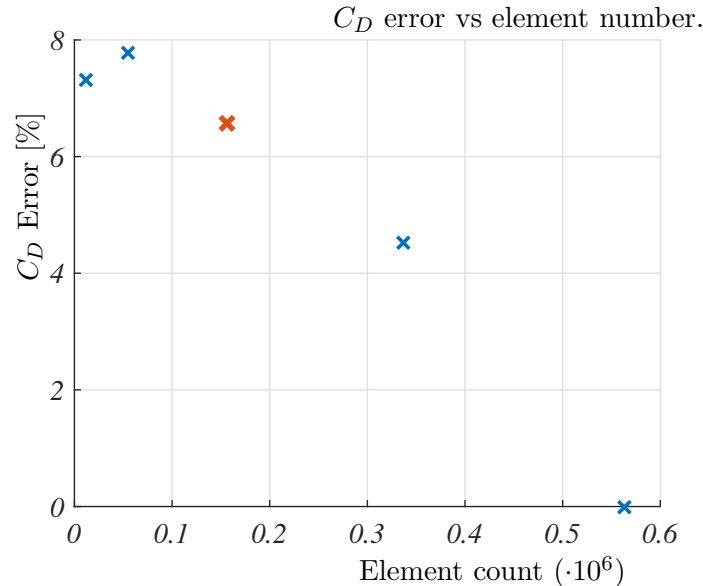


Figure 4.20: Mesh independence study: drag coefficient.

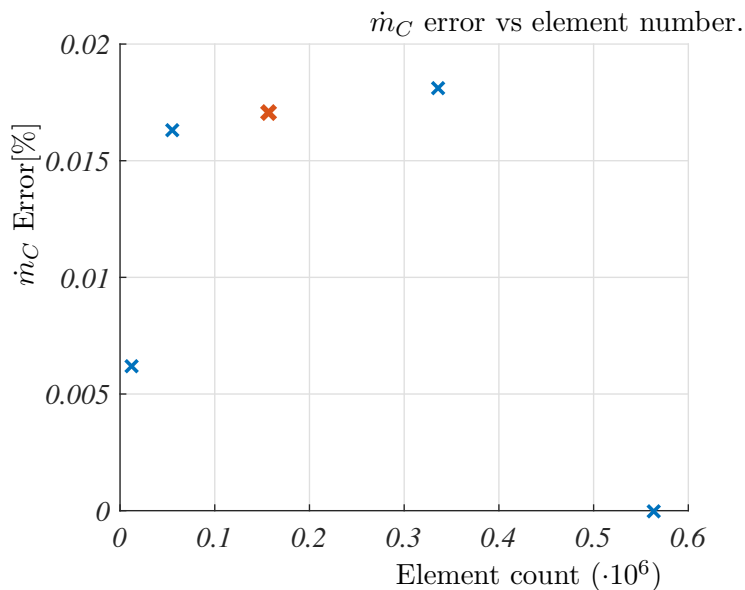


Figure 4.21: Mesh independence study: compressor mass flow rate.

In the figures 4.20 and 4.21 this result is presented. It is clear to notice that, although the trends do not match the usual result from a mesh independence study, the actual values are really close. In the case of the mass flow value for the compressor, the error accepted when using the coarsest mesh and using the finest as real value is less than 0.5%, although for the drag coefficient the error values are larger this fact is partially due to the low value of this coefficient.

The main conclusion drawn from this mesh independence case is that the finer meshes are not worth the extra calculation time and disk space required. So it was decided to use an intermediate mesh of roundly 150k elements. Different shots of the mesh details are pictured in figures 4.22, 4.23 and 4.24.

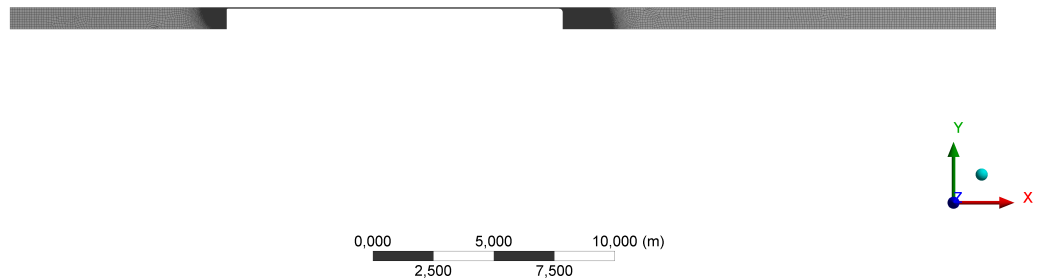


Figure 4.22: 2-D mesh: overall view.

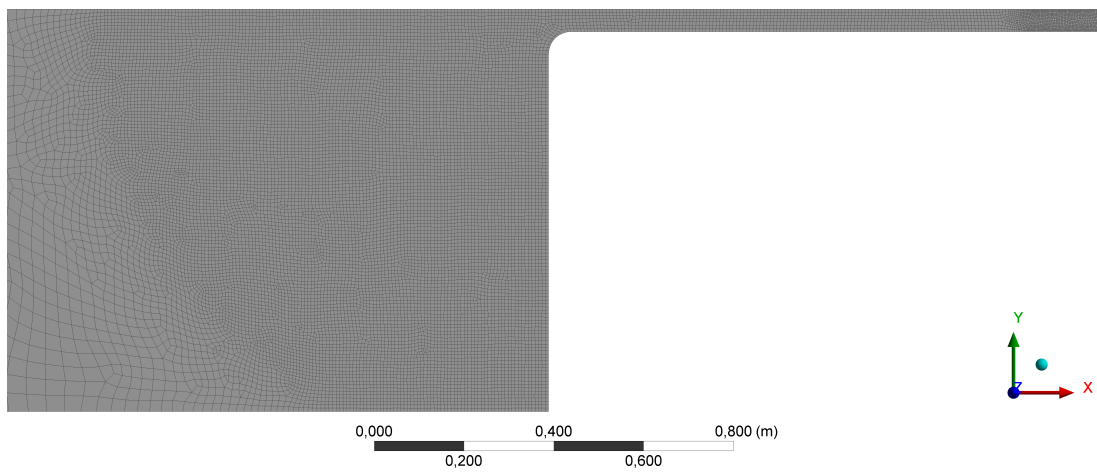


Figure 4.23: 2-D mesh: inlet detail.

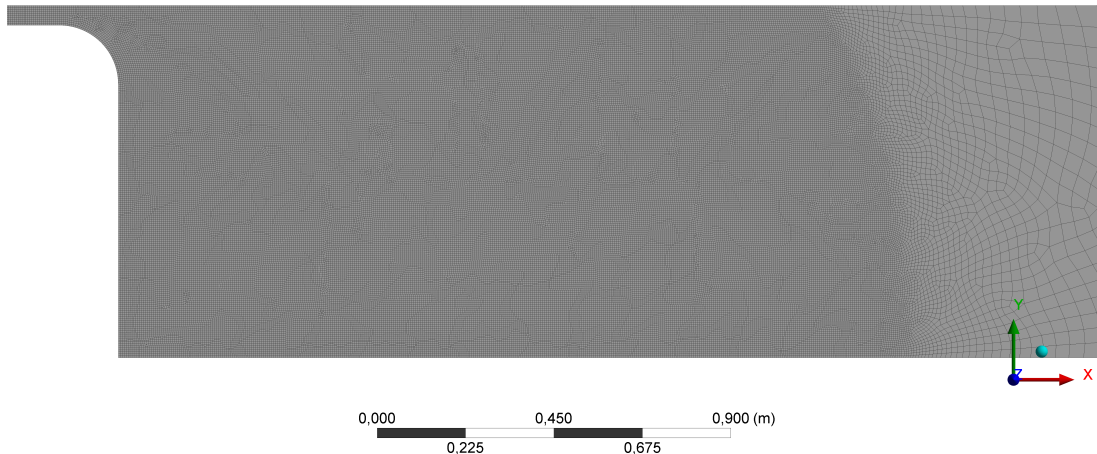


Figure 4.24: 2-D mesh: nozzle detail.

This new mesh was generated and tested with the case from the mesh independence study and, as expected all values were inside the expected error ranges as can be seen in figures 4.20 and 4.21 as the red marked point in the charts.

FLUENT setup and boundary conditions

With the mesh generated, the final boundary conditions were set in the next place. For the kind of speeds required for the pod, a traditional pressure-based incompressible analysis was not feasible. A pressure-based compressible scheme of solution was used together with compressible gas behavior for the air and temperature dependant viscosity (Sutherland's Law). Both these last models require the solver to use the energy equation in the calculations as well as the boundary conditions do. The chosen turbulence model was the k-e model with enhanced wall functions as this represents a compromise between a more complex model, calculation speed and stability. Also, to avoid errors with the gauge pressure, the operating conditions tab was filled with a value of 0 Pa. For the upstream and downstream boundary conditions a *pressure-far-field* condition with prescribed Mach number, pressure, and temperature was employed according to the design parameters. At the compressor inlet a *pressure-outlet* with prescribed pressure and backflow direction vector. For the nozzle, a *pressure-inlet* type boundary condition was used. In this case the parameters were the total pressure and total temperature of the nozzle, which were iteratively adjusted in order to match compressor and nozzle mass flow rates. In the last place, the tube wall was configured to a sliding wall in order to simulate the relative movement between the pod and the wall of the tube. The different settings of the boundary conditions were exported as parameters in order to give them expressions and values inside ANSYS Workbench for further parametric study. A particular case was the wall slide velocity, which was calculated using the tube Mach number and speed of sound at the tube conditions mentioned before.

After the boundary conditions, several monitors were set up in order to assess calculation convergence, finally was chosen to limit the iteration number per calculation instead of using monitor-based convergence criteria due to numerical oscillations and poor numerical convergence. Despite this fact, physical convergence was achieved for each case by means of surface based controls such as compressor mass flow rate, drag coefficient and nozzle mass flow rate.

Finally, inside ANSYS Workbench Response Surface component, the different design points were tagged to exporting so as to have the different sets of data available for analysis.

4.2.2 3-D cases

Geometry and mesh independence study

For the 3-D mesh, a revolution operation was applied to the previous 2-D surface in which several divisions were made in order to apply different mesh sizing conditions and methods.

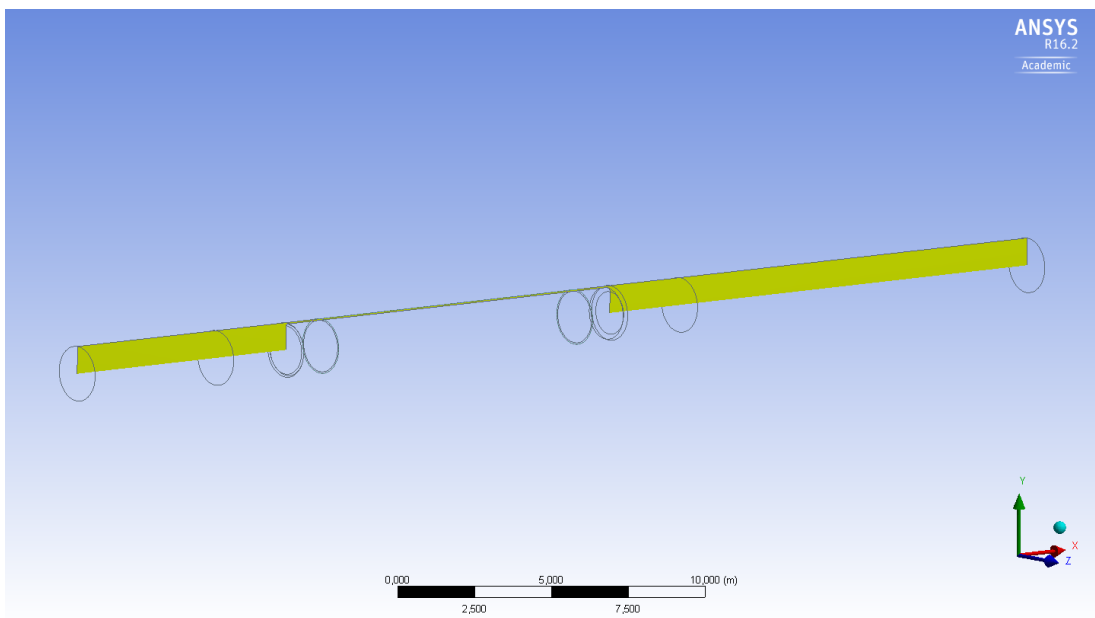


Figure 4.25: 3-D parametric CFD geometry domain.
Note the previous 2-D geometry section highlighted in yellow.

In this case, the mesh resolution must be lowered in comparison to the 2-D setup. Despite this fact, the element number in the case of the coarsest mesh was around 2 million elements. The sizing controls applied in this case include a pod wall element sizing, compressor and nozzle element size controls, minimum overall mesh size and a mapped face meshing scheme for the pod wall surface and tube wall. Unexpectedly, ANSYS Mesher did not accept the mapped face meshing so it had to be discarded for this setup.

Three different meshes were generated for this purpose using the same boundary conditions as described for the 2-D case, a coarse mesh with around $2M$ elements, a medium

mesh with $4.5M$ elements and a fine mesh. For solution independence, both compressor mass flow rate and pod drag coefficient were taken into account. It was decided that the effort required in terms of computing power was worth the resolution obtained, so the finest mesh, with around 6 million elements, was selected for future calculations (in terms of solution quantities, all meshes were below 1% absolute error compared to the 2-D cases and the finest mesh).

The mesh details can be appreciated in figures 4.26, 4.27 and 4.28.

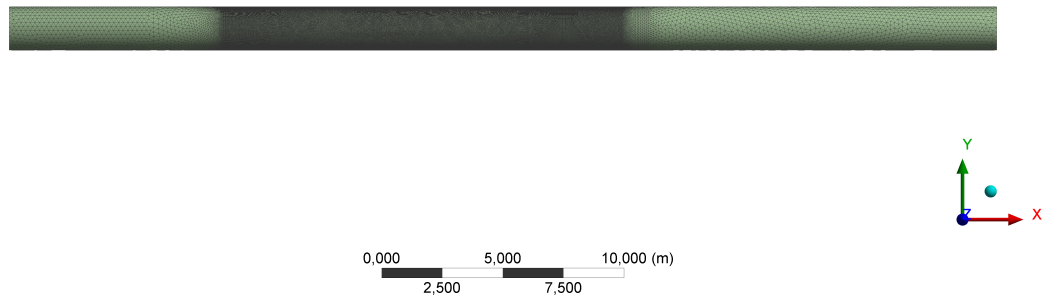


Figure 4.26: 2-D mesh: overall surface view.

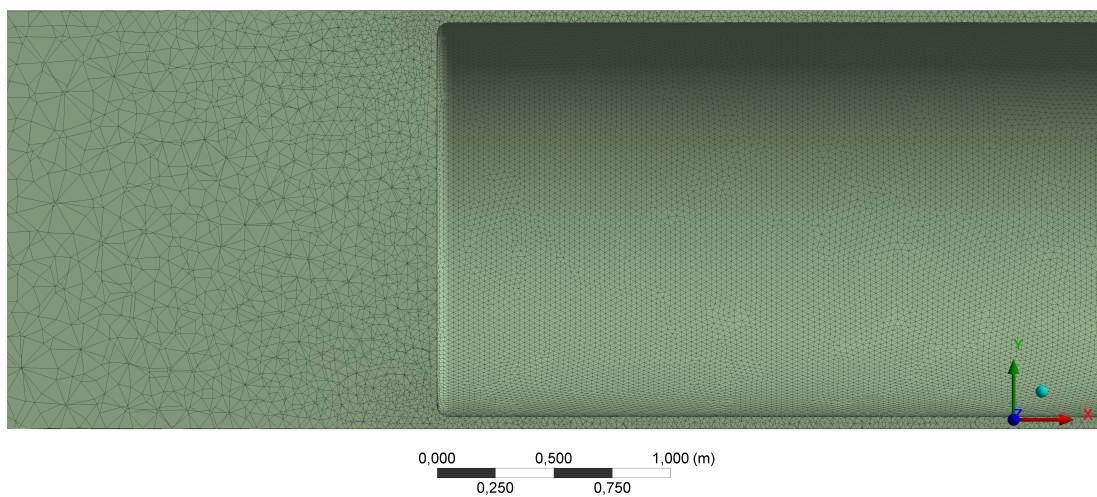


Figure 4.27: 3-D mesh: inlet detail at symmetry plane.

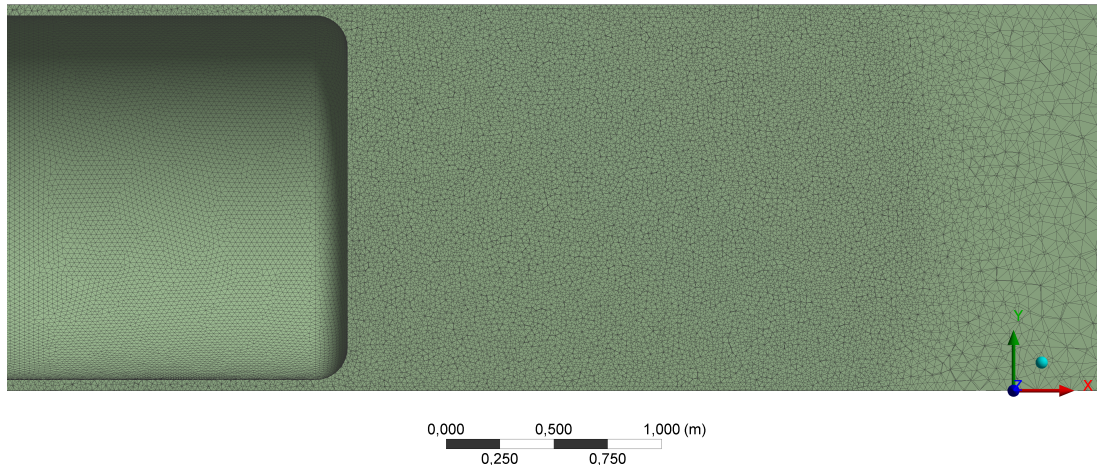


Figure 4.28: 3-D mesh: nozzle detail at symmetry plane.

FLUENT setup and boundary conditions

The 3-D calculation setup and final boundary conditions were almost identical to the 2-D case, the only difference is the non-axisymmetric formulation of the problem and solver and the definitions of the compressor and nozzle boundary conditions, which include the option for introducing a swirl movement to simulate the rotation of both machines and the aerodynamic interaction it can produce. As usual in this development, all this changes were made into parameters for further study.

4.2.3 CFD Cases

2-D Speed ramp-up

A Mach ramp was applied sequentially in order to simulate the pod's acceleration. As the Mach number was varied the mass flow rate entering the compressor, and thus exiting the nozzle, varied as well. In order to accommodate for this change the conditions in the nozzle were changed as seen in figure 4.29. This values were obtained iteratively in order to conserve mass flow through the pod's diffuser inlet and nozzle outlet.

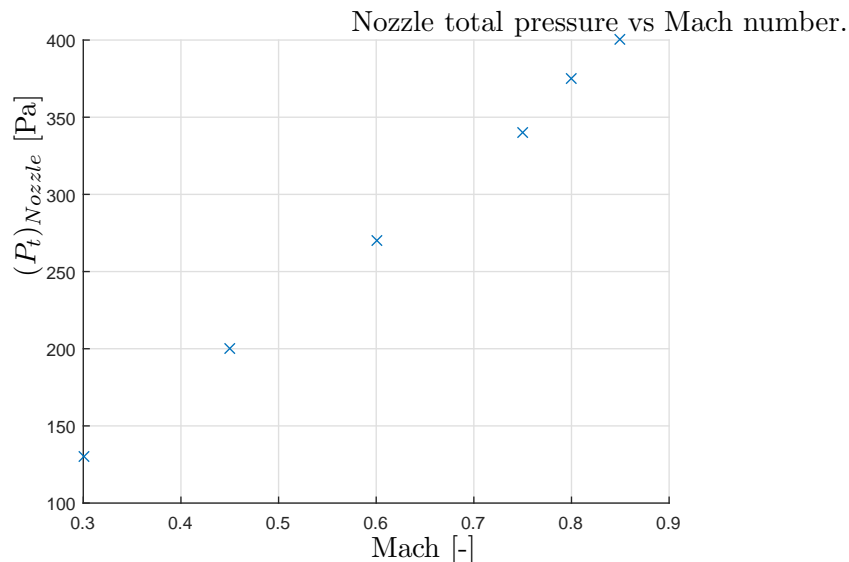


Figure 4.29: Nozzle total pressure as a function of Mach number for the ramp cases.

The results of this calculations are shown in the following figures.

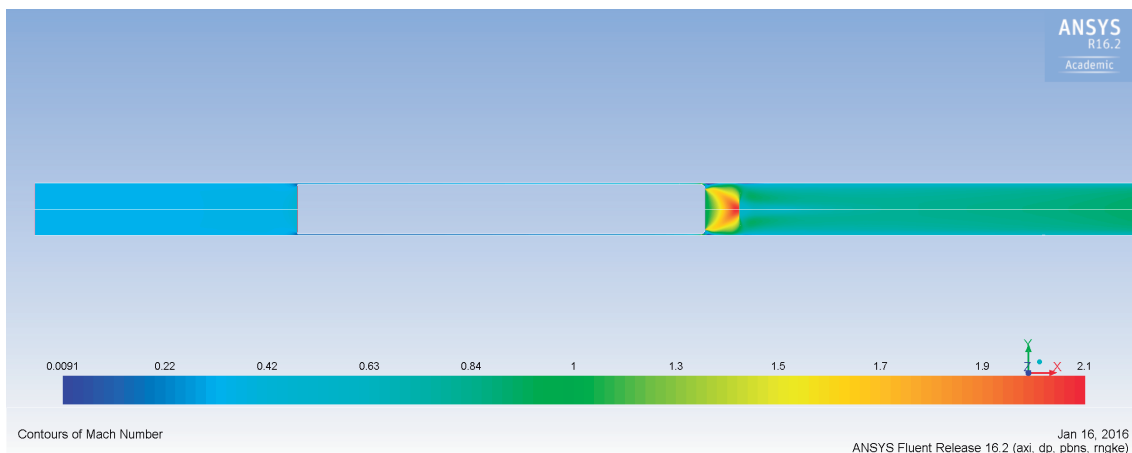


Figure 4.30: Mach contours at the nozzle area, Mach 0.3.

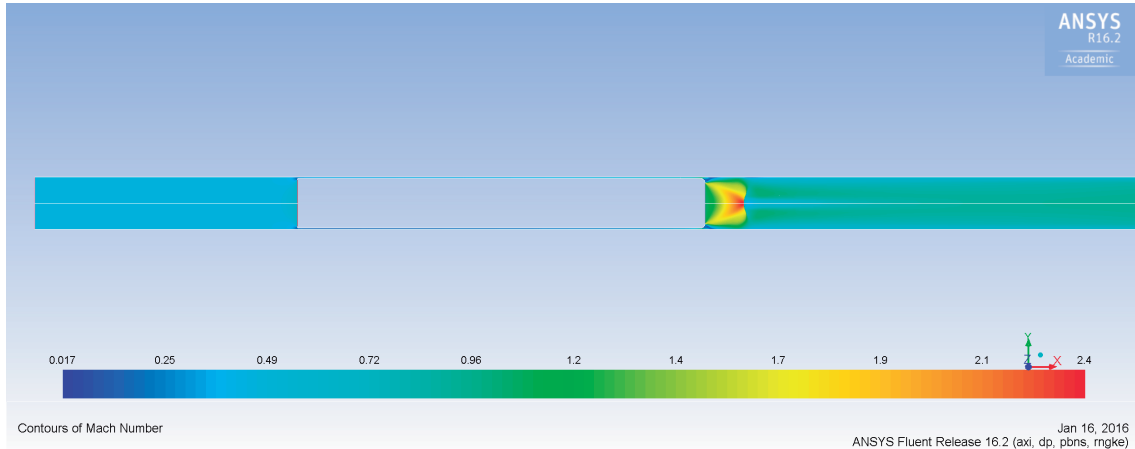


Figure 4.31: Mach contours at the nozzle area, Mach 0.45.

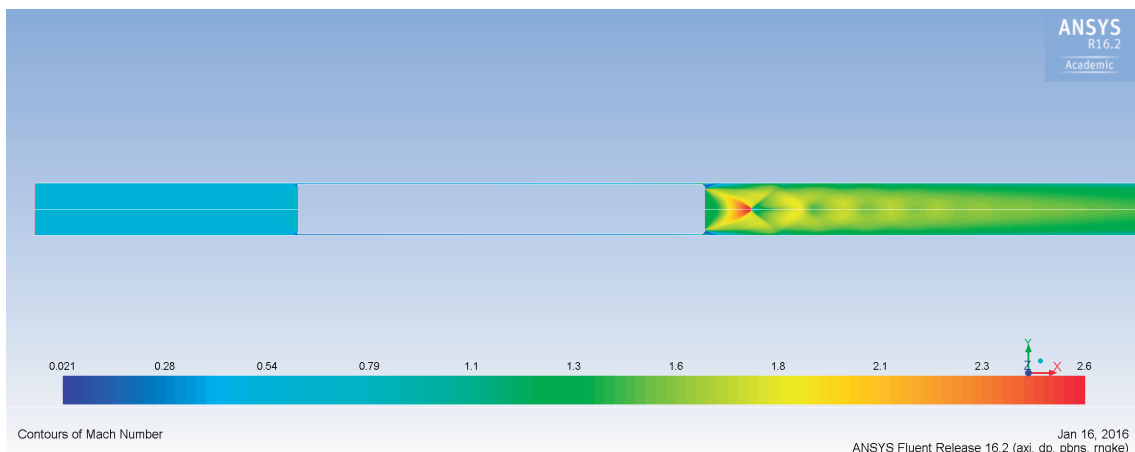


Figure 4.32: Mach contours at the nozzle area, Mach 0.6.

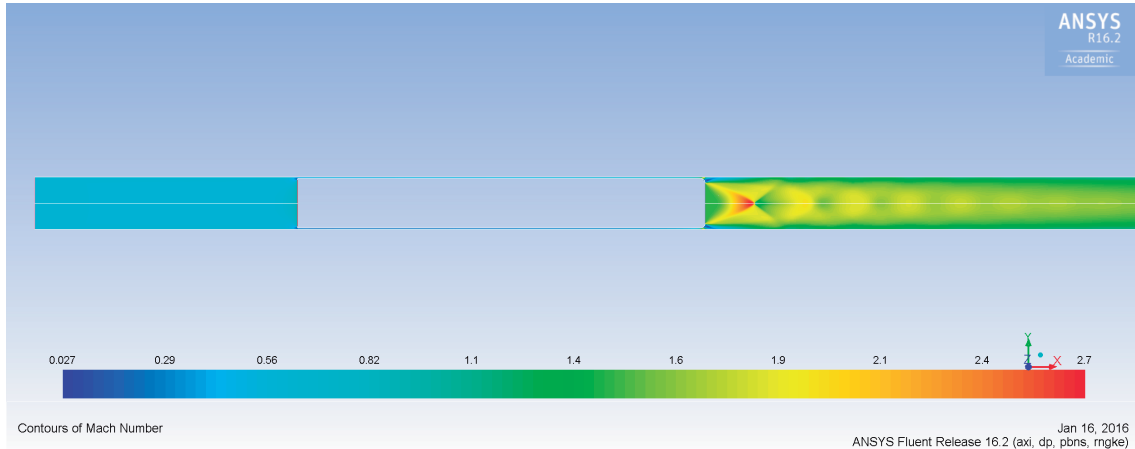


Figure 4.33: Mach contours at the nozzle area, Mach 0.75.

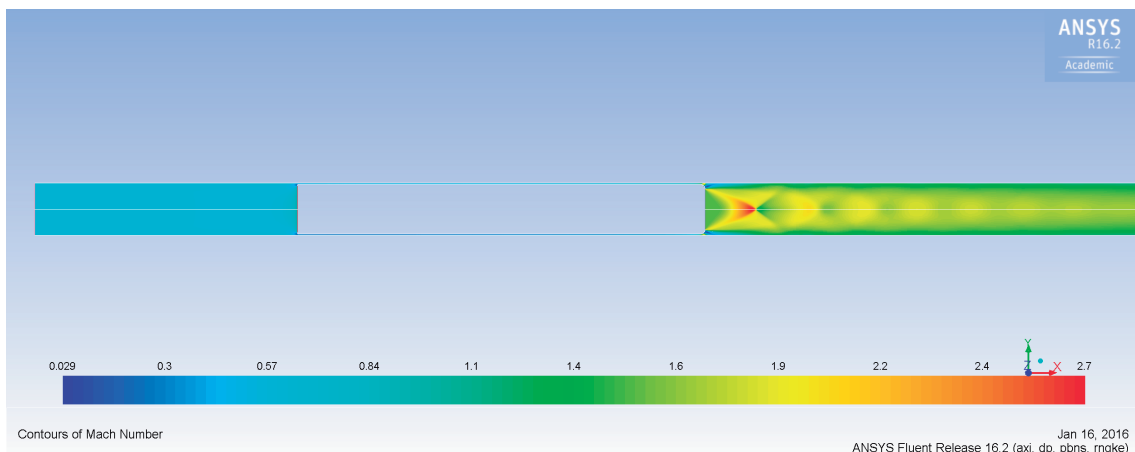


Figure 4.34: Mach contours at the nozzle area, Mach 0.8.

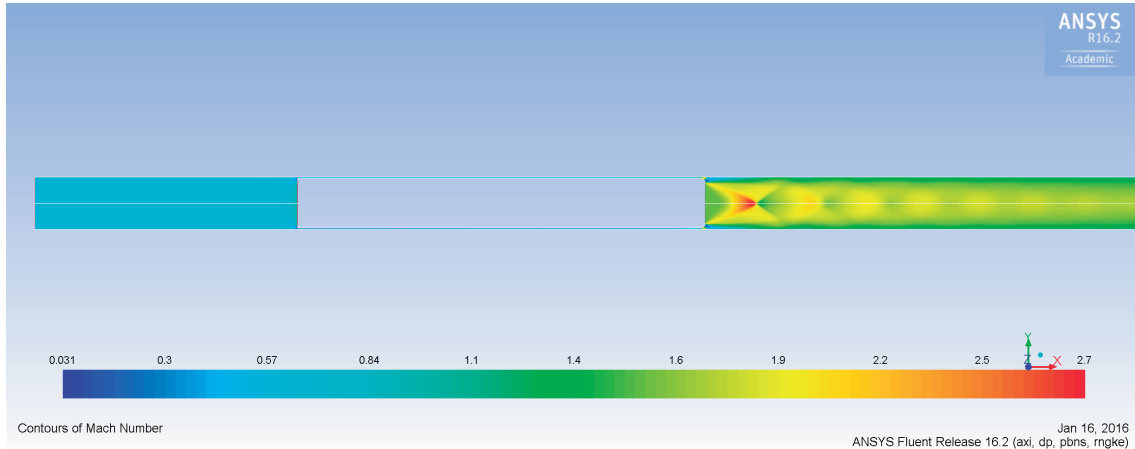


Figure 4.35: Mach contours at the nozzle area, Mach 0.85.

The flow patterns in the tube follow the classic results for a subsonic compressor intake for the aft of the pod. On the rear, the nozzle flow becomes dominant and solutions similar to rocket engine plumes and afterburner flows in jet engines appear as it was expected considering the imposed boundary conditions. As the conditions in the nozzle increase the flow needs to expand to adapt to the tube conditions and Mach disks and Mach diamonds show up in the calculations. As flow evolves, the patterns dissipate and becomes homogeneous. The contours of static pressure at the inlet, figure 4.36, show the depression imposed to the compressor inlet and the increase in gap static pressure due to stagnation effects as the gap flow is choked.

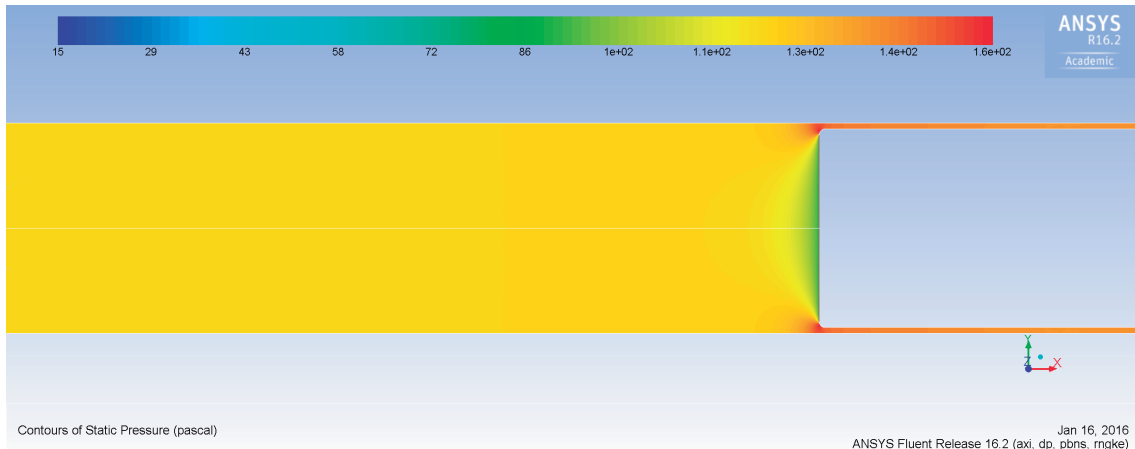


Figure 4.36: Static pressure contours, inlet area, Mach 0.75.

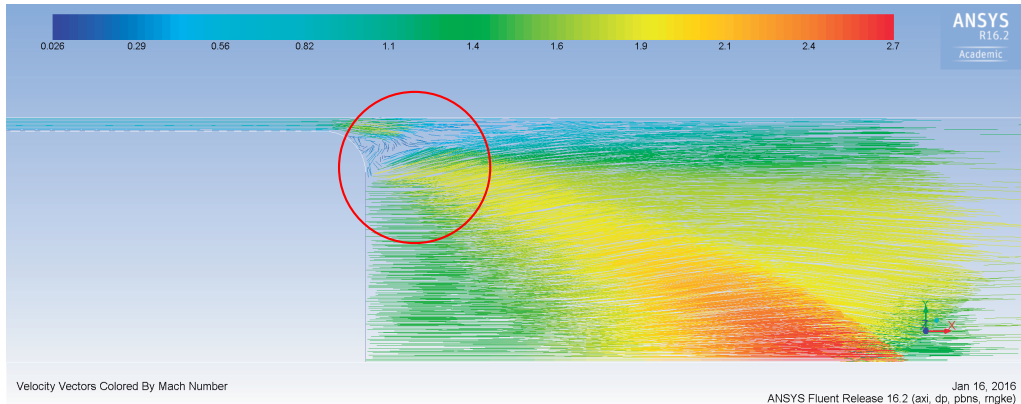


Figure 4.37: Gap velocity vectors, coloured by Mach number, Mach 0.75.

An interesting fact is the flow evolution at the gap exit, between the rear part of the pod and the tube and near the nozzle, showing the viscous mix layer and the acceleration over the Fanno flow. This flow is further observable by plotting flow conditions along the gap as shown in figure 4.38.

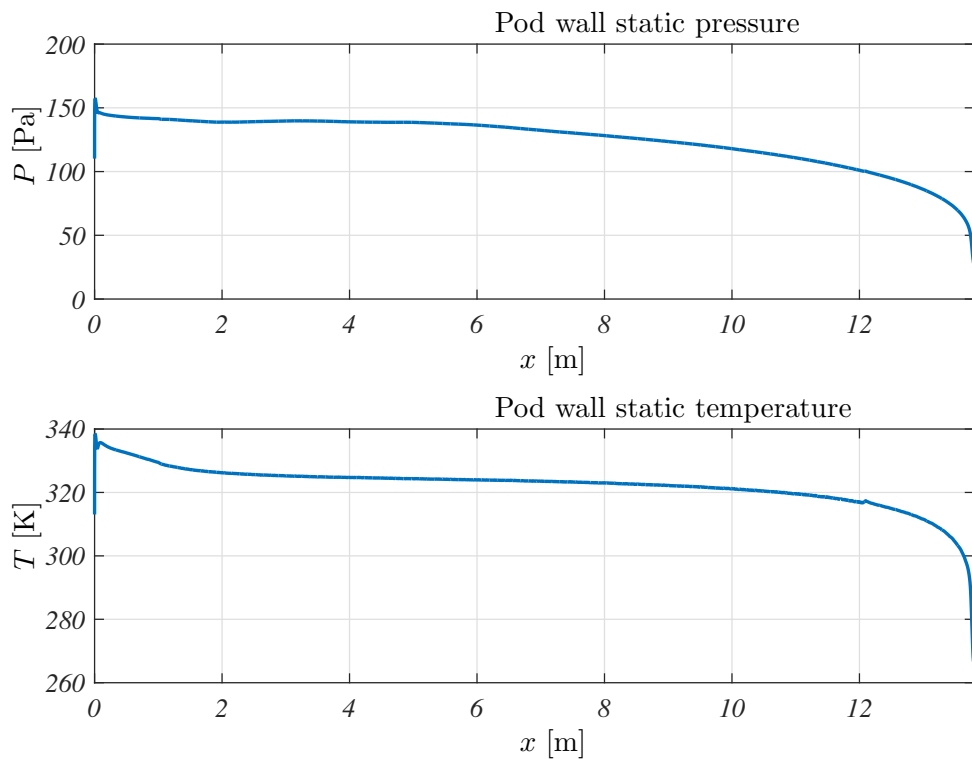


Figure 4.38: Fanno flow along the gap for Mach 0.75.

Finally, temperature and pressure contours show the predicted profile around the pod,

arriving to sonic conditions at the gap outlet ($x = 12.9$).

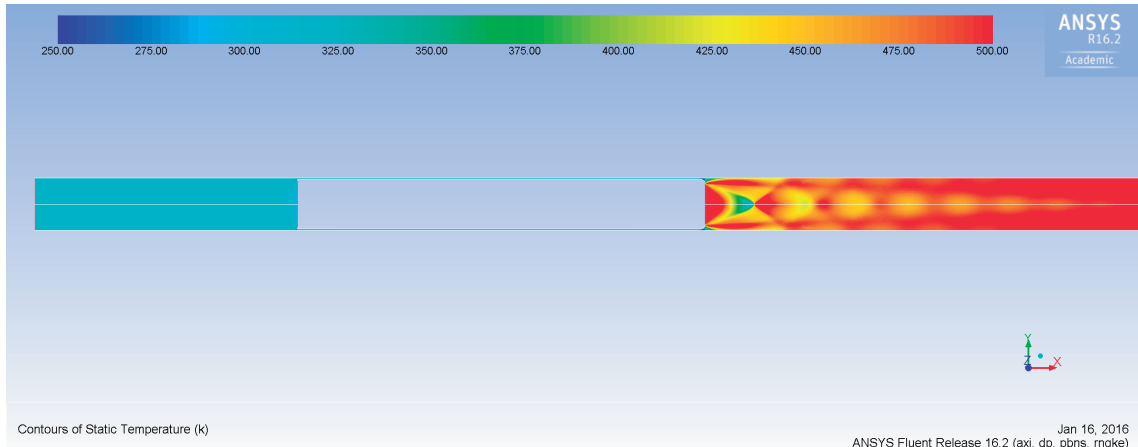


Figure 4.39: Temperature contours, Mach 0.75.



Figure 4.40: Temperature contours, pod detail, Mach 0.75.

3-D Cruise configuration

As the cruise speed corresponds to a Mach number around 0.75, this case was set up to mimic those conditions. Nozzle pressure was set up in the same way as the 2-D case.

The results of this case are shown in the following figures.

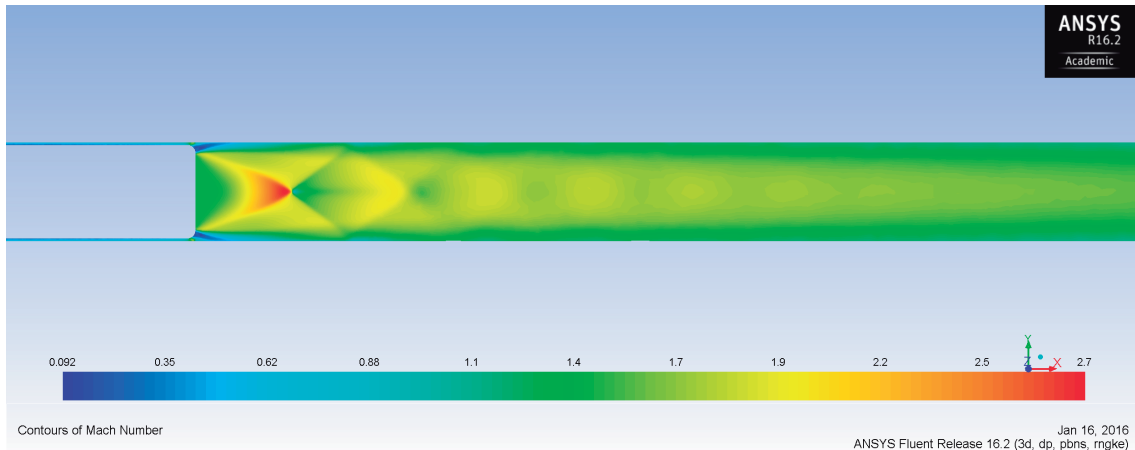


Figure 4.41: Shockwaves in the nozzle area displayed as density gradients and coloured by static pressure.

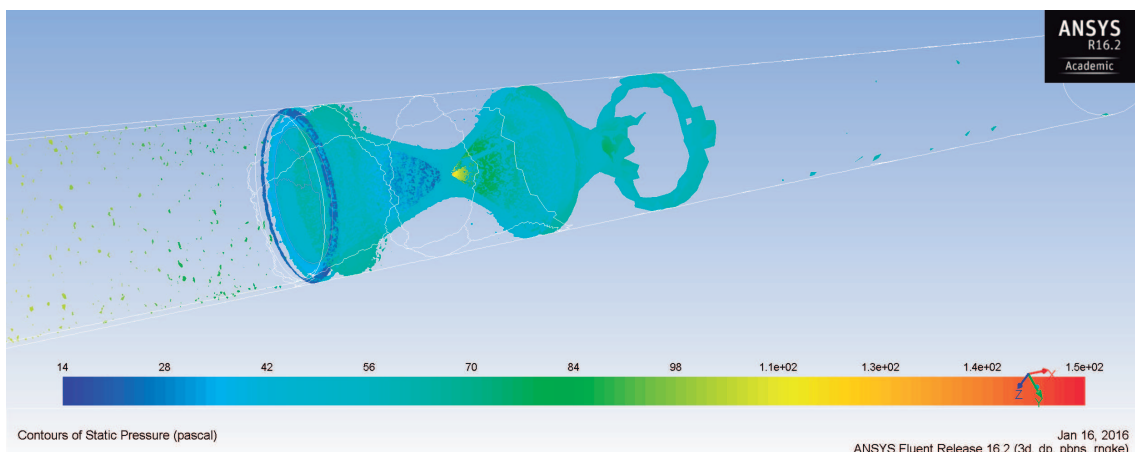


Figure 4.42: Shockwaves in the nozzle area contours of static pressure at pod symmetry plane.

Mach diamonds and shockwaves are identical to the 2-D case and air conditions around the pod have been pictured in figures 4.43, 4.44, 4.45 and 4.46. Values for the temperature around the pod suggest that no special materials are required for cruise phase. In addition, pressure fluctuations are small since the static tube pressure is also low. This fact allows for a simpler structure analysis from the tube point of view but rotating machinery inserts harmonic excitations into the structure which have to be evaluated. Moreover, the

sameness between the 2-D cases and the 3-D cases has validated the last to calculate the swirl effects due to turbomachinery flow.

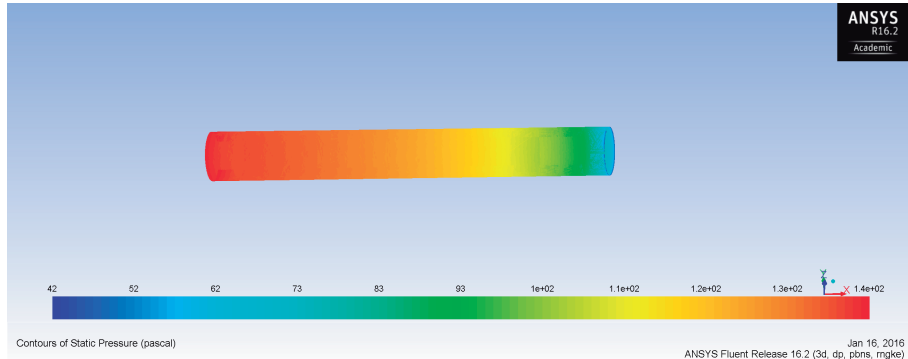


Figure 4.43: Contours of static pressure at pod wall.

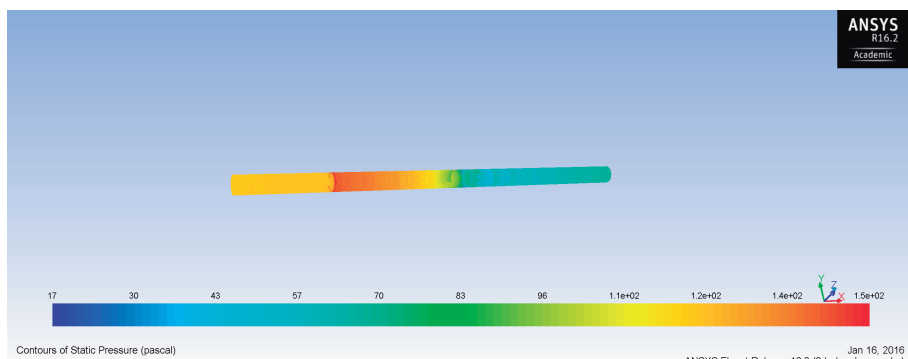


Figure 4.44: Contours of static pressure at tube wall.

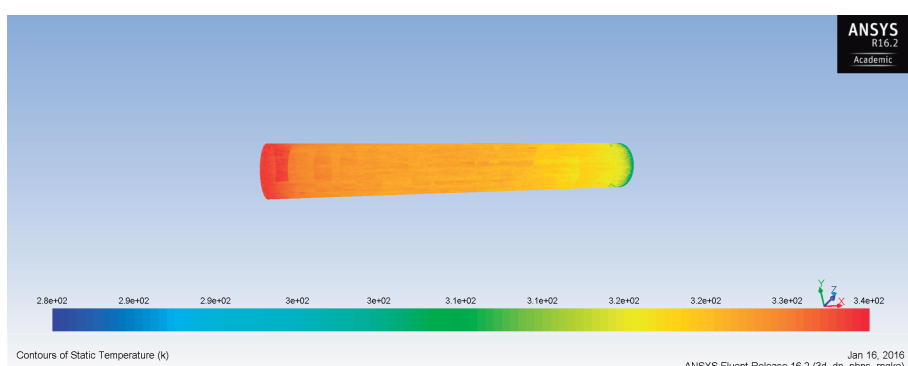


Figure 4.45: Contours of static temperature at pod wall.

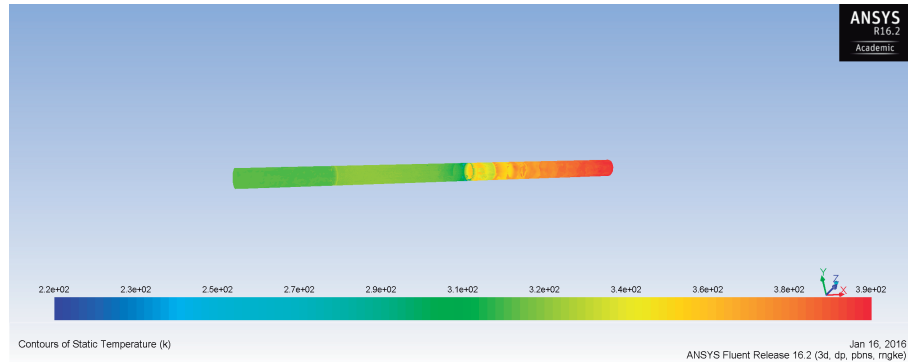


Figure 4.46: Contours of static temperature at tube wall.

As in the 2-D cases, gap Fanno flow is visible in the simulations. Pressure and temperature in the pod wall and tube wall are plotted along the travel direction for all mesh points. As it can be seen in the figure 4.48 the data is not widely spread at each position in the tube this means the solution is almost axisymmetric, and corresponds faithfully to 2-D calculations.

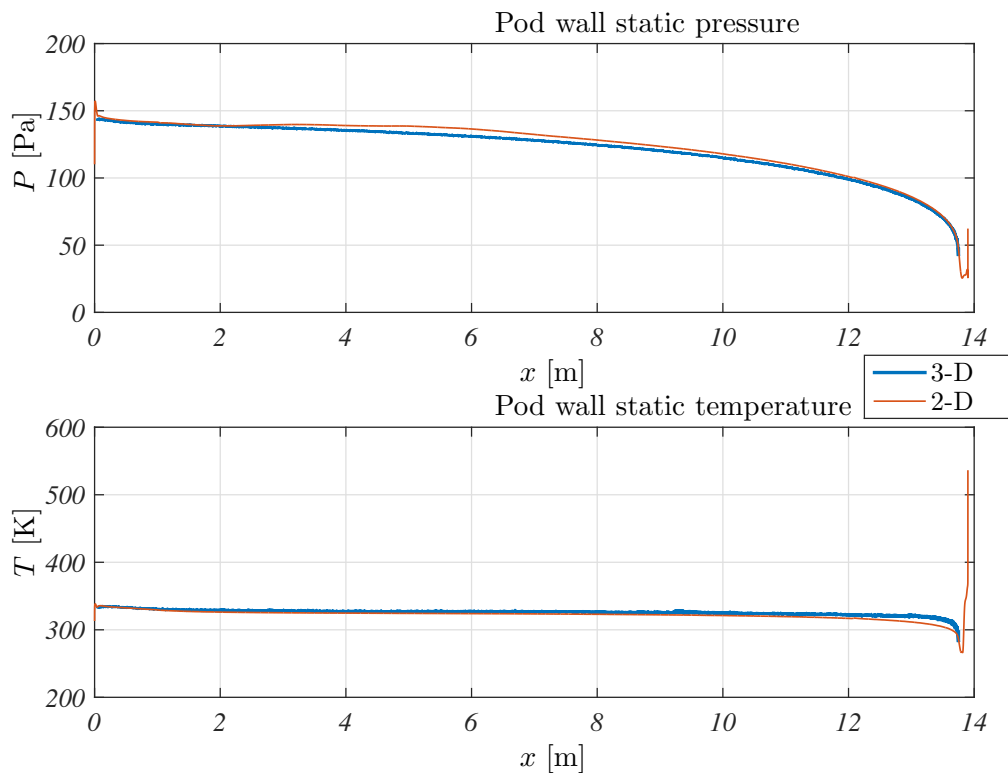


Figure 4.47: Temperature and pressure evolution on the pod wall for the cruise case.

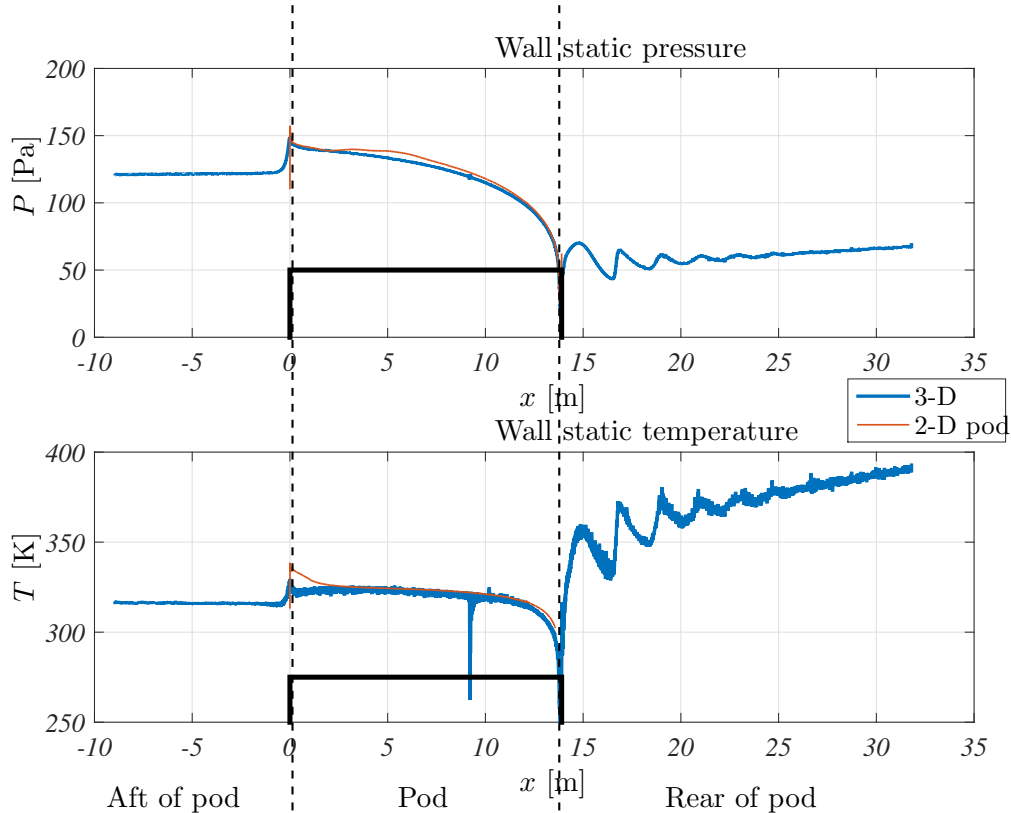


Figure 4.48: Temperature and pressure evolution on the tube wall for the cruise case.
In black is sketched the position of the pod.

4.2.4 Low speed propulsion system

The previously mentioned propulsion system based on pure aerodynamic propulsion, despite its ability to provide thrust at high speeds it lacks efficiency while working at low speed conditions. A complementary solution based on mechanical traction has been devised. This system will consist on several retractable wheel sets distributed beneath the pod. The systems will work as follows:

- When the pod is stopped, the levitation system is turned off and the pod is let to rest on the wheels.
- While accelerating at low speed the main propulsion will be provided by several sets of powered wheels moved by electric motors. This behavior will be maintained until the pod speed reaches a certain threshold.
- Once the pod is travelling fast enough the compressor will start moving and the main propulsion system will be activated. Simultaneously, the levitation system will be progressively turned on and the wheels will be retracted into the structure of the pod.

For the braking phase the described sequence will be played in reversed order.

In case of failure of either, aerodynamic propulsion or levitation systems, the wheels will be automatically extended and the pod will travel by rolling means.

4.3 Ergonomics, passenger comfort and design

After performing the previous calculations a concern was shown regarding the internal cabin space available for the passengers. It was decided to require a external product designer a study of the space available. Its conclusions were clear, with the tube diameter proposed at the Alpha report there is no meaningful room for passengers inside the pod. A decision was made in order to provide a comfort level adequate for the ride, tube diameter was increased and the cabin was stretched. This new configuration, despite the efforts, still does not provide enough room for a comfortable travel experience but is enough to a short trip. In figures 4.49 and 4.50 the cabin internal distribution is shown together with real sized dummies.

Also, to provide a wider cabin sensation, the space above the cabin was increased and the ride position was reclined, fact that allows higher G rates in a safer way. There is a relatively large area in between both rows of seats which could be arranged as a baggage compartment for the passengers.

As an example, the Cessna Citation XLS+ has a maximum cabin height of 1.73 m in the alley. This height barely enables passenger movement in flight. On an extreme case, the Cessna Citation Mustang has only a 1.37 m cabin height at the alley, meaning the passengers must lean while moving. It has been supposed that the Alpha proposal dimensions must have come from a study of this similar capacity aircraft.

For longer travel distances, an even wider proposal should be studied to avoid claustrophobic sensation in the cabin and the possibility of a small lavatory.



Figure 4.49: Cabin distribution proposal.

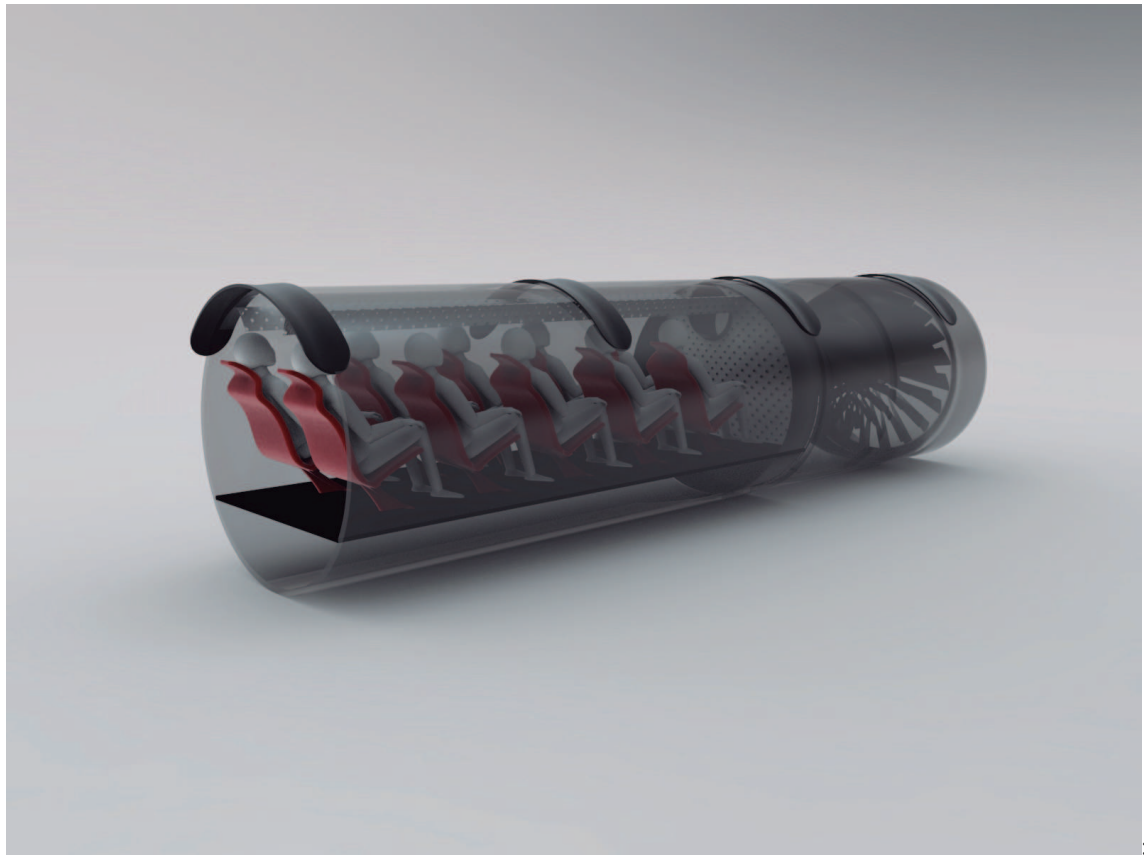


Figure 4.50: Cabin distribution proposal, perspective.

4.4 Design re-optimization

As has been described in section 4.3, the space available for the passengers is not a comfortable solution for the proposed tube diameter and cabin length. In order to fit the passengers comfortably in the cabin, the tube diameter and the pod length have been extended. Because of this fact, a new cruise optimization like the one described in 3.3.1 is needed.

Launching a new optimization calculation gives the results shown in figure 4.51.

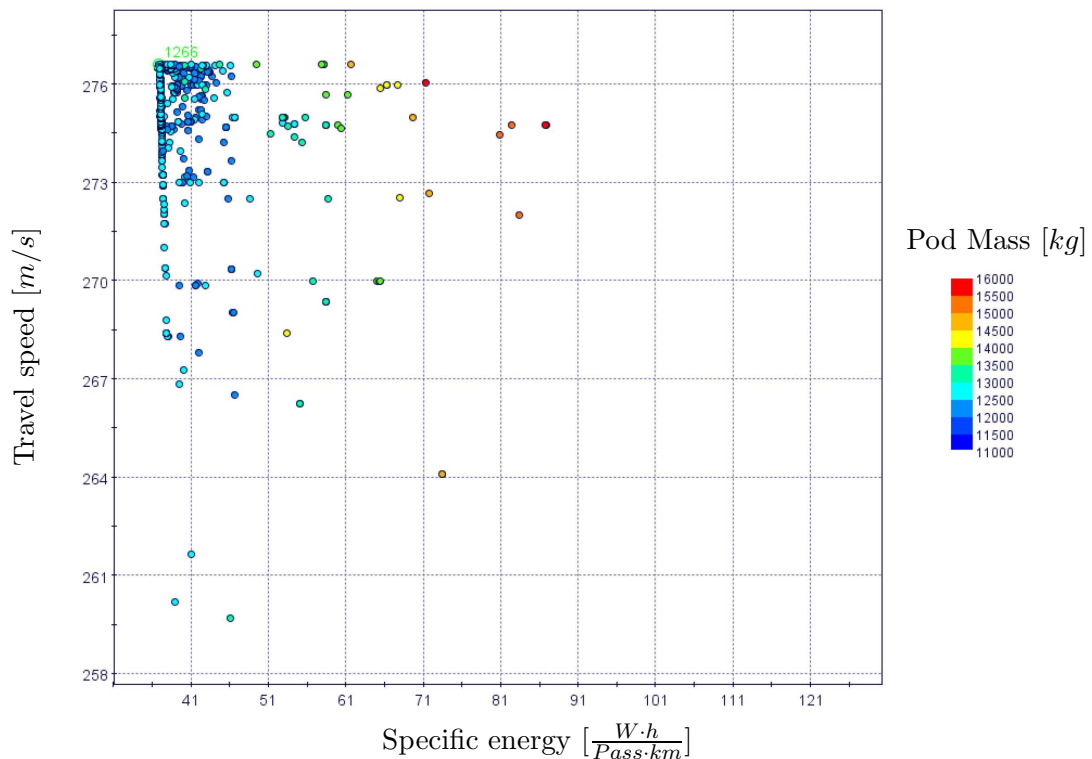


Figure 4.51: Cruise case optimization results.

The dimensions and variables of this run optimal result are shown in table 4.2.

Parameter	Value	Units	Parameter	Value	Units
Pod Length	19	m	Tube diameter	2.2	m
Gap distance	0.05	m	Tube pressure	100	Pa
Tube temperature	305	K	Travel speed	276	m/s
Diffuser suction	0.8	[\cdot]	Diffuser section ratio	1	[\cdot]
$(\pi_C)_{t/t}$	22	[\cdot]	$(\eta_C)_{t/t}$	0.7	[\cdot]
$u_{C_{Out}}$	306	m/s	f_{Duct}	0.01	[\cdot]
L_{Duct}	15	m	$(\pi_T)_{t/t}$	15	[\cdot]
$(\eta_T)_{t/t}$	0.7	[\cdot]	$u_{T_{Out}}$	423	m/s
f_{Gap}	0.02	[\cdot]	Travel length	600	km
Pod mass	12236.5	kg	Specific energy	36.91	$\frac{W \cdot h}{km \cdot pass}$

Table 4.2: Design dimensions and parameters

If this results are analysed carefully it, can be seen that the flow regime and relevant non-dimensional groups remain fairly constant. The main source of discomfort is the increase in travel speed and the high compressor suction value which could lead to sonic conditions at diffuser inlet. From now on, it is assumed that the flow conditions for this configuration are almost identical to the described in 4.2. Regarding the magnetic levitation system, as it is fairly decoupled of geometric parameters, the values calculated before can apply without incurring large errors.

4.5 Structural analysis

The case studied for this development is the passenger cabin as a critical component for the safety of Hyperloop operation. As the pod acceleration and deceleration values should be nominally low, the required initial acceleration and nominal deceleration cases are not relevant for this development.

Geometry

The cabin geometry is directly influenced by its internal surroundings: the air tube travelling from the compressor to the turbine and the exchangeable battery located directly below it. A straight plane floor was required for the cabin, and an upper space was reserved outside of the pressure vessel for the air tube as can be seen in figure 4.52 a). The endcaps of the pressure vessel were modelled as smooth continuous surfaces extending from the base geometry. It should be built of a composite material to minimise the weight and improve dynamic behavior. So, the choice material for this calculations was carbon fiber preps with a yield stress of 230 MPa [5]. The imposed charge is a outward pressure of 101225 Pa which corresponds to the difference between atmospheric cabin pressure and tube static pressure. First studies showed the need for additional reinforcement, so, a semimonocoque construction, with outer reinforcement formers and stringers was devised as is shown in figure 4.52 c) and d).

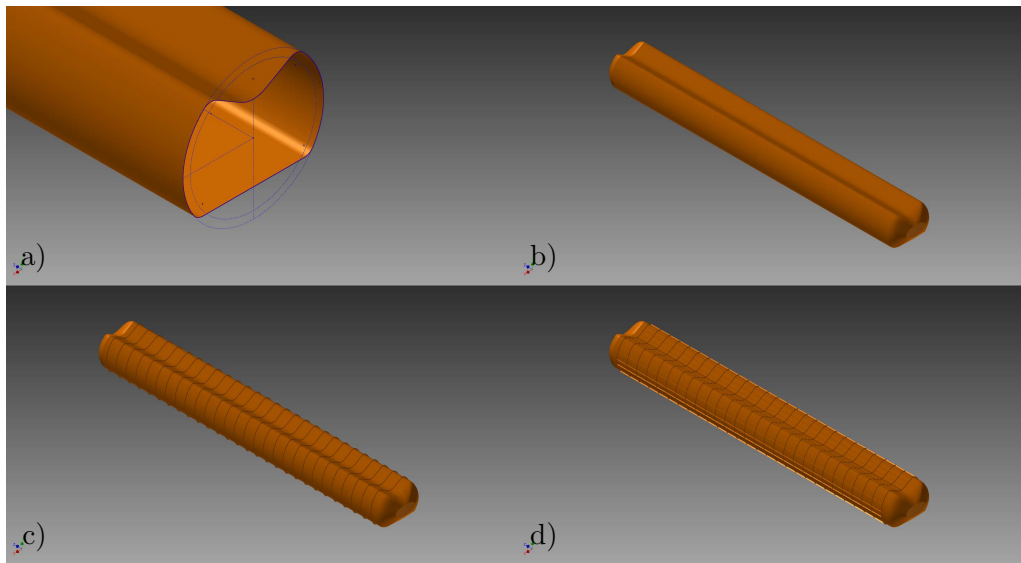


Figure 4.52: Pressure cabin geometry details.

4.5.1 Static analysis

Thickness parametric study

A first approach in order to minimise structural weight consisted in a parametric study of skin thickness as it represents the bulk of the cabin weight. The analysis was set up in ANSYS Mechanical and its results can be seen in figures 4.53 and 4.54. The main criteria for choosing a thickness is the maximum principal stress of the structure. As a safe choice, a thickness of 5 mm was selected and it is further analysed in 4.5.1.

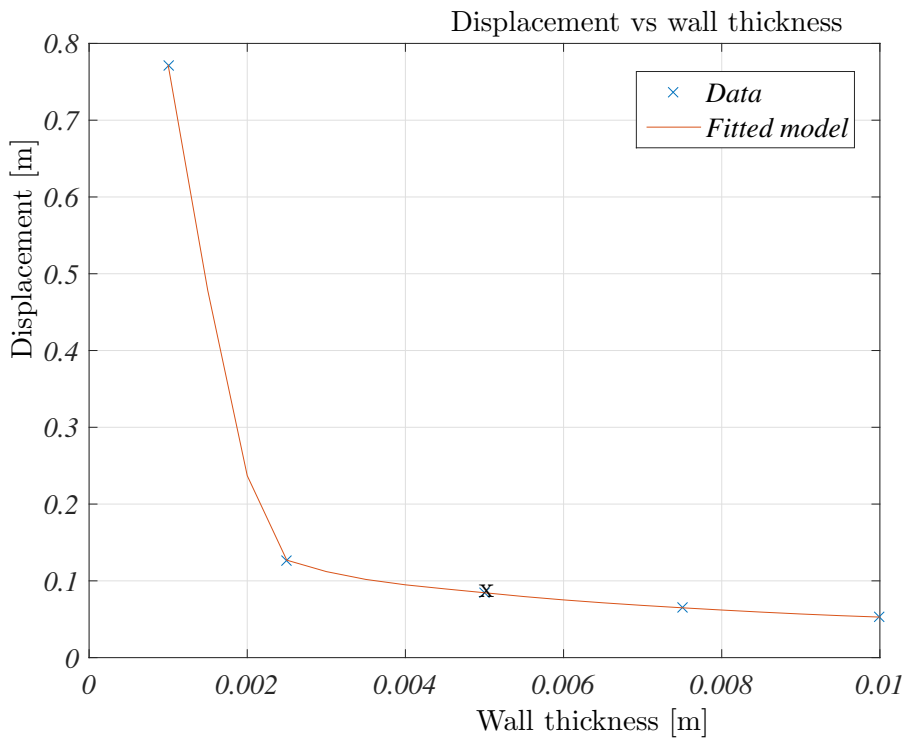


Figure 4.53: Cabin skin thickness displacement parametric study.

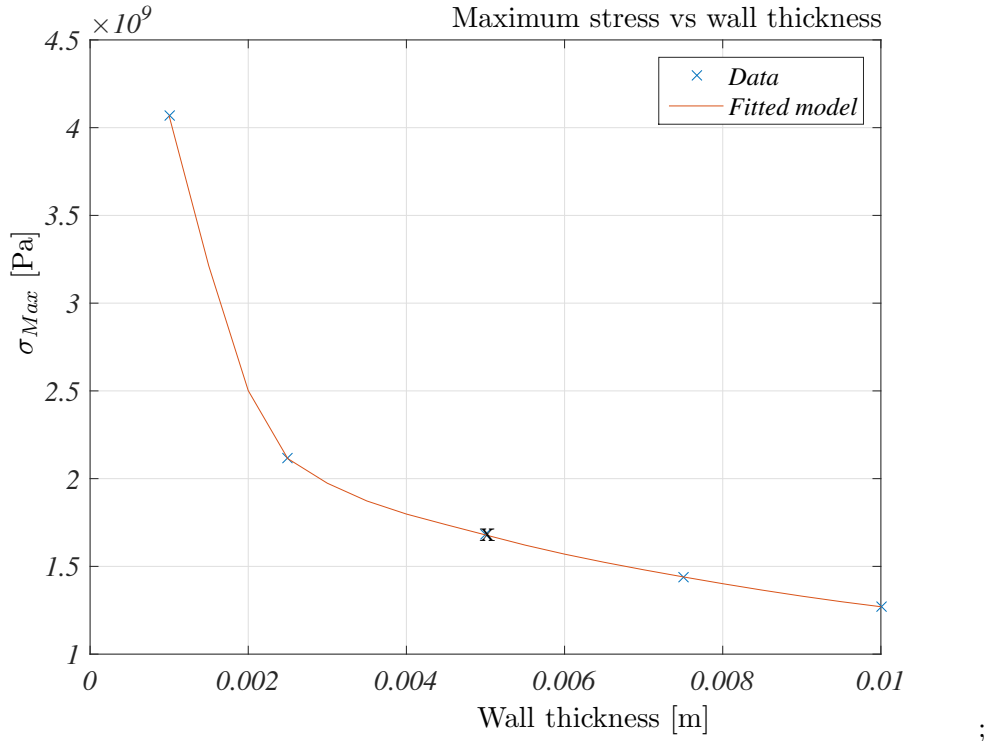


Figure 4.54: Cabin skin thickness stress parametric study.

Reference study

The mesh used in the calculations is showed in the following pictures. The software automatically detects if the mesh needs to be refined according to the case results, the showed mesh is the definitive one that was generated.

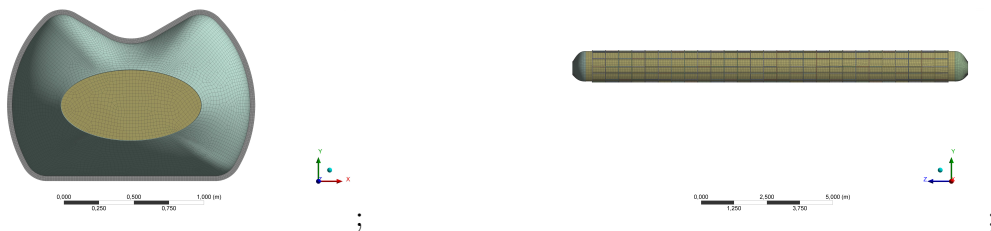


Figure 4.55: Cabin mesh: front and side view.

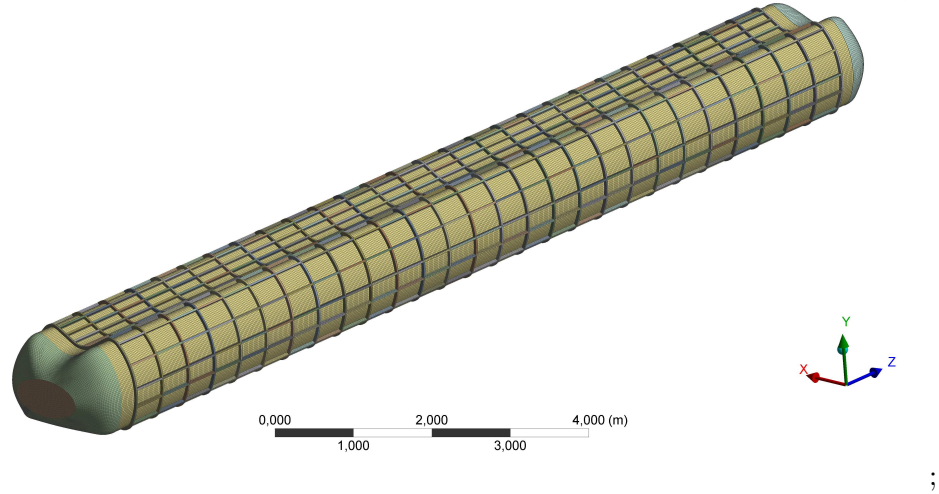


Figure 4.56: Cabin mesh: perspective view.

The results of the calculation for the chosen thickness of 5 mm for the structure are visible in figures 4.57, 4.58, 4.59 and 4.60. Maximum deformation is 0.086 m at the marked spot and maximum stress is 170 MPa.

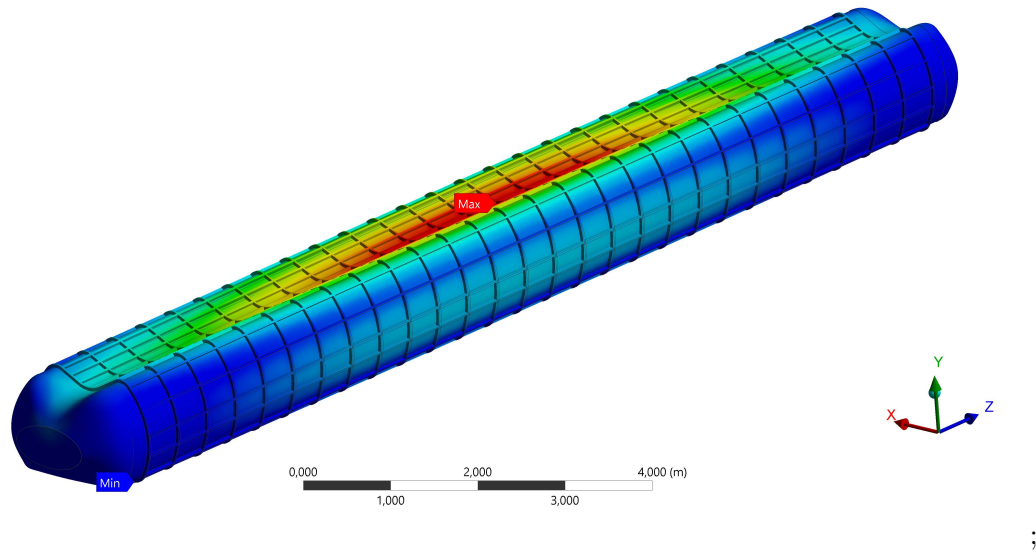


Figure 4.57: Cabin deformation: perspective view.

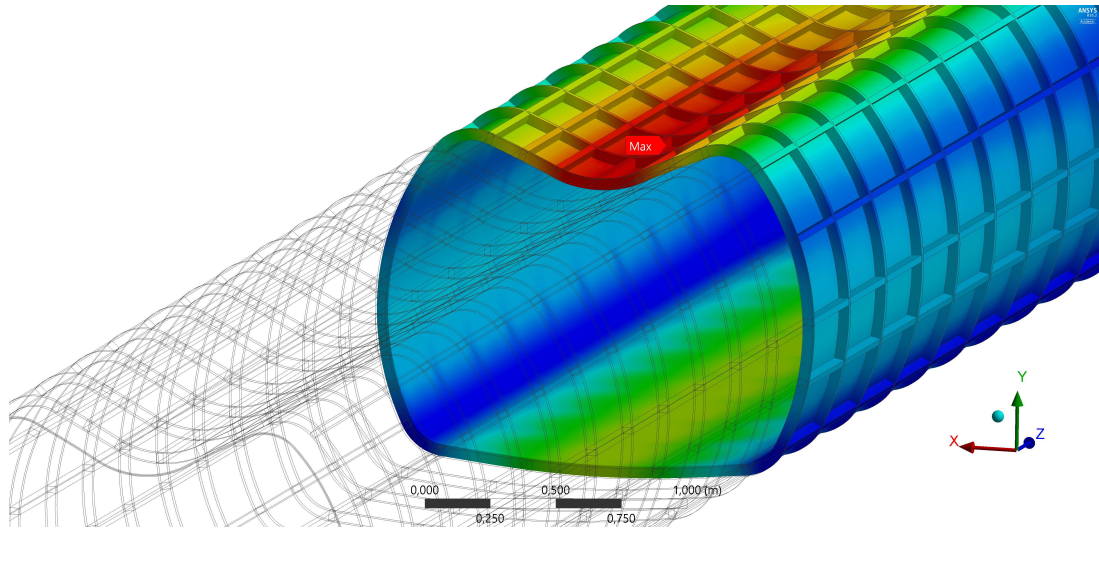


Figure 4.58: Cabin deformation: perspective cut.

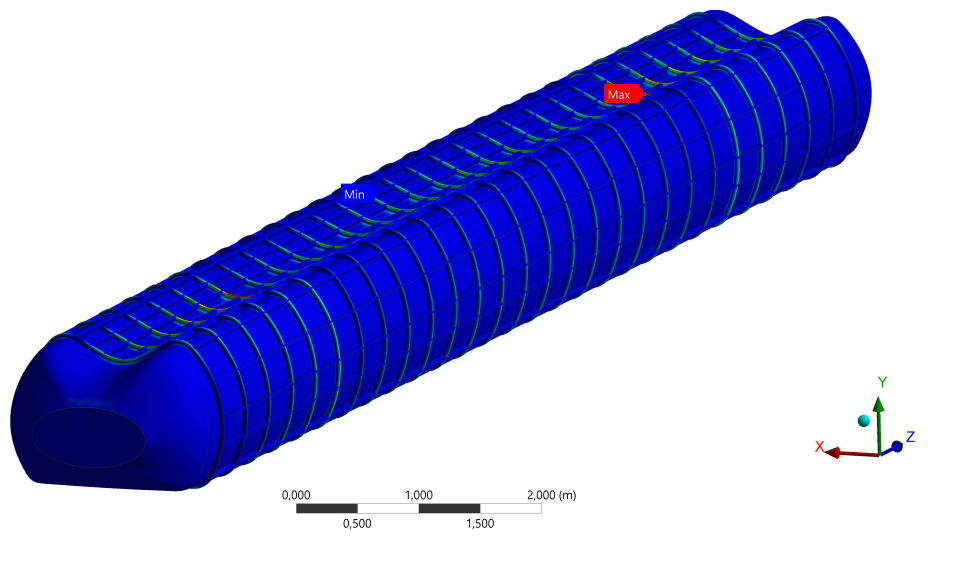


Figure 4.59: Cabin stress: perspective view.

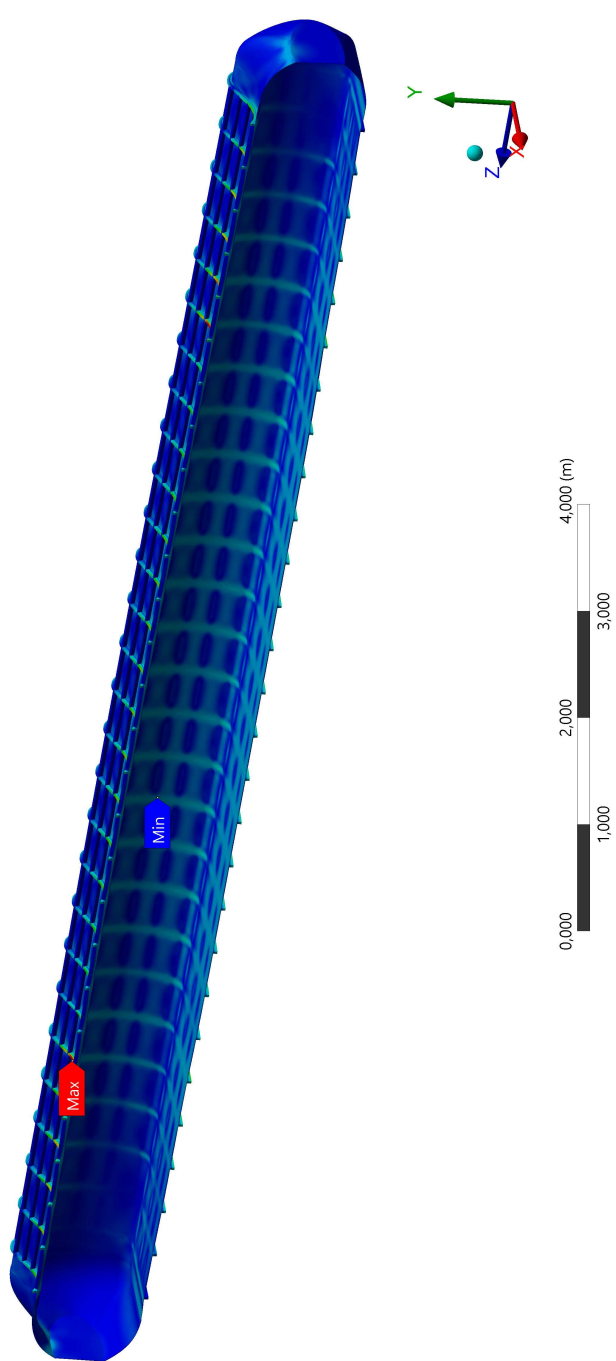


Figure 4.60: Cabin stress: perspective cut.

4.5.2 Modal analysis

Using the reference case results as a base, a modal analysis was performed with the aid of ANSYS Mechanical. There was no information available about structure damping so a non-damped analysis was performed. The first 10 global vibration mode frequencies can be seen in figure 4.61.

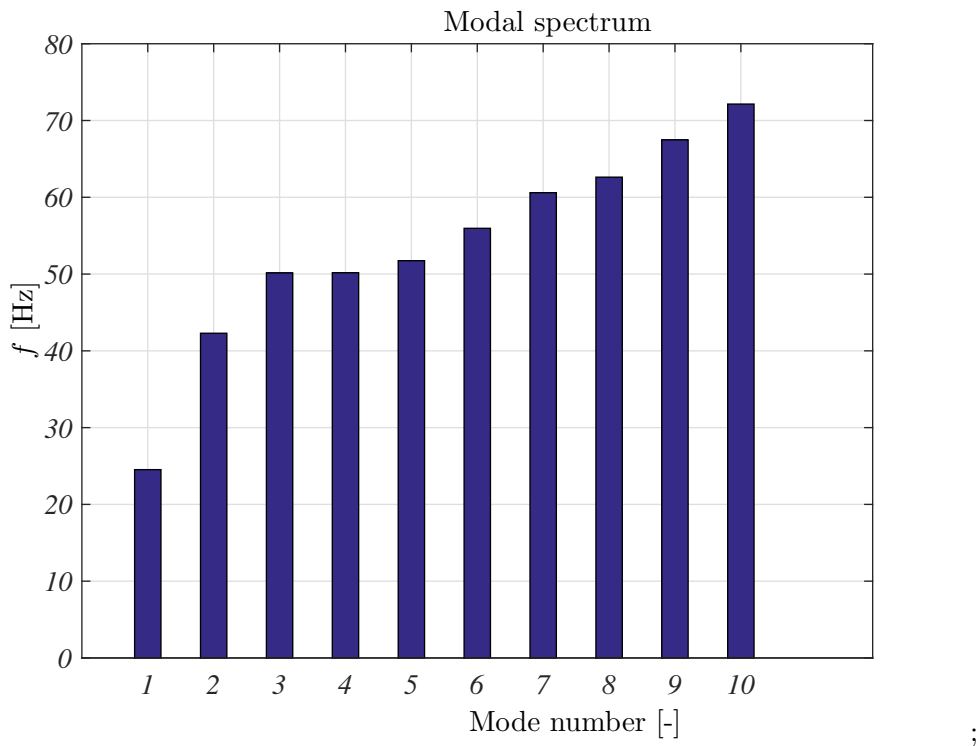


Figure 4.61: Cabin structure modal spectrum.

In addition, snapshots of the first five modes are shown in figures 4.62, 4.63, 4.64, 4.65 and 4.66. It can be seen that the first, second and third mode correspond to the harmonics of the top surface bending state. The fourth mode is a torsional situation and the fifth mode is a twin crest mode on the bottom plate of the cabin.

It is interesting to remark, that the frequencies of the moving and rotating elements of the pod, mainly turbine and compressor, should not couple with the ones of the cabin structure or to the ones of other pod structures.

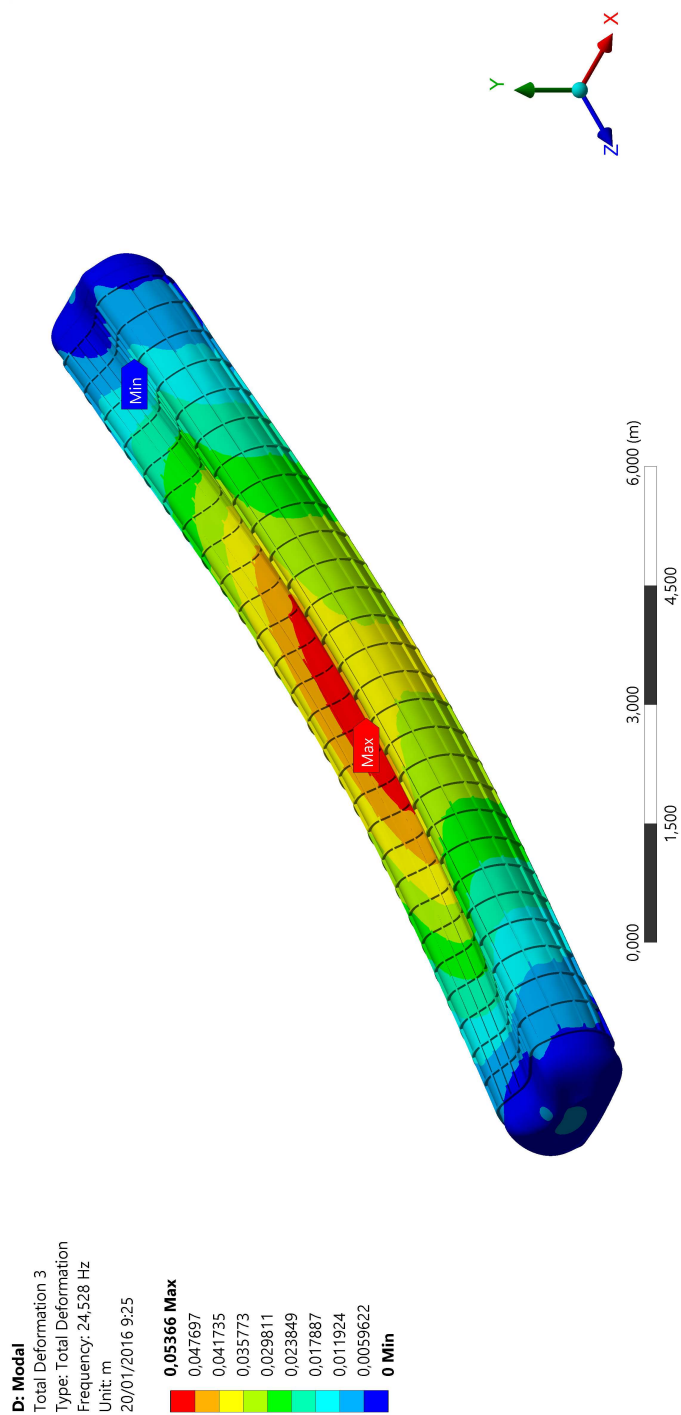


Figure 4.62: First vibration mode of the cabin structure.

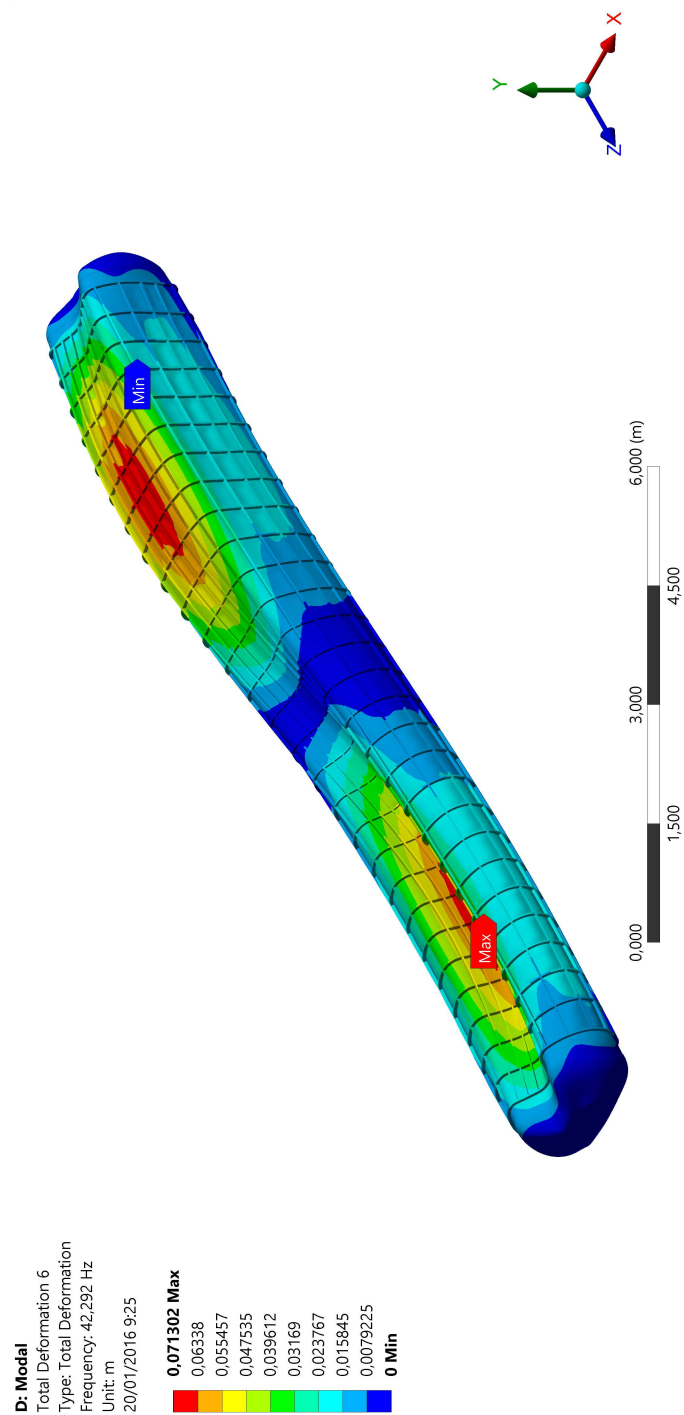


Figure 4.63: Second vibration mode of the cabin structure.

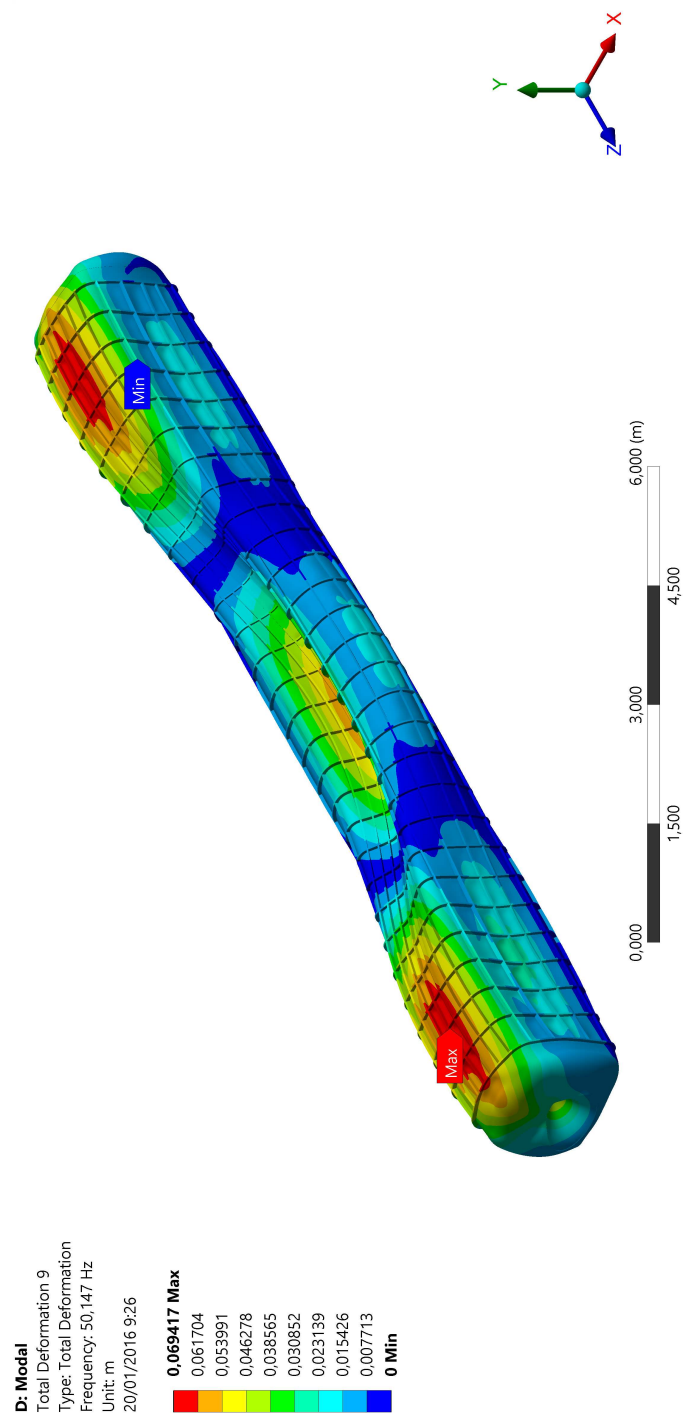


Figure 4.64: Third vibration mode of the cabin structure.

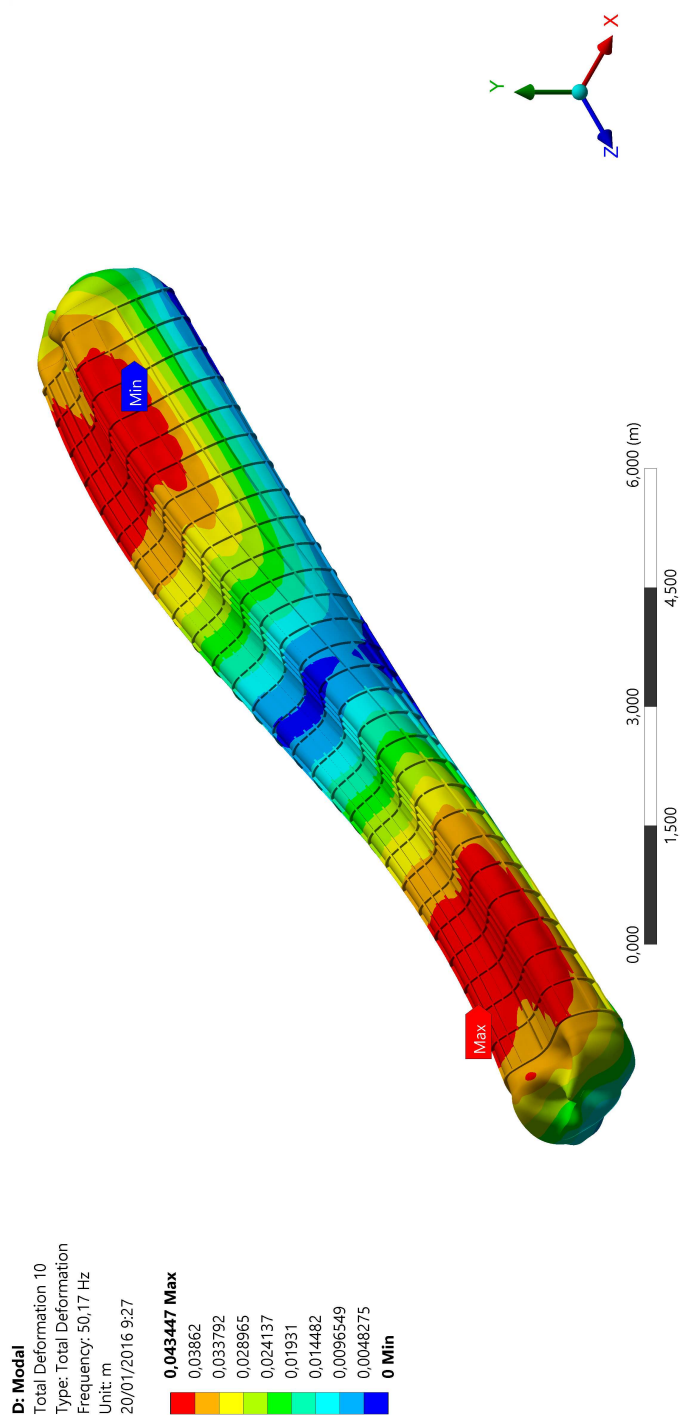


Figure 4.65: Fourth vibration mode of the cabin structure.

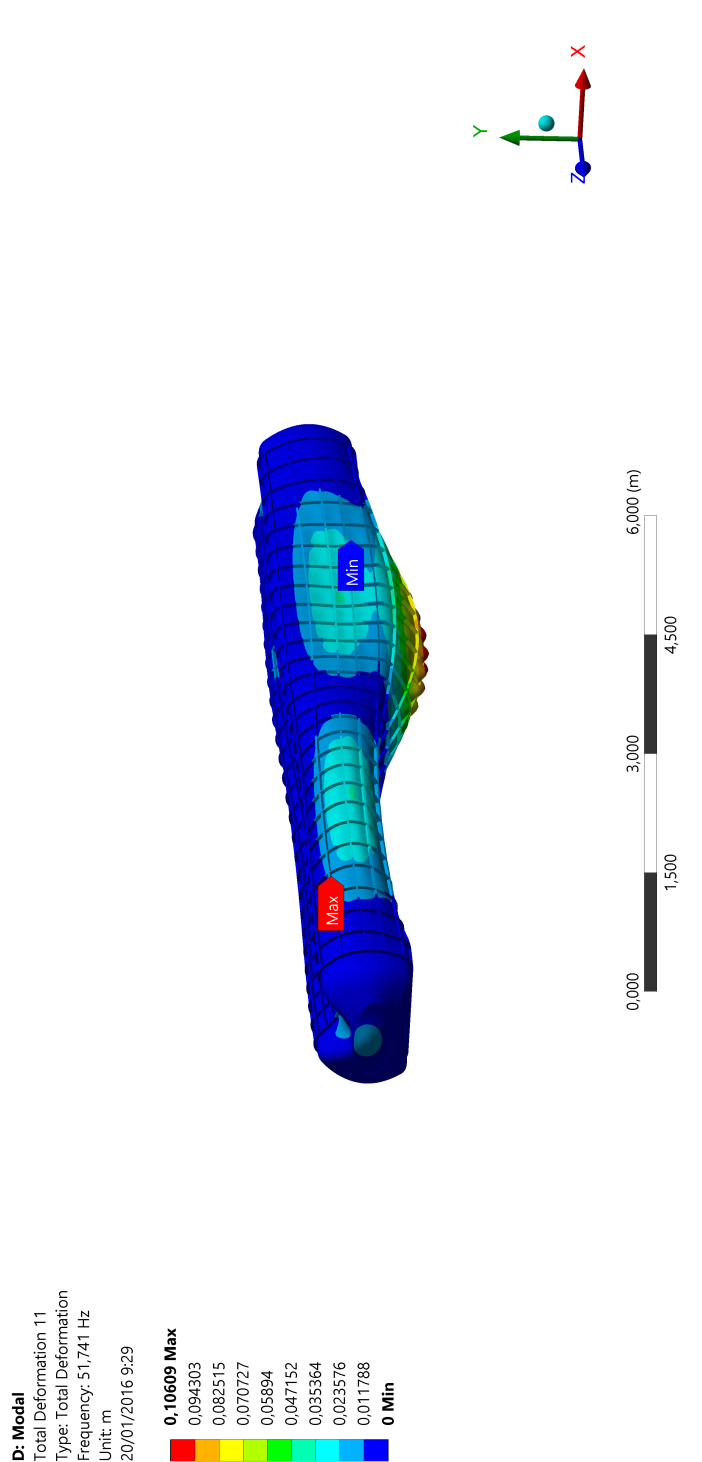


Figure 4.66: Fifth vibration mode of the cabin structure.

4.6 Braking system

From the section 4.2 an important fact was identified: despite the low pressure, the incoming air can brake the pod. This fact allows for the development of an efficient, simple and reliable braking system. This system consists of a valve at the compressor discharge tube. This valve allows, when open, to the air to flow to the rear part of the pod and feed either the turbine or the nozzle. When closed, the air cannot flow around the pod because of Fanno choking (see figure 4.38). Air incoming must pressurize in order to accomplish mass conservation, this increase in pressure exerts a force which can effectively stop the pod. Albeit of the mentioned valve, air flow can be restricted by changing the compressor's operating point, i.e., reducing the electric motor power or speed. The flow behavior in this regime is fairly complex and must be experimentally confirmed. In figure 4.67 the relevant steps in the flow development are depicted. It is known to happen that:

1. Just after closing the compressor discharge valve, a shock wave forms upstream the pod intake ($t = 0\text{ s}$ in figure 4.67).
2. This shockwave starts travelling upstream at a speed based on the flow conditions in the pressurized area ($t = 0.3\text{ s}$ in figure 4.67).
3. As the flow zone displaced by the pod movement is increasing, Fanno flow effects begin to appear and pressure and temperature keep increasing at the pod's inlet. In this state, the flow near the shock wave becomes choked ($t = 0.46\text{ s}$ in figure 4.67).
4. Due to Fanno flow choking, other shock wave is emitted from the pod's front and begins travelling upwards faster than the previous due to temperature increase in the pod region ($t = 0.67\text{ s}$ in figure 4.67).
5. When the second shock wave reaches the first, it dissipates and a new Fanno flow starts developing, which will lead to more repeating shock waves ($t = 1.8\text{ s}$ in figure 4.67).

The steps described in points 4 and 5 repeat, producing a high pressure zone before the pod and thus, braking it, as can be seen in the figure 4.67. When both effects evolve, the pressure increase and the pod deceleration compensated. Also, a secondary flow can escape this high pressure zone via the gap between the pod and the tube, but since the mass flow is negligible compared against the shear volume of air the pod is moving, this effect is not important.

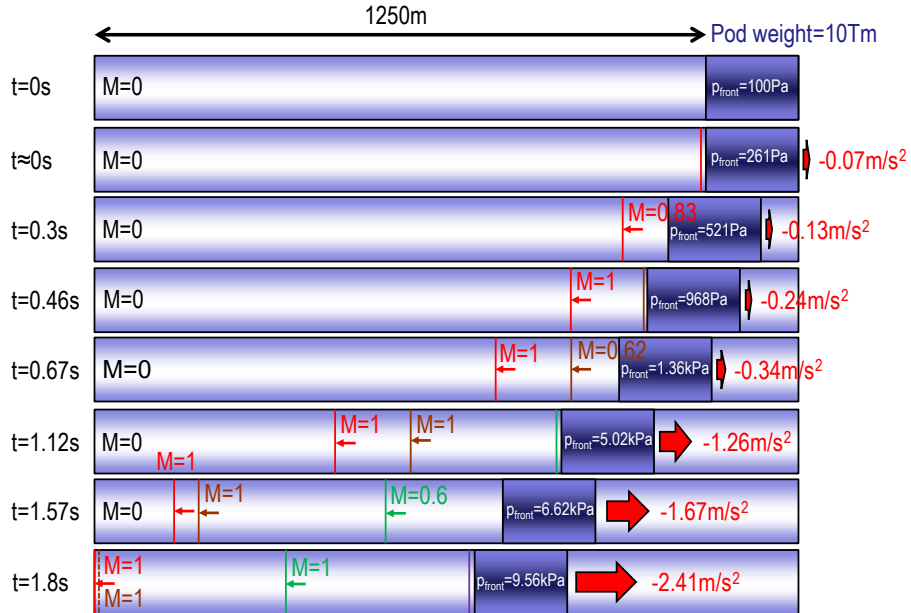


Figure 4.67: Pod braking flow patterns.

This is a transient effect, and, eventually, the pod will brake to a stop. The evolution of the described flow pressure has been partially calculated considering the evolution of consecutive normal shock waves and Fanno flows in front of the pod and its results are included in figure 4.68. When the travel speed is low enough, the wheels of the pod can be extended and used as a conventional regenerative braking system, providing extra energy budget in case of an emergency.

The process can be actively controlled by means of partially restricting the compressor flow and/or controlling the effective gap distance by means of variable geometry devices placed on pod surface.

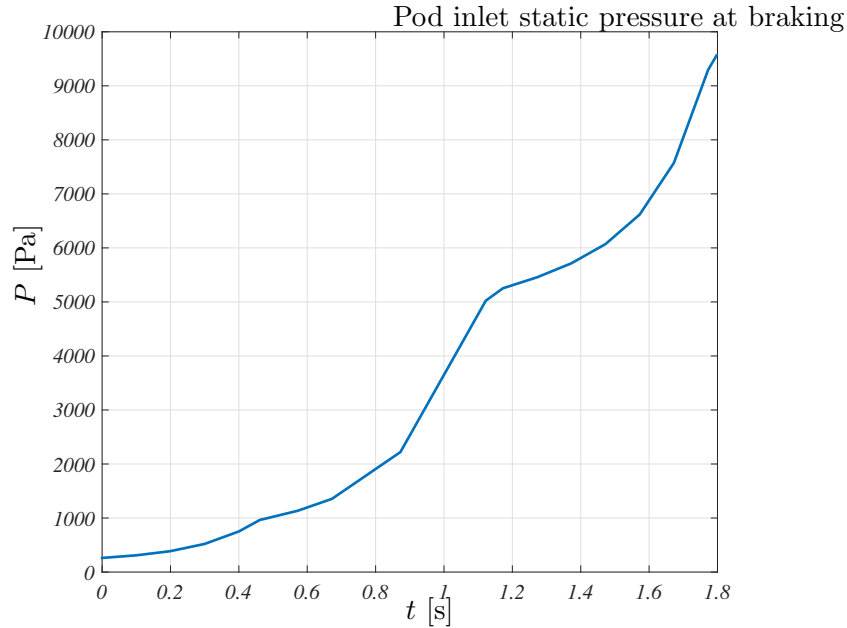


Figure 4.68: Pod inlet static pressure at braking.

Note that the pressure value increases by 2 orders of magnitude in a time of just 2 seconds, this fact permits an emergency braking safely if high pod accelerations can be tolerated.

Additionally, this behaviour has been partially simulated using CFD analysis. In the first place, the flow was simulated using the mesh from the previous 2-D calculations (see section 4.2). The result from the cruise 2-D condition was used as a starting point for a transient flow simulation. The results for three different timesteps are showed in figure 4.69.

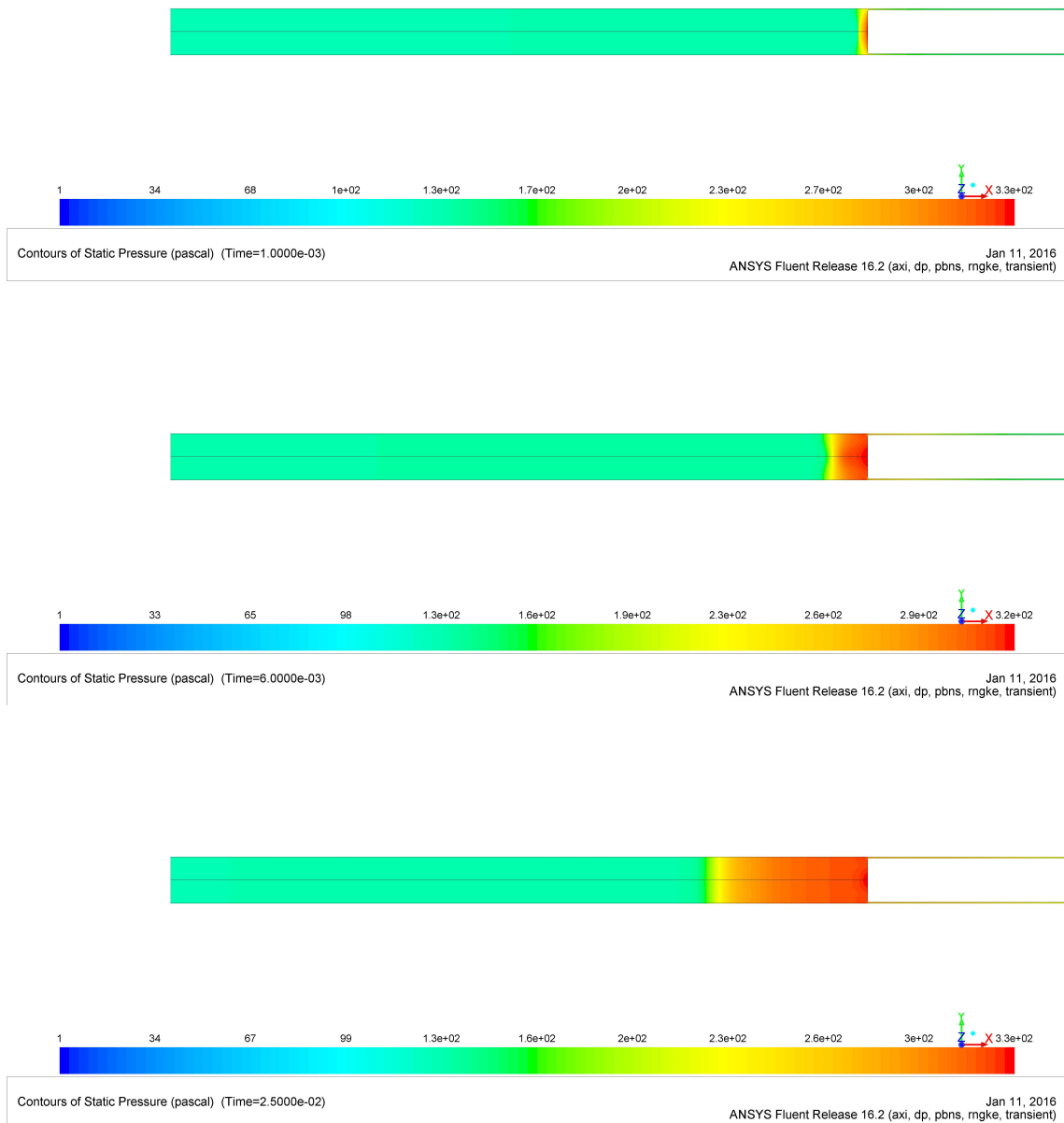


Figure 4.69: Pod inlet static pressure at braking.

This figure shows the pattern of the shockwave and initial Fanno flow as has been explained above. In addition, for comparison purposes, a plot of the pressure and temperature distribution along the domain's symmetry axis for a given timestep is included.

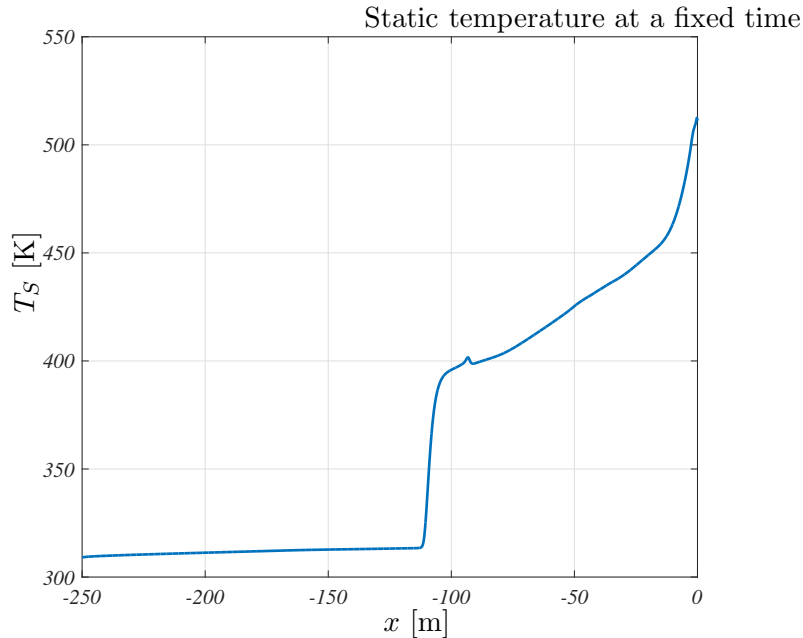


Figure 4.70: Static temperature at a braking timestep symmetry axis.

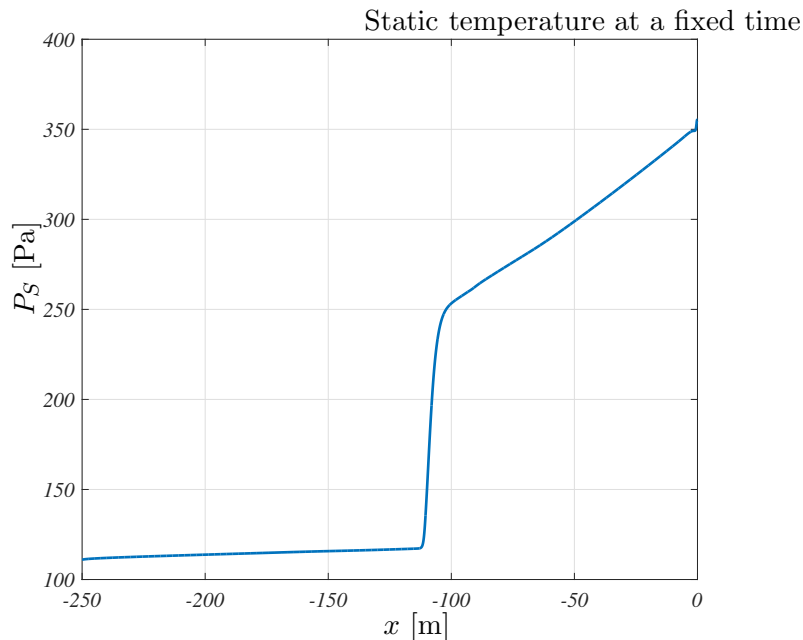


Figure 4.71: Static pressure at a braking timestep at symmetry axis.

In figures 4.70 and 4.71 a steep change is noticed in both, pressure and temperature, showing the location of the shock wave. Moreover, the pressure drop due to Fanno flow

can be seen from the shock wave to the pod's inlet.

After these analysis, it was decided to impose a constant deceleration value for the crewed braking phase. This constant value will be of $0.3m/s^2$ and will be controlled actively by changing the compressor discharge valve or the compressor operating point when needed. This has been decided for the sake of passenger comfort and safety.

4.6.1 Alternative braking proposal

In addition to the exposed braking system, an off-pod braking system method has been considered. This system will be composed of a series of pressure relief valves distributed along the track, together with a system of airlocks. The valves will enable the change of tube pressure in sections isolated via diaphragm airlock doors.

If a pod is unable to brake by its own means, a small tube section can be used to brake it by means of higher pressures in its front section. This airlock system allows for a lower recovery time and cost as it does not need to flood the entire vacuum tube with atmospheric pressure.

Additionally, system could potentially be used together with a set of emergency diversion tubes placed along the track.

4.7 Guidance, navigation and control

4.7.1 Sensors on board

In order to have a robust system, different sensors have to be distributed around the pod to avoid a possible loss of the signal. As the system is in a closed loop, a continuous reference needs to be received. The magnitudes to be measured are:

- Position
- Distance to the tube
- Attitude
- Environmental variables

4.7.2 Control scheme

This is a multiple input multiple output control problem as the distance to the tube and the attitude have to be controlled at the same time (MIMO problem). These magnitudes are related, so it is not the optimal solution to control them with independant controllers. For this reason, a control law has yet to be established, and the best way to fine tune it is experimentally. That is the reason why the following control scheme is proposed but without the control law which will ultimately control the pod.

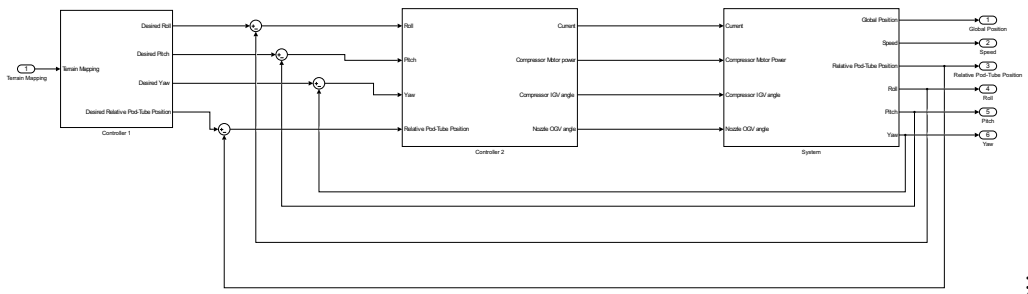


Figure 4.72: Control scheme proposed for the pod.

Digure 4.72 shows the proposed control scheme which, starting from a database of tube terrain cartography and taking into account the current pod position along the travel, pod attitude and relative pod position a desired pod attitude is generated. This desired attitude enters a block which both calculates the desired current at the EM in the levitation units and controls the roll-related variables (IGV, NZV positions and motor/generator speeds). The whole pod reacts to this changes and again, variables are measured closing the loop. The pod speed is not controlled in a closed loop, its control is open.

4.7.3 Guidance and navigation

Positioning

As the pod is placed inside a metallic tube, GPS is not expected to work properly, but this is also an advantage: the tube itself can be used to geolocate the pod. For that purpose, adhesive coloured tapes located in defined points can be used. These will have two functions:

- Incremental position: every time IR sensors detect a positioning tape, the distance is increased in a constant step.
- Absolute position: a camera captures the colour bands inside the tube. As the tapes have a characteristic colour, with a colour code the relationship between colour and position can be obtained, resulting in a measurement of the absolute position of the pod inside the tube.

In order to take this solution, some considerations need to be taken into account:

- 2 tapes in a 180deg configuration have been chosen to avoid problems in case of singular attitudes.
- A light shall be located at the beginning of the pod to allow the camera to analyze images and colours in a more reliant manner.
- Inertial navigation can be used to complement the other systems with the IMU's incorporated in the pod.
- All measures shall be coherent and they will be used in complementary and Kalman filters.

The diagram of the optical markings described can be seen in figure 4.73. Incremental yellow and red optical marks are distributed in steps of 200m and every 5 marks (1000 m) there is an absolute optical mark that the camera will analyze. The colour of this mark depends on the location. With 10 different colours and two positions, there are 1024 different combinations and every two colour combination of colours can be assigned to every kilometer.

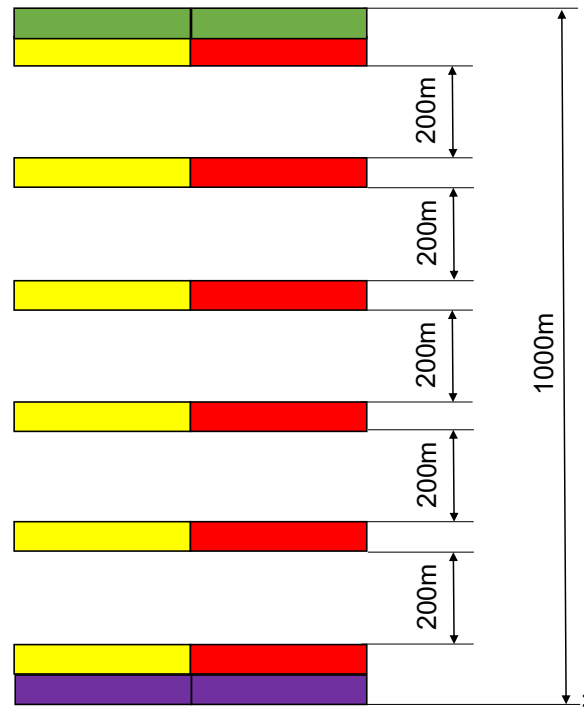


Figure 4.73: Positioning patterns in the tube.

As an exception, when approaching and leaving a station a double blue optical mark will warn the system and the incremental marks will be distributed in a 50 m spacing and in a double configuration to improve accuracy as shown in figure 4.74.

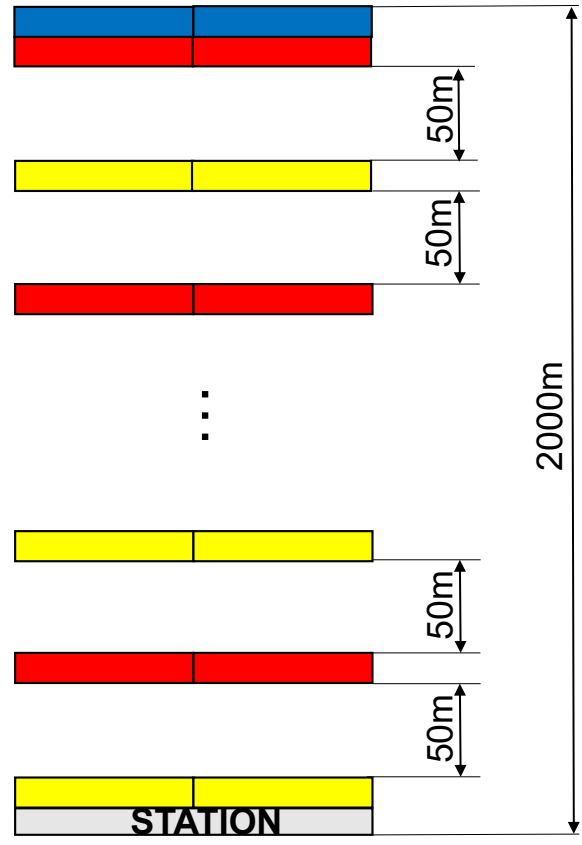


Figure 4.74: Positioning patterns in the tube. Terminal guidance.

The images used to estimate position can be also used to estimate the attitude, as the marks are distributed symmetrically and tangent to the direction of the tube.

Distance to the tube

This is the most critical magnitude to be measured, as the pod shall be in the setpoint all the time. For that reason there are different sensors chosen for that function:

- Laser: the reflexion with the tube is used to estimate the distance.
- IR: same principle as the Laser sensor.
- Hall effect: the magnetic flux is related with the distance between the magnets and the tube.
- Inductive proximity sensors: the inductance between the sensor and the tube is related with the distance.
- LDR circuit: as there is a light at the beginning of the pod, the light received by the LDR is dependent on the distance due to the shadows created.

- Inertial sensors: gyroscopes and accelerometers can be used to estimate displacements of the pod.

Pod attitude

This magnitude is related with the previous one but shall also be estimated. In order to do this, the sensors chosen are:

- Inertial sensors: gyroscopes and accelerometers can be used to estimate Euler angles (global attitude)
- Differences between distances: different locations of different points of the pod are related with attitudes relatives to the tube.
- Camera: the position of the optical marks can be used to estimate the relative attitude.

Sensor	Position	Attitude	Distance
Camera	x	x	x
IR	x		x
Laser			x
Hall Effect			x
LDR			x
Inductive			x
IMU	x	x	x

Table 4.3: Sensor and magnitude cross table.

4.7.4 Conclusions

As the system must be fault-tolerant, the presence of different sensors cannot be avoided. In order to handle faults, redundant sensors Kalman filters are the best solution. Nevertheless, same technology sensors must not be included in the same filter, e.g.: inductive and Hall effect.

Notwithstanding, as demonstrated with the magnetic model, the three variables can be controlled, however, speed and global position controls shall be performed in open loop.

In order to conclude, a proposed sensor location scheme can be found in figure 4.75. This scheme represents the location of the sensors which is related with the position of the magnetic levitation units, uniformly distributed along the pod length. As, there will be 8 levitation rings, 8 group of sensors should be located in order to obtain independence in each levitation actuator. On the top side of the pod, inductive sensors will not be placed in order to avoid interferences with the magnetic field created to hover, nevertheless, hall effect sensors are placed to measure this field and ensure proper control of the levitation units. As additional comments, inertial sensors have better performance if placed in the center of gravity of the system and a light has been placed close to the camera as there will be no light inside the tube for most of the pod travel.

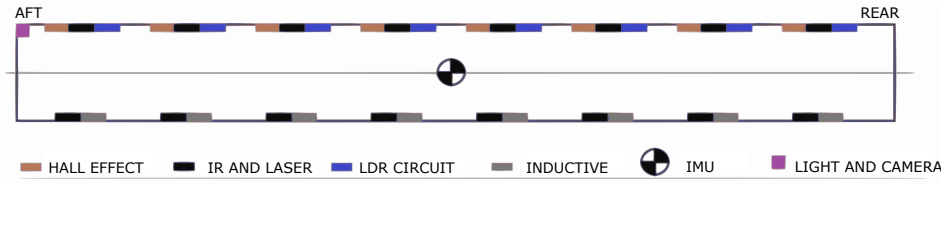


Figure 4.75: Pod sensors arrangement.

4.8 Safety measures

Safety is a critical point in the design of any transportation method. Traveling at sound speed could be thought as a very dangerous thing as it is thought of the airplane, even though it is the safest mean of transport. Hyperloop has to show that no matter how high the velocity is, you will be safe. The safety systems must be developed in the same way as the entire project, with the most advanced and innovative ideas available. Furthermore, safety regulations need to be merged with the design and performance of the pod. There are several basic safety systems to include in the cabin such as:

- Safety instructions: A video with instructions will be played at the beginning of the travel with safety instructions and procedures in case of emergency.
- Seat belt: The passengers must be secured to the pod with a seat belt. It could be an standard car seat belt, but in this case a 4-point seat belt will be the safest way of keeping the contact between the passenger and the seat. That is because when there is a turn, the pod will turn around its central axis and the passenger will not be completely horizontal. Therefore, the 4-point seat belt will hold the passenger no matter what the position of the pod is.
- Air-bag: The pod is going to be equipped with individual airbag that will protect the head of the passenger in the case of a high deceleration. The airbag will be set in the top part of the seatings of the passenger seated before. If there is a situation where the pod has to decrease its velocity suddenly, for instance a malfunction of the propulsion system, a problem with the levitation system that results in a collision with the tube...) the airbag will inflate rapidly and the head of the passenger will hit the airbag and not the next seat.
- Defibrillator: as there will be 30 people inside the pod, it is an statistical problem that some passenger may have some heart problems. This device is incorporated as it is demonstrated that its presence can save lives.
- Oxygen and CO₂ monitoring: sensors of O₂ and CO₂ should be incorporated in the pod, as the quality of the air is critical for the passengers and monitoring these magnitudes can diagnose an air leakage.
- Heartbeat and temperature monitoring: sensors integrated in the cabin for every seat can monitoring these vital constant and diagnose medical problems in order to have a quick response with the medical kit, defibrillator and oxygen mask.
- Oxygen mask: as the external pressure of the pod is 100 Pa, a system of ensuring the passenger's oxygen must be incorporated in the pod. The design of these oxygen mask are going to be similar to high altitude aircraft oxygen masks.
- First-aid kit: as the situation may be similar to emergency cases in an aircraft passenger cabin, COMMISSION REGULATION (EU) No 965/2012 of 5 October 2012 for Air Operations has been taken into account and the first-aid kit shall be in

compliance with: AMC1 CAT. IDE.A.220 First-aid kit CONTENT OF FIRST-AID KITS

- (a) First-aid kits should be equipped with appropriate and sufficient medications and instrumentation. However, these kits should be complemented by the operator according to the characteristics of the operation (scope of operation, flight duration, number and demographics of passengers, etc.).
- (b) The following should be included in the first-aid kit:
 - * (1) Equipment
 - (i) bandages (assorted sizes);
 - (ii) burns dressings (unspecified);
 - (iii) wound dressings (large and small);
 - (iv) adhesive dressings (assorted sizes);
 - (v) adhesive tape;
 - (vi) adhesive wound closures;
 - (vii) safety pins;
 - (viii) safety scissors;
 - (ix) antiseptic wound cleaner;
 - (x) disposable resuscitation aid;
 - (xi) disposable gloves;
 - (xii) tweezers: splinter; and
 - (xiii) thermometers (non-mercury).
 - * (2) Medications
 - (i) simple analgesic (may include liquid form);
 - (ii) antiemetic;
 - (iii) nasal decongestant;
 - (iv) gastrointestinal antacid, in the case of pods carrying more than 9 passengers;
 - (v) anti-diarrhoeal medication, in the case of pods carrying more than 9 passengers;
 - (vi) antihistamine.
 - * (3) Other
 - (i) a list of contents in at least two languages (English and one other). This should include information on the effects and side effects of medications carried;
 - (ii) first-aid handbook, current edition;
 - (iii) medical incident report form;
 - (iv) biohazard disposal bags.
 - * (4) An eye irrigator, whilst not required to be carried in the first-aid kit, should, where possible, be available for use on the ground.

AMC1 CAT. IDE.A.225 Emergency medical kit The following should be included in the emergency medical kit:

- (1) Equipment

- * (i) sphygmomanometer, non-mercury;
 - * (ii) stethoscope;
 - * (iii) syringes and needles;
 - * (iv) intravenous cannulae (if intravenous fluids are carried in the first-aid kit, a sufficient supply of intravenous cannulae should be stored there as well);
 - * (v) oropharyngeal airways (three sizes);
 - * (vi) tourniquet;
 - * (vii) disposable gloves;
 - * (viii) needle disposal box;
 - * (ix) one or more urinary catheter(s), appropriate for either sex, and anaesthetic gel;
 - * (x) basic delivery kit;
 - * (xi) bag-valve masks (masks two sizes: one for adults, one for children);
 - * (xii) intubation set;
 - * (xiii) aspirator;
 - * (xiv) blood glucose testing equipment; and
 - * (xv) scalpel.
- (2) Instructions: the instructions should contain a list of contents (medications in trade names and generic names) in at least two languages (English and one other). This should include information on the effects and side effects of medications carried. There should also be basic instructions for use of the medications in the kit and ACLS cards (summarising and depicting the current algorithm for advanced cardiac life support).
 - (3) Medications
 - * (i) coronary vasodilator e.g. glyceriltrinitrate-oral;
 - * (ii) antispasmodic
 - * (iii) epinephrine/adrenaline 1:1000 (if a cardiac monitor is carried);
 - * (iv) adrenocorticoid-injectable;
 - * (v) major analgesic;
 - * (vi) diuretic-injectable;
 - * (vii) antihistamine-oral and injectable;

5

Cost and production analysis

In the following chapter the costs of the project are estimated based on real market figures and a list of all resources needed is described.

5.1 Pod cost breakdown

The following calculations apply for the construction of a real size Pod following the specifications provided by the Space X's Hyperloop proposal, not the human-rated Pod. Metal costs are based in stock exchange guidelines. Most aeronautical-alike elements have been assigned prices based in the current aircraft scene.

First of all, an overview of the costs of the main subsystems of the pod will be depicted. These are: levitation, main structure, propulsion system and batteries. These parts are considered the core parts of the project, representing an amount of about 90% of the total cost of the pod. A special focus will be given to them, intending to obtain the best quality-price ratio. The other systems represent a small percentage and will therefore be not so critical.

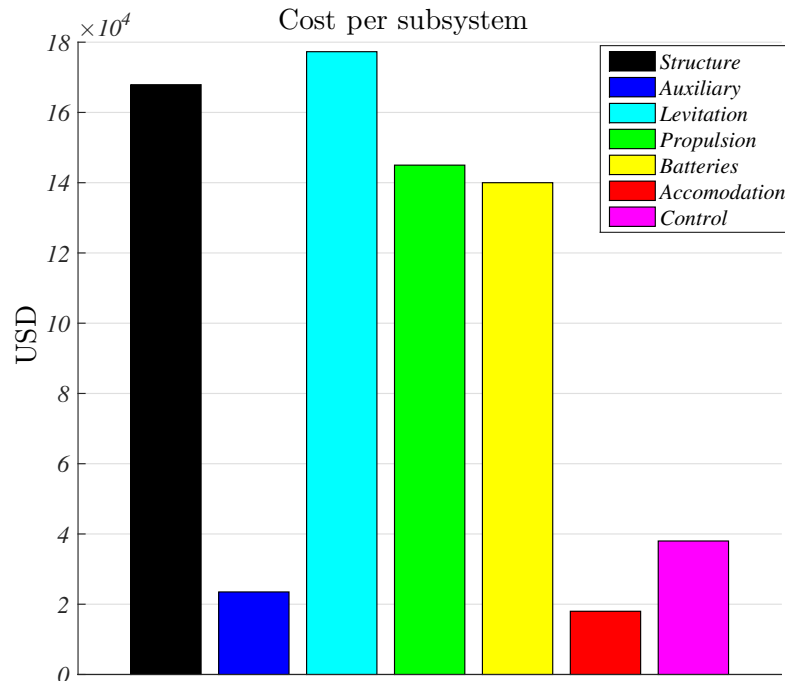


Figure 5.1: Pod costs by subsystem.

;

At this stage, the different subsystem components are detailed:

Levitation system

It considers copper coils and neodymium alloy magnets needed for each levitation unit. Also, eight levitation rings made of these units are needed, with five levitation modules in each one of them. As a result, forty levitation units made of both components, permanent magnet (Neodymium) and electromagnet (Copper), are required.

Main structure

For the main structure subsystem, carbon fiber for the main semi-monocoque bodyshell will be employed, as well as both aluminium and Kevlar for the structural reinforcements and other pod structures. Thickness has been obtained by computing simulation, explained in the chapter on the structural analysis of this document (see section 4.5).

Propulsion system

The main parts of the propulsion system are the turbine and the compressor.

Batteries and power system

The fourth core system to take into account are the batteries and power systems. The price contains the main battery cost plus a second auxiliary battery with a quarter of its energy. For that purpose, energy density levels with a price of 80 USD/KWh are considered, something that could be improved in the near future thanks to constant and recent research in batteries for automotive and other industries.

All these considerations, as well as the other subsystems are represented in the breakdown table below:

Section	Breakdown		Units	Unit	Price	Total price
Main Structure	Monocoque	3000	kg	55	USD/kg	165000
	Structural reinforcement	100	kg	11	USD/kg	1100
	Structural component	300	kg	6	USD/kg	1800
Auxiliary systems	Undercarriage	4	-	4000	USD/unit	16000
	Emergency Oxygen supply	30	-	250	USD/unit	7500
Levitation	Neodymium alloy	102.2	kg	40	USD/kg	
	Copper coils	46.1	kg	4	USD/kg	
	Levitation unit	40	-	4432.4	USD/unit	177296
Propulsion	Compressor	1	-	75000	USD/unit	75000
	Turbine	1	-	70000	USD/unit	70000
Batteries	Main Battery	1400	KWh	80	USD/kWh	112000
	Emergency Battery	350	KWh	80	USD/KWh	28000
Accomodation	Cabin accomodation	30	-	300	USD/unit	9000
	Access door system	10	-	400	USD/unit	4000
	Other	1	-	5000	USD/unit	5000
Control	Sensor Kit	2	-	30000	USD/unit	60000
	Control system computer	4	-	4000	USD/unit	16000
	Control system network	8	-	2500	USD/unit	20000
						767696

Table 5.1: Pod cost breakout.

The previous calculations contain only the bill of materials for the pod, the production process costs are not included. For a more accurate measure, an analysis of the construction, assembling and testing phases is needed to obtain the final price for each pod. In order to obtain this cost in the safe side, a productive/materials ratio conversion of 1,9 is considered to calculate this part. Last, the price of the complete fleet of pods should be estimated using a frequency of the line of 5 minutes between a pod and the next one, and the course characteristics.

As shown below, a fleet of 16 pods could completely cover the desired track requirements.

Pod Avg speed	270	m/s
Frequency of the line	5	min
Travel distance	614	km
Total round travel distance	1228	km
Distance between pods	81	km
Number of pods travelling	16	-
Extra pods	5	-
Total of pods to be built	21	-

Table 5.2: Pod final production costs.

As a conclusion, the definitive pod production cost table is included in table 5.3.

Concept	Cost	Unit
Material cost	0.77	Million USD/pod
Production-cost ratio	0.9	Production cost/Material cost
Production and material pod cost	1.46	Million USD/pod
Total number of pods for the track	21	-
Total materials cost	16.12	Million USD
Total pod price	30.63	Million USD

Table 5.3: Pod final production costs.

5.2 Track cost breakdown

In order to calculate the cost reduction that the system could achieve due to the removal of rails inside the tube, an estimation of the costs of the rail has been elaborated based on SpaceX's Hyperloop Test Track specifications and the information available in the first Hyperloop Alpha whitepaper.

The current pod design proposal consists of a system that avoids the following parts of the first tube design:

- Aluminum Rail
- Aluminum Plates
- Concrete support

Considering a tube length of 614 km, the section of all three elements following the Test Track specifications has been calculated to obtain the volume needed. Afterwards, the total mass of aluminum was determined and, according to current price of materials, obtaining the cost that a Test Track with the size of the real track. The total cost suggested a figure of \$188M. According to the Hyperloop Alpha whitepaper, the total cost of the tube is estimated in \$640M. Thus, the use of a rail-free system would represent a cost reduction of up to 30%.

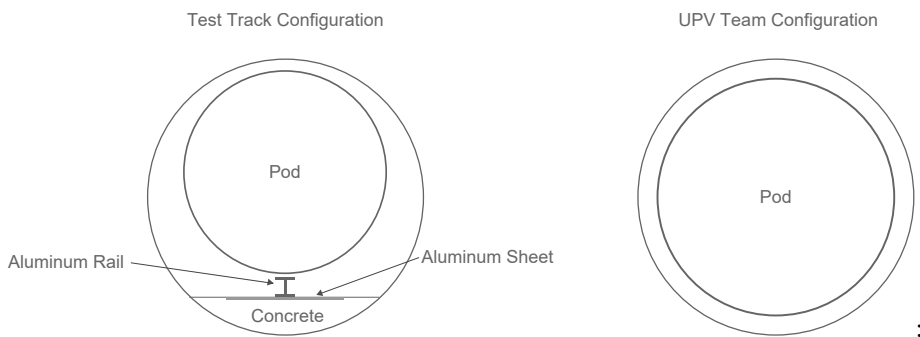


Figure 5.2: Tube layout comparison.

5.3 Production planning

The production process of each pod can be decomposed into various modules. This will allow for optimization and estimation of time needed to build each transport unit. The main modules of the project schedule are presented below:

Module 1: Cabin

The initial module. Process begins with a resin transfer (RTM) and injection system, wherein resin is introduced under pressure into a preheated mold containing the carbon base. Next to the addition of structural reinforcements and a high temperature cure of materials, the main cabin structure is obtained and ready to mechanize.

Module 2: Levitation

Each levitation unit requires a neodymium core surrounded by a copper coil. After the integration of both parts of the module, it is needed to compact them and calibrate measurements perfectly.

Module 3: Propulsion

This module presents two different parts: Turbine and Compressor, which are constructed independently and ready to integrate with the Module 1.

Module 4: Mechanical elements

Some mechanical parts of the pod are included. The access gate system actuators allow to get inside the pod also enabling strong hermetic seals. Furthermore, the wheel sets should be added to the pod as an auxiliary system for departures and arrivals.

Module 5: Accommodation

After complete Module 1, the passenger elements of the cabin are introduced. 30 seats are necessary for our pod. Subjection and habitability elements needed are placed too.

Module 6: Security

Security systems should meet quality requirements. Seat belt, air-bag, defibrillator, oxygen mask and other, must be tested after installation.

Module 7: Control and Communication

Due to the high level of control necessities, the pod presents triple redundancy in computation and communication centers, also, double redundancy in data acquisition system by duplicating the number of sensors. Moreover, additional replacement modules are included in each part.

A Gantt diagram of the mentioned process is displayed in figure 5.3.

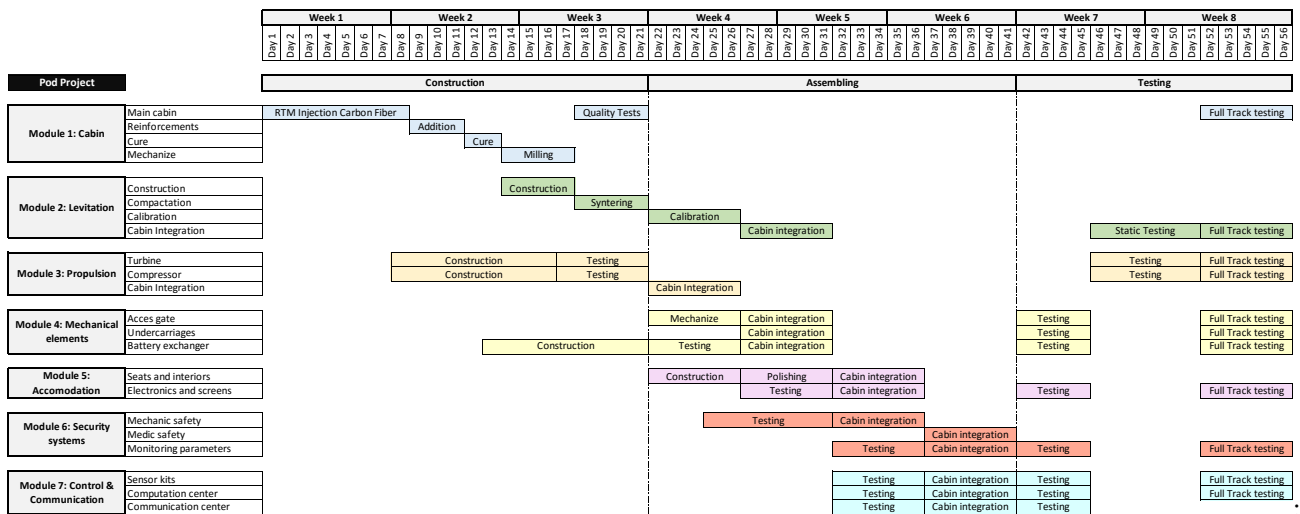


Figure 5.3: Gantt diagram for the project production.

6

Final proposed solution specifications

The pod solution proposed parameters is detailed as follows.

Geometric dimensions

Parameter	Value	Unit
Pod Length	19	m
Pod Diameter	2.1	m
Pod-Tube distance	0.05	m
Cabin length	15	m
Cabin height	1.4	m

Table 6.1: Pod final dimensions.

Aerodynamic coefficients and conditions

Cruise lift coefficient	0	-
Cruise drag coefficient	0.8587	-

Table 6.2: Pod final aerodynamic performance.

Magnetic characteristics and conditions

Number of levitation units per assembly	5	-
Number of levitation assemblies	8	-
Maximum field strength	2.76	T
Maximum current	$3 \cdot 10^5$	A·Turn

Table 6.3: Pod final magnetic parameters.

Power per subsystem

System	Power	
Propulsion (high speed)	356	kW
Propulsion (low speed)	425	kW
Levitation	163	kW
Auxiliary (imposed)	100	kW

Table 6.4: Pod final power distribution.

Mass per subsystem

System	Mass	
Propulsion	2575	kg
Battery	2290	kg
Structure	3750	kg
Levitation	5700	kg
Auxiliary (imposed)	500	kg
Payload	3600	kg
Control and sensors	1200	kg
Overall pod mass	19615	kg

Table 6.5: Pod final mass budget.

Pod performance

Travel maximum speed	276	m/s
Acceleration, phase 1	0.6	m/s^2
Acceleration, phase 2	0.3	m/s^2
Deceleration, phase 1	0.3	m/s^2
Deceleration, phase 2	0.6	m/s^2
Payload weight	3600	kg
Stored energy	665	kWh

Table 6.6: Pod final power distribution.

Pod velocity profile

The pod velocity profile is showed in figure 6.1.

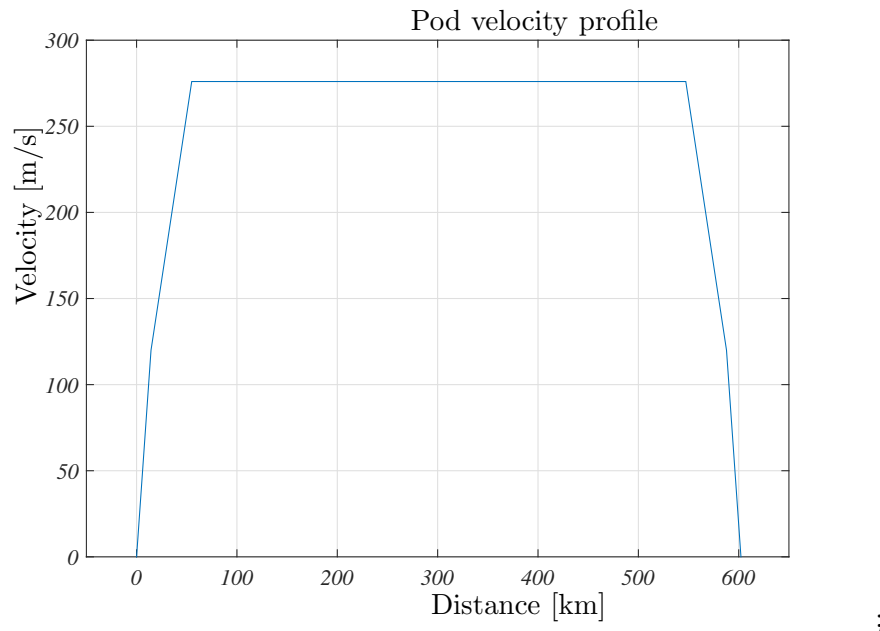


Figure 6.1: Pod velocity profile.

Pod thermal profile

The pod thermal profile is fairly constant regarding the velocity dependance as can be seen in figures 4.39 and 4.40. The only situation where it might exceed 50 degree above ambient temperature is during emergency braking. In this case, the front part of the pod experiences temperatures of 1200 K . Regarding the internal air tube, it should be conveniently isolated.

7

Conclusions

As it has been detailed throughout the chapters of this document, the current design proposed by the Hyperloop Makers UPV Team differs substantially from the previous work done by SpaceX in the Hyperloop Alpha proposal. This will be summarized at this stage in order to obtain a global perspective, highlighting key advantages and providing an order of magnitude in broad terms.

First of all, the design offers a rail-free alternative for the levitation system. Rails avoided, estimated savings of up to 30% of the total tube construction cost could be achieved. This is a promising achievement taking into account that the tube construction costs represent 90% of the total Hyperloop project. The proposed design would achieve about \$180M in cost reduction for construction as well as avoiding rail maintenance costs and spare parts due to aging and wear. Speed is also one of the most important advantages of the system. At a travel speed of up to 1000 kilometers per hour, the pod could commute from Los Angeles to San Francisco in about 45 minutes.

From the point of view of the ergonomics, it has been detected that the size of the tube, and thus, the size of the pod, would be too tight to carry passengers in a sufficiently comfortable way. Despite the existence of several aircraft models which are even smaller than the proposed design. Therefore, the team considers that, in case of longer journeys, passengers would greatly benefit from a wider pod diameter. The cabin layout of the current pod has been designed to fit 30 passengers. Additionally, as there is no rail, the tube has angular symmetry and the pod is able to roll to compensate the inertial forces which passengers could suffer otherwise.

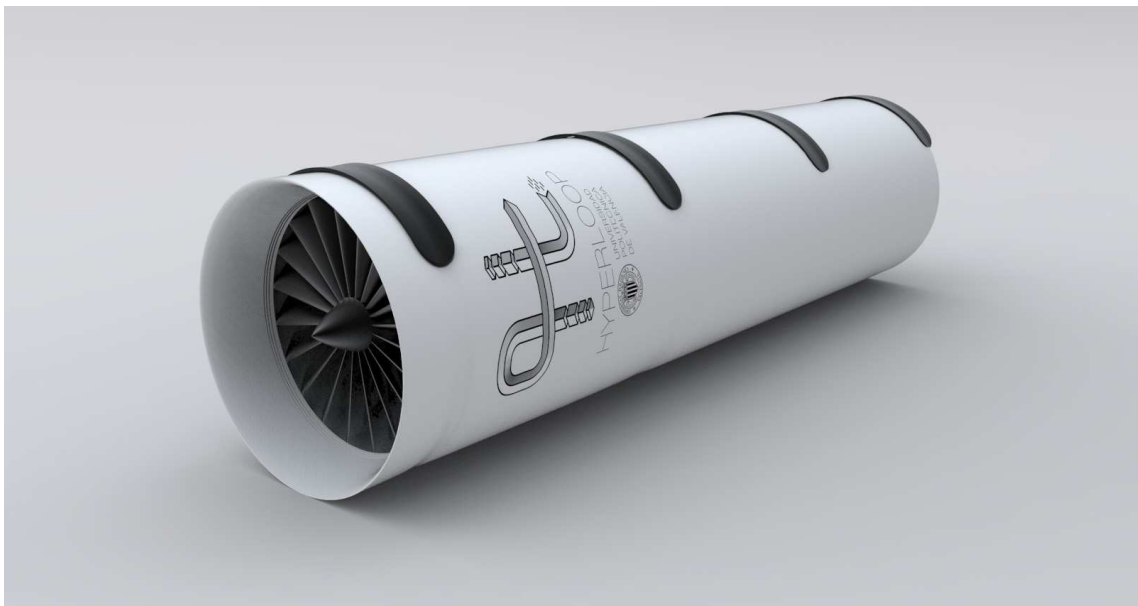


Figure 7.1: Proposed concept appearance.

Levitation

The levitation system has been validated with a real model of a magnetic levitator from the Institute of Automatic Systems (ISA) available at the University. Firstly, the levitation system consistent in electromagnet-magnet has been validated to be controlled in a stable behavior and after that the proposal design has been simulated with the ANSYS Maxwell software. In addition, dynamic behavior has been studied in order to obtain the influence of Lenz's Law. The result of the studies show that Lenz's Law reduces the effectiveness of the levitation system up to 75% at 260 m/s. This fact could be overcome by reducing the gap thickness between the tube and the pod at high speeds, increasing EM current or oversizing the levitation system. As a conclusion, the chosen layout for the levitation systems consists in 8 rings with 5 levitation units uniformly distributed along the pod length at the upper side.

Aerodynamics and propulsion

Regarding propulsion, the system consists in compressing the incoming air flowing along a inner tube up to a turbine that partially recovers energy and a nozzle that expands the air at the outlet of the pod producing thrust. In the CFD section, section 4.2, the behavior of the air has been studied at the inlet and outlet of the pod and in the gap between pod and tube. The obtained results validate that the thrust needed to achieve cruise speed and to keep it constant is more than enough. Additionally, this system allows braking with a constant deceleration by controlling the compressor discharge valve and/or compressor operating point. At low speeds, the propulsion system consists of a mechanical traction mechanism of retractable wheels which is more efficient than the aerodynamic propulsion at these speeds. Nevertheless, a complementary off-pod propulsion system could be proposed in order to reduce the energetic costs due to the initial acceleration and downsize the battery requirements. At a cruise speed of 276 m/s (roughly 1000 km/h) the pod consumption per passenger is as low as 35 kW.

Structure

The cabin structure has been designed in reinforced carbon fiber. Furthermore, structural ribs have been included in order to optimize the stress distribution across the cabin due to the internal pressurization loading and thus ensure optimum material use in the passenger cabin. ANSYS simulations show that the maximum strains and stresses obtained are between the acceptable ranges of the construction materials, thus validating the structural design. Moreover, vibration modes have been obtained in order to identify the natural frequencies of the structure and their strain pattern. These values should be rejected from the vibration operating environment.

Guidance, navigation and control

The guidance and navigation system has been designed with multiple and redundant sensors with different technologies in order to achieve a fault-tolerant system. An optical mark system has been chosen to locate the pod. The distances between marks has been increased up to 200 m and an absolute positioning system has been added through the analysis of camera images. The controlled variables are pod-to-tube gap distance and pod attitude. The velocity is defined in every location as the speed profile shows (see figure 6.1).

Safety

Every system has been designed with an alternative in case of failure as this kind of transportation system entails a lack of current regulation. This safety policy allows to prevent critical situations instead of acting after the emergency. Despite that, some corrective measures based on current aviation regulations have been considered as: oxygen masks, airbags or medical kits. Despite the efforts, a severe incident would almost signify passenger damage.

Costs

Due to the current pod design, the savings in the tube construction costs are fairly superior than the increase in pod price. For that reason, it is concluded that an on-pod system approach results in an economical advantage. Experiments and tests will be carried out in order to confirm the theoretical conclusions obtained from this design proposal.

8

Future work

The current work covers the design of a holistic proposal for a high-speed pod. Nevertheless, time is limited and more work and research should be carried out in order to cover each and every aspect of the solution. Below, some lines of research are detailed in order to provide a basis for future works.

Levitation

The study of alternative materials and magnet-electromagnet configurations for levitation optimization could allow mass and energetic cost reduction. For example, superconductor materials could be used to build electromagnets with superior power taking maximum advantage of space and energy needed to levitate the pod.

Aerodynamics and propulsion

A preheating of the inlet air in the compressor could be used to increase maximum pod speed keeping a constant Mach, which would avoid sonic problems. Additionally, a CFD study including the effect of swirl at the compressor inlet should be performed to validate the reduction of the velocity relative to the blades. Additional systems for supersonic and hypersonic travel speeds should be evaluated: rocket engines, scramjet, ramjet engines and other unconventional engines. Other considerations could include the study of aerodynamic elements for controlling the pod's attitude and position. The study of an aerospike type nozzle could improve the vortex situation appearing at the gap end.

Finally, regarding the aerodynamics and propulsion, certain fluid mechanic related problems exist while travelling inside the transonic regime. These do not allow the system to work in a stable and efficient manner but, after surpassing this regime, there are not restrictions to how fast the pod could travel from the aerodynamic point of view. Supersonic, nearly hypersonic, travel is possible with high efficiencies.

Control system

In order to improve the control system an optimal and robust control algorithm (H_{\inf} and LQR) should be designed. Also, signal conditioning with Kálmann filters and defining a functional communication protocol should be programmed for remote control and monitoring of the critical parameters for the pod from the base of operations. If robust control is obtained, the system can be designed with a narrower gap between pod and tube, this fact improves the aerodynamic drag of the system.

Safety

Lines of research within the safety system include the development safety diversion mechanisms to allow braking in a safety zone. This system would include flexible segments of tube in parallel. Those would, by means of hydraulic actuators, change the normal path of the tube to an auxiliary braking one that would allow braking. The system is explained in figure 8.1.

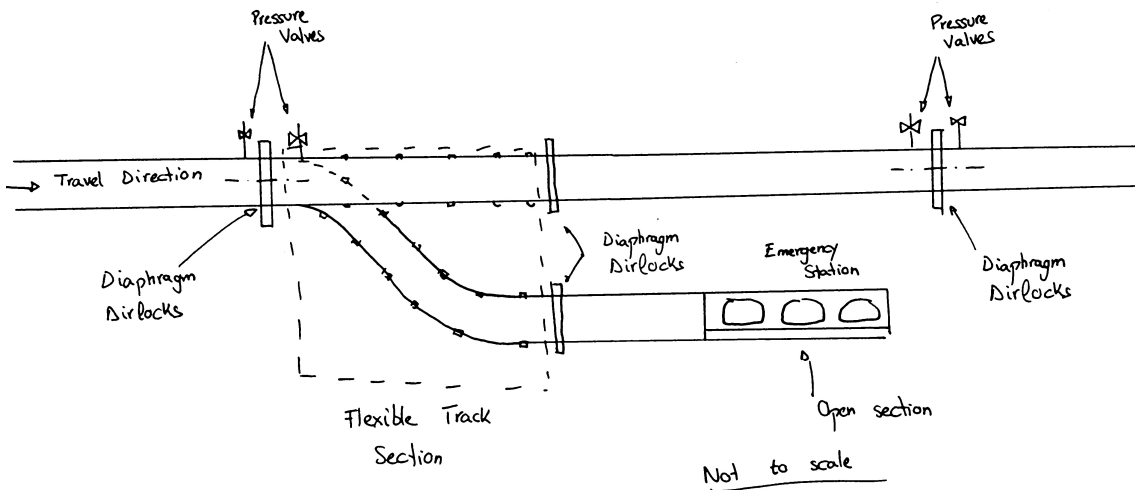


Figure 8.1: Diversion system proposal.

Besides developing additional safety systems the proposal will need to adjust to the upcoming regulation framework.

Systems integration and further studies

To validate the theoretical results displayed in this report, full range experiments and prototyping are required. Experimental results will enable further modelling and guide future analysis.

Scalability and cargo analysis

In order to ensure the feasibility of the system for commercial cargo, or to increase the passenger capacity of the pods, analysis of scalability should be carried out to obtain the optimal operation parameters.

Bibliography

- [1] SpaceX. *Hyperloop Alpha Design Proposal*, 2015.
- [2] F.M. White. *Fluid Mechanics*. McGraw-Hill international editions. McGraw-Hill, 2003.
- [3] Peter J. Fleming Carlos M. Fonsecay. Genetic algorithms for multiobjective optimization: Formulation, discussion and generalization. 1993.
- [4] Stanley M. Shinners. *Modern control system theory and design*. 1993.
- [5] DoD USA. *MIL-HDBK-17-2F Composite Materials Handbook*, 2002.